Department of Geomatics Engineering

# Temporal Characteristics of GPS Error Sources and Their Impact on Relative Positioning

**(URL: http://www.geomatics.ucalgary.ca/links/GradTheses.html)**

**by**

**Michael C. Olynik**

**July 2002**

UNIVERSITY OF
CALGARY

THE UNIVERSITY OF CALGARY


TEMPORAL CHARACTERISTICS OF GPS ERROR SOURCES

AND THEIR IMPACT ON RELATIVE POSITIONING


by


MICHAEL C. OLYNIK


A THESIS

SUBMITTED TO THE FACULTY OF GRADUATE STUDIES

IN PARTIAL FULFILLMENT OF THE REQUIREMENTS FOR THE

DEGREE OF MASTER OF SCIENCE


DEPARTMENT OF GEOMATICS ENGINEERING


CALGARY, ALBERTA

JULY, 2002

# ABSTRACT

Some GPS applications require precise single point positions that are stable over time. However, changes in GPS error sources can lead to a degradation in the relative (over time) stability of the estimated positions. For this reason, it is not the absolute errors, but rather their temporal variations, that are of importance. In this research, the temporal characteristics of the orbital, satellite clock, and ionospheric errors are analyzed independently. Satellite clock and orbit errors are analyzed by comparing broadcast and precise satellite clock corrections and orbits. Dual frequency carrier phase data is used to assess the change in the ionospheric error. The remaining errors, which include the tropospheric error, multipath, and noise are investigated together. To compute the remaining errors, the receiver clock error must be removed, which is possible if the position is known. The analysis comprises primarily of assessing error behaviors and magnitudes through time and frequency analyses. In this way, the differences in variability of the errors are easily determined.

The effect of each error in the position domain is investigated in addition to the combined effect. Data from various field conditions has been used in the analysis. Static results show that on a typical day when single frequency data is processed with broadcast orbit and clock data, the root mean square (RMS) of the changes in the position errors over a 50 second interval is about 5.6 cm in northing, 3.9 in easting and 10.2 cm in height. When using precise orbits and clocks, in addition to dual frequency data, these values improve by 46-54% to 2.6 cm in northing, 2.1 cm in easting, and 4.7 cm in height. Under severe ionospheric activity, the RMS of the changes in the errors decrease from 8.1 to 3.3 cm in northing, 5.7 to 2.6 cm in easting, and 17.0 to 4.9 cm in height, which are improvements of 54-71%. In a kinematic environment the improvement is 43-63% in all three components.

# ACKNOWLEGMENTS

**TABLE OF CONTENTS**

# LIST OF TABLES

# LIST OF FIGURES

**Page**

# LIST OF SYMBOLS

| | |
|---|---|
| p | measured pseudorange (m) |
| $\rho$ | geometric range (m) |
| $d\rho$ | orbital error (m) |
| c | speed of light (m/s) |
| dt | satellite clock error (s) |
| dT | receiver clock error (s) |
| $d_{ion}$ | ionospheric error (m) |
| $d_{trop}$ | tropospheric error (m) |
| $\varepsilon_p$ | receiver code noise plus multipath (m) |
| $\Phi$ | observed integrated carrier phase (m) |
| $\lambda$ | wavelength (m) |
| N | integer ambiguity (cycles) |
| $\varepsilon_\Phi$ | receiver carrier phase noise plus multipath (m) |
| $\dot{\Phi}$ | Doppler measurement (Hz) |
| $\dot{\rho}$ | derivative of geometric range with respect to time (Hz) |
| $\dot{dp}$ | derivative of orbital error with respect to time (Hz) |
| $\dot{dt}$ | derivative of satellite clock error with respect to time (Hz) |
| $\dot{dT}$ | derivative of receiver clock error with respect to time (Hz) |
| $\dot{d}_{ion}$ | derivative of ionospheric error with respect to time (Hz) |
| $\dot{d}_{trop}$ | derivative of tropospheric error with respect to time (Hz) |
| $\dot{\varepsilon}_\Phi$ | derivative of receiver phase noise plus multipath with respect to time (Hz) |
| $af_2$ | second order coefficient ($s^{-1}$) |
| t | time of measurement (s) |
| $t_{oe}$ | time of ephemeris (s) |

| | |
|---|---|
| $af_1$ | first order coefficient |
| $af_0$ | zero order coefficient (s) |
| $d_{rel}$ | relativity correction (s) |
| $t_{gd}$ | group delay (s) |
| $f_1$ | L1 frequency (Hz) |
| $f_2$ | L2 frequency (Hz) |
| $\lambda_1$ | L1 wavelength (m) |
| $\lambda_2$ | L2 wavelength (m) |
| $\Phi_1$ | L1 carrier phase measurement (cycles) |
| $\Phi_2$ | L2 carrier phase measurement (cycles) |
| $N_1$ | L1 integer ambiguity |
| $N_2$ | L2 integer ambiguity |
| $\sigma_p$ | standard deviation of point position (m) |
| DOP | dilution of precision |
| $\sigma_r$ | standard deviation of range measurement (m) |
| $\hat{P}_i$ | smoothed range at $T_i$ (m) |
| $\hat{P}_{i-1}$ | smoothed range at $T_{i-1}$ (m) |
| $P_i$ | pseudorange at $T_i$ (m) |
| $\Phi_i$ | phase measurement at $T_i$ (cycles) |
| $\Phi_{i-1}$ | phase measurement at $T_{i-1}$ (cycles) |
| $W_1$ | weight of the pseudorange measurement |
| $W_2$ | weight of the carrier phase predicted range |
| $\Phi_{pred}$ | predicted phase measurement (cycles) |
| $\Phi_{i-1}$ | phase measurement at previous epoch (cycles) |
| $\dot{\Phi}_i$ | Doppler measurement at current epoch (cycles/s) |
| $\dot{\Phi}_{i-1}$ | Doppler measurement at previous epoch (cycles/s) |

| | |
|---|---|
| $\Delta t$ | time difference between current and previous epochs (s) |
| g | data set (m) |
| $\tau$ | time of observation (s) |
| $\varphi$ | argument of latitude (radians) |
| i | inclination of orbit (radians) |
| $\Omega$ | longitude of the ascending node (radians) |
| $\Delta x$ | across-track satellite antenna phase center offsets (m) |
| $\Delta y$ | along-track satellite antenna phase center offsets (m) |
| $\Delta z$ | radial satellite antenna phase center offsets (m) |
| $x_s$ | x satellite coordinate in ECEF frame (m) |
| $y_s$ | y satellite coordinate in y direction in ECEF frame (m) |
| $z_s$ | z satellite coordinate in z direction in ECEF frame (m) |
| $x_a$ | x receiver coordinate in ECEF frame (m) |
| $y_a$ | y receiver coordinate in ECEF frame (m) |
| $z_a$ | z receiver coordinate in ECEF frame (m) |
| $\Delta\Phi$ | remaining errors |

# LIST OF ABBREVIATIONS

| | |
|---|---|
| C/A | Course acquisition |
| DGPS | Differential GPS |
| DOP | Dilution of Precision |
| ECEF | Earth-Centred-Earth-Fixed Frame |
| EDOP | Easting Dilution of Precision |
| EU | European Union |
| GDOP | Geometric Dilution of Precision |
| GPS | Global Positioning System |
| HDOP | Height Dilution of Precision |
| IGS | International GPS Service |
| MEDLL | Multipath Estimating Delay Lock Loops |
| MET | Multipath Elimination Technology |
| NAPA | National Academy of Public Administration |
| NAWC | Naval Air Warfare Center |
| NDOP | Northing Dilution of Precision |
| NOAA | National Oceanic and Atmospheric Administration |
| NRC | National Research Council |
| NRCan | Natural Resources Canada |
| PDOP | Three-dimensional Dilution of Precision |
| PRN | Psuedorandom noise |
| PSD | Power Spectral Density |
| RMS | Root Mean Square |
| SA | Selective Availability |
| SCSF | Satellite-Centred-Satellite-Fixed Frame |
| SV | Satellite Number |
| TDOP | Time Dilution of Precision |
| TEC | Total Electron Content |
| URA | User Range Accuracy |

**CHAPTER 1**

**INTRODUCTION**

**1.1 Background**

In the past few years, a need has developed for stable positioning over time. Stable positioning can be thought of as precise relative positions as a function of time. This means that over many epochs the position errors change as little as possible. It is not the absolute positions that are of interest; rather it is the change in the errors of the positions. One application, led by the Naval Air Warfare Center (NAWC), uses the P3-Orion aircraft to perform differential magnetometer measurements in support of a submarine detection program. The magnetometer is located in a 5 m tail boom that is subjected to buffeting effects (up and down movement of the aircraft) of up to a few metres. In order to maximize the resolution of these magnetometer measurements, precise relative (over time) positions of the aircraft are required, so the buffeting effect can be removed from the magnetometer signal. For this application, the relative positions must be determined at the level of a few centimetres over a time interval of 2-50 seconds. An additional requirement is that the time series of the computed positions be free of discontinuities and jumps in the position. If there are any discontinuities in the time series, then the buffeting effect is incorrectly removed from the magnetometer data. A future requirement of this application is the ability to do real-time positioning.

One system which can supply the necessary accuracy is the Global Positioning System (GPS), which is a satellite-based radio-navigation system. The system uses line-of-sight measurements and is available in all weather conditions. GPS was developed by the United States Department of Defense and became fully operational in 1994 (Parkinson et al., 1995). GPS is a military system, and when it first became operational optimal accuracies were not available to the civil user community. Before May 2000, GPS

positions were intentionally degraded by a method known as selective availability (SA) (Seeber, 1993). SA was implemented by dithering the satellite clocks, and caused a range error with a standard deviation of 24 m (Zumberge and Bertiger, 1996). Since SA was turned down to zero in May 2000 (White House, 2000), the single-point accuracy using GPS has dramatically improved (Auld, 2000). This allows GPS to be used in more applications where it would have been previously inadequate. A resulting improvement after the removal of SA is in the temporal stability of GPS position estimates. The maximum change in the range error caused by SA was 2 metres over a 1 second interval (NAPA/NRC, 1995). The relative positions in the NAWC application must be at the level of a few centimetres for intervals of up to 50 seconds, so under SA conditions the requirement could not have been met.

Even though SA is not a factor, other errors still have a significant effect on the position solution. Errors due to the broadcast orbits give degraded satellite coordinates. In the past, SA affected the satellite clocks, and although the clocks are now more accurate by more than one order of magnitude, the clock errors still affect the position solution (Neilan et al., 2000). Atmospheric effects due to the troposphere and ionosphere also have a detrimental effect on the solution. Finally, errors due to multipath and receiver noise cause errors in the position (Kaplan, 1996). Each of the errors changes over time, which together leads to an overall change in the GPS position errors. The effects are different for each error, and have different effects on the position error behavior.

Several correlated GPS errors, such as the orbital and atmospheric errors, can be reduced if more than one receiver is used. A technique known as differential GPS positioning (DGPS) typically uses two receivers. One receiver is at a known location, and is referred to as the reference receiver. Since the coordinates are known, the distances from the antenna to the satellites can be computed. By comparing the actual GPS measurements to the computed distances, a correction can be determined. Another receiver at an unknown location, known as the rover receiver, can apply these corrections to its GPS observations. By using differential methods, the position accuracy of the remote receiver

can be improved. However, in the case of the airborne magnetometry application described earlier, the flights take place hundreds of miles from the shore, so single point positioning must be used. An alternate method is wide area differential GPS (WADGPS) (Peck et al., 1997), but this cannot be used since there is no ability to use a communications link. Therefore, the research is focused around maximizing the performance of single point positioning using broadcast orbit and clock data.

## 1.2 Objectives

There are two major objectives in this thesis. The first objective is to assess the temporal characteristics of several different GPS error sources. These errors include the orbits, satellite clocks, and the ionosphere. The other GPS error sources cannot be investigated independently, so the characteristics of the aggregate remaining errors are examined. The remaining errors include the tropospheric delay, multipath, and noise. The different error sources can be investigated using a few different methods, such as with an autocorrelation analysis or in the frequency domain. Another method of examining the change in the error as a function of time is by quantifying the changes over different time intervals. Previously, work has been done in this area relating to the ionospheric errors by Skone (1998) and Doherty (1997). However, the objective of this thesis is a more thorough investigation of the changes of the errors and their characteristics. The analysis will be primarily of time intervals of 2-50 seconds, although intervals of up to 30 minutes will be examined in order to further investigate the error behavior.

The second objective is to determine the effect of different errors on the position estimates. By using a variety of data sources, the effects of many GPS errors can be significantly reduced. In this case, it is the relative changes in the position errors, rather than the absolute position errors themselves, which are of interest. A goal of this analysis is to investigate methods to obtain the highest accuracy relative 3-D position components over time, of which the requirement is for a relative accuracy of a few centimetres over time intervals of 2 to 50 seconds. In the past work, in the area of positioning for

magnetometry has focused on the absolute errors, rather than the change over time (Lachapelle et al., 1994; 1996b). Due to the improved resolution of the magnetometer sensor, which in turn requires more accurate buffeting measurements, the change in the position errors is now more important. The aircraft operates far from shore so differential techniques are generally not feasible.

Three separate data sets are used to realize these objectives. The first is a static data set collected on the roof of the University of Calgary in November 2001. This data was collected continuously for nine days under various atmospheric conditions. The second data set was collected on a boat in the St. Lawrence Seaway in February 2002. Finally, an airborne data set was collected on an airplane near San Jose in June 2000. The three data sets are used to evaluate the algorithms in both static and kinematic environments.

**1.3 Outline**

The next two chapters will present relevant background material to this thesis. GPS theory and different errors that affect GPS observations will be discussed in Chapter 2. Chapter 3 will describe the basic theory of carrier smoothing, and smoothed relative single-point positions. The algorithm developed will be described, as well as solutions to problems that occur in precise positioning over time. Chapter 3 also includes the methodology used in the analysis of the different GPS error sources.

Chapter 4 describes the data used in this investigation. There are three data sets, and the details on how, where, and when they were collected is given in this chapter. For the two kinematic data sets the truth position of the antenna is unknown, so details are given on how a reference position is determined.

Chapter 5 will discuss the orbital, satellite clock, ionospheric, and remaining errors. The temporal behavior of the errors, in addition to an analysis of the frequency domain will be given. Orbital errors will be discussed with an emphasis on the differences in each

direction. The satellite clock errors will be investigated with respect to the different satellite blocks, due to the different clocks in each. The ionospheric error, and how its temporal behavior can change under different ionospheric conditions will be investigated. Remaining errors after the orbital, satellite clock, and ionospheric errors have been removed can be calculated. An analysis of the remaining errors before and after a tropospheric correction has been applied will be given in Chapter 5.

Chapter 6 will discuss the changes in the positions over different time intervals. The positions will be computed under a variety of processing methods. These include using precise orbits, precise clocks, dual frequency data, as well as applying a tropospheric correction. A comparison of the results when different algorithms are applied will be given. The results will be presented under different operational conditions.

Chapter 7 will give some conclusions of this research, and recommend future work in this area.

**CHAPTER 2**

**INTRODUCTION TO GPS AND GPS ERRORS**

## 2.1 GPS Observables and Measurement Equation

The three main GPS measurements are the code, carrier phase, and Doppler measurements. The code pseudorange measurement is the amount of time it takes for the GPS signal to travel from the satellite to the antenna. It is calculated by correlating the received PRN code (C/A) with a replica code generated by the receiver. This time is multiplied by the speed of light to determine the distance traveled by the signal. The distance is not a true range measurement, due to clock errors in both the receiver and satellite. For this reason the code measurement is referred to as the pseudorange (Wells et al., 1987).

Ideally, the carrier phase measurement would be the number of full and fractional cycles between the satellite and receiver antennas. However, a GPS receiver cannot distinguish one cycle from another, so it measures the fractional phase and keeps track of the changes in the phase. For this reason the carrier phase measurement is ambiguous, and cannot be used alone for GPS positioning (Langley, 1998).

Currently, GPS satellites transmit on two frequencies, referred to as L1 and L2. The L1 frequency is 1575.42 MHz, while the L2 frequency is 1227.60 MHz. However, the P code on the L2 frequency is encrypted, so measurements are not available to civil users unless techniques are used which decrease the signal strength by 14 to 31 dB (Woo, 1999). For this reason, L2 measurements cannot be made with the same quality as they can on the L1 frequency. As part of the modernization of GPS, the L2 signal will be available to civil users, and a new L5 frequency of 1176.45 MHz will be part of the

system in the future (Challstrom, 1999).   This will lead to more accurate dual-frequency measurements, so the ionospheric error can be determined more accurately.

There are a number of errors in the GPS measurement equations.  The code pseudorange measurement equation in Wells et al. (1987) is:

$$p = \rho + d\rho + c(dt - dT) + d_{ion} + d_{trop} + \varepsilon_p \qquad (2.1)$$

where:

p        measured pseudorange (m),

$\rho$        geometric range (m),

$d\rho$        orbital error (m),

c        speed of light (m/s),

dt        satellite clock error (s),

dT        receiver clock error (s),

$d_{ion}$        ionospheric error (m),

$d_{trop}$        tropospheric error (m), and

$\varepsilon_p$        receiver code noise plus multipath (m).

The carrier phase measurement equation is (Wells et al., 1987):

$$\Phi = \rho + d\rho + c(dt - dT) + \lambda N - d_{ion} + d_{trop} + \varepsilon_\Phi \qquad (2.2)$$

where:

$\Phi$        observed integrated carrier phase (m),

$\lambda$        wavelength in (m),

N        integer ambiguity (cycles), and

$\varepsilon_\Phi$        receiver carrier phase noise plus multipath (m).

This equation is similar to the pseudorange equation, although there are some differences. The most notable difference is the integer ambiguity in the phase measurement equation. The integer ambiguity is the difference in the number of wavelengths between the start of the receiver generated carrier phase and the signal from the satellite. A second difference that while the magnitude of the ionospheric error is the same on both the code and phase measurements, it has an opposite sign. The ionosphere delays the code measurement, so the measured range is longer than the true value. In the case of the carrier phase, the signal is advanced by the ionosphere as it propagates through the atmosphere, so the measured range is shorter than the correct value.

The Doppler measurement is a measure of the difference in velocity between the satellite and antenna, and is typically measured in L1 cycles per second. The Doppler measurement does not have an integer ambiguity, and is in the range of $\pm$ 5 KHz. In this thesis the Doppler is only used to detect cycle slips on the carrier phase measurement. Another possible use of the Doppler measurement is in calculating the velocity. The equation of the Doppler is:

$$\dot{\Phi} = \dot{\rho} + \dot{d}p + c\left(\dot{d}t - \dot{d}T\right) - \dot{d}_{ion} + \dot{d}_{trop} + \dot{\varepsilon}_{\Phi} \qquad (2.3)$$

where the dots represent the derivatives with respect to time.

**2.2 Orbital Error**

GPS orbits can be computed in one of two different ways. One way is with the broadcast ephemeris, which are Keplerian and perturbation parameters transmitted from the satellite in the navigation message, typically at two-hour intervals. The navigation message is generated using measurements from five globally distributed monitor stations. By using the equations in Spilker (1996a), the coordinates of the satellite can be determined in the xyz frame from the broadcast ephemeris. The navigation message also contains an estimate of the accuracy of the broadcast clock and orbit, which is referred to as the User

Range Accuracy (URA). The URA allows the user to estimate the effect of the combined orbital and clock error on a single point solution. It was shown in Jefferson et al. (2000) that the errors in the broadcast orbits have been consistently decreasing over the last decade, from a median of about 7 m in 1992 to 4 m in 2000.

An alternate method of computing the satellite coordinates is the use of precise orbits. These are given by a number of agencies in three forms. One form is the ultra-rapid orbits, which are the least accurate type of precise orbits. The ultra-rapid orbits contain data for 48 hours. The first 24 hours of data are post-mission orbits computed with results from over 50 International GPS Service (IGS) stations. The next 24 hours of data are predicted, and are available for real-time positioning. The second type is rapid orbits, which are post-mission orbits available one or two days after the data is collected. These orbits are more accurate than the rapid orbits, but are not the best post-mission orbit. The third type is the final orbits, which are the most accurate at a level of better than 5 cm (IGS, 2001). These final orbits are available two weeks after the data has been collected. Each type of precise orbits has a data point every 15 minutes. The precise orbits used in this thesis are final orbits determined by Natural Resources Canada (NRCan). Table 2.1 shows the accuracy of the IGS orbits products as of March 2001 (IGS, 2001).

Table 2.1: Accuracy of IGS Orbits

| Product | Accuracy (cm) |
|---------|---------------|
| Ultra-Rapid | 25.0 |
| Rapid | 5.0 |
| Final | <5.0 |

## 2.3 Satellite Clock Error

Due to instabilities in the GPS satellite oscillators that are used in the GPS satellites, the user must adjust for the clock error. As with the orbits, the satellite clock error can be

determined by using parameters from the navigation message. The equation for determining the satellite clock error from the broadcast ephemeris is:

$$dt = af_2 (t - t_{oe})^2 + af_1 (t - t_{oe}) + af_0 + d_{rel} - t_{gd} \qquad (2.4)$$

where:

dt      satellite clock error (s),

$af_2$      second order coefficient (s$^{-1}$)

t      time of measurement (s),

$t_{oe}$      time of ephemeris (s),

$af_1$      first order coefficient (unitless),

$af_0$      zero order coefficient (s),

$d_{rel}$      relativity correction (s), and

$t_{gd}$      group delay (s).

It should be noted that equation (2.4) contains a correction for relativity. Due to the differences in velocity and gravitational potential of the satellite and antenna there is an apparent frequency shift in the satellite oscillator. This leads to an error of up to 70 ns for the satellite clock. By applying the relativity correction this error is removed (Seeber, 1993). Another term in equation (2.4) is the group delay, which is caused by the atmosphere delaying the signal. The group delay must be removed from the satellite clock error.

Since the broadcast navigation message is a prediction, the clocks computed from equation (2.4) are inaccurate. To obtain a better estimate of the satellite clock error precise clocks are used. As with the orbits, there are three types of precise clocks, and the precise clocks are available from the same agencies as the precise orbits. The ultra-rapid clocks are predicted, while the rapid and final are computed with IGS data. The precise clocks have a data interval of either 30 seconds or 15 minutes. In this thesis, final

clocks with a data interval of 30 seconds are used. As in shown in Table 2.2, the final precise clocks are accurate to 0.1 ns, which is equivalent to 3 cm in range (IGS, 2001).

Table 2.2: Accuracy of IGS Clock Corrections

| Product | Accuracy (ns) | Accuracy (cm) |
|---|---|---|
| Ultra-Rapid | 5.0 | 150 |
| Rapid | 0.2 | 6 |
| Final | 0.1 | 3 |

## 2.4 Ionospheric Error

The ionosphere is a region of ionized gases in the atmosphere which affects GPS signals. A major effect of the ionosphere examined in this paper is the carrier phase advance. This effect is different on the L1 and L2 frequencies, so the magnitude of the error can be computed. A typical ionospheric error is 5 metres (Skone, 1998), although it varies due to factors such as the elevation angle and the time of day. By comparing the L1/L2 range measurement with the single frequency observation, the first-order ionospheric error can be determined. The equation for the phase measurement advance in Wells et al. (1987) is:

$$d_{ion} = \frac{f_2^2}{f_1^2 - f_2^2} \left( \Phi_1 \lambda_1 - \Phi_2 \lambda_2 - \left( N_1 \lambda_1 - N_2 \lambda_2 \right) \right) \tag{2.5}$$

where:

$f$      frequency of L1 or L2 (Hz),

$\lambda$      wavelength of L1 or L2 (m),

$\Phi$      carrier phase measurement on L1 or L2 (cycles), and

$N$      integer ambiguity on L1 or L2 (cycles).

The error computed in equation (2.5) is dependent on the carrier phase ambiguity. The ambiguity must be determined computationally to obtain the absolute ionospheric error. However, to determine the change in the error over time, the ambiguity can be neglected. The methodology to do this is given in Section 3.5.3. The higher order ionospheric effects are not determined by equation (2.5), although they have been shown in Klobuchar (1996) to be less than 1% of the total ionospheric error even under extreme conditions.

Ionospheric scintillations are rapid variations in the phase and amplitude of signals that results from density irregularities in the ionosphere. The major effects of scintillations are an increase in the errors for code and carrier phase measurements, as well as a higher probability of losing lock on the satellite (Knight and Finn, 1998). Scintillation effects are largest in the equatorial (10-20° geomagnetic latitude), auroral (65-75°), and polar cap (> 75°) regions. However, during geomagnetic storms the auroral oval moves towards the equator, and can lead to scintillation effects as far south as the United States and northern Europe (Skone, 2001).

The magnitude of the ionospheric error is proportional to the total electron content (TEC), which varies during the solar cycle. During the solar maximum, the TEC is 2-3 times larger than during the solar minimum (Klobuchar et al., 1995). The current solar maximum has led to increased storm activity, which should peak in 2001-2003 (Skone et al., 2001). The number of major magnetic storms increases by a factor of 6 under solar maximum conditions, as compared to the solar minimum (Kunches, 1997). The data used in this research was collected in 2000-2002, so it has been affected by the increased TEC in the atmosphere. It was shown in Skone (1998) that the temporal stability of the ionospheric error was degraded under active ionospheric conditions.

**2.5 Tropospheric Error**

The troposphere is the portion of the atmosphere extending up to 60 km above the earth's surface. Approximately 80-90% of the delay is due to the wet portion of the troposphere which is contained within the first 10 km. However, this is the most difficult portion to model due to the variability in the atmospheric conditions. The wet tropospheric delay is affected by factors such as temperature, pressure, humidity, and satellite elevation (Qui, 1993). The other part of the tropospheric delay is the dry delay, which is primarily due to oxygen and nitrogen in the atmosphere. At the zenith, the dry delay is 2.3 m, while the wet delay is 1-80 cm (Spilker, 1996b). The total error increases more than 10 times as the satellite gets closer to the horizon (Seeber, 1993).

In differential positioning with short inter-receiver distances, the tropospheric delay is significantly reduced. Unfortunately, in single point or differential positioning with a long inter-receiver distance the troposphere can lead to increases in the position errors. Since the troposphere is not dispersive at GPS frequencies, a model must be used to estimate the tropospheric effect. Some of these models include: the Hopfield model (Hopfield, 1969), the modified Hopfield model (Goad and Goodman, 1974), and the Saastamoinen model (Saastamoinen, 1973). Goad and Goodman (1974) showed that the modified Hopfield model gives the best results for low elevation satellites. Each of these models gives similar results for satellites above 20 degrees. The dry part of the tropospheric delay can be estimated to a few millimetres using a model, while the estimation of the wet portion is much less accurate. The models are only accurate to 10-20% for the wet part of the tropospheric delay.

**2.6 Multipath**

Multipath is the phenomenon whereby a signal is reflected or diffracted from various objects and arrives at the receiver via multiple paths (Braasch and Van Graas, 1991). An example of this effect is shown in Figure 2.1. As a result, it is highly dependent upon the

conditions surrounding the receiver antenna and the type of antenna that is used (Raquet, 1998). Depending on the delay, a GPS receiver cannot always distinguish between a direct and reflected signal. As a result, the receiver takes the measurement based on the combined signal rather than the direct signal causing the multipath error. This makes multipath a difficult error to remove, because there is no model that can be used for the general case (Ray, 2000).
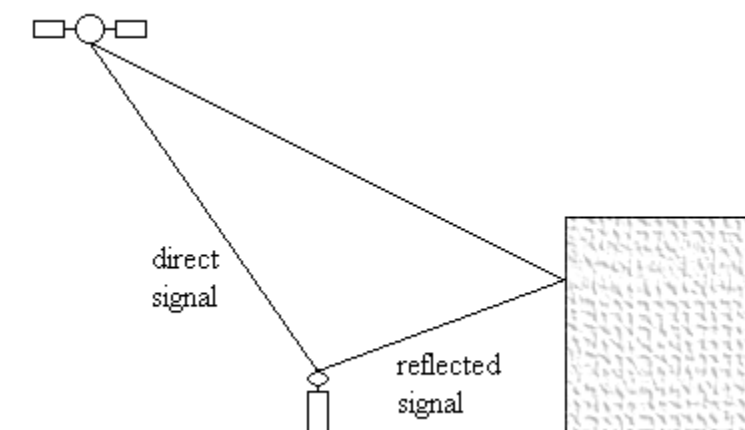


Figure 2.1: Multipath

If a high quality receiver is used, under the most severe conditions multipath can reach 15 m for code measurements and ¼ wavelength for phase observations (Ray, 2000). This corresponds to 5 cm for L1 phase and 6 cm for L2 phase. Typical levels of multipath are up to 3 m for the code measurement, and about 0.5 cm for phase. Improvements in GPS receivers have decreased the errors due to multipath. Some of these improvements include: narrow correlator spacing (Van Deirendonck et al., 1992), Multipath Elimination Technology (MET) (Townsend and Fenton, 1994) and Multipath Estimating Delay Lock Loops (MEDLL) (Townsend et al., 1995). A comparison of these technologies was done in Lachapelle et al. (1996a) demonstrating the improvement in a marine environment. It was found that MEDLL was the most effective method at reducing multipath, although MET also had a positive effect.

The simplest approach to reducing multipath is to avoid multipath environments. Choosing antenna sights that are not near any structures that could cause multipath is the best way to avoid it. Also, antenna hardware such as choke rings and ground planes have been found to be quite effective for reducing multipath (Lachapelle, 1989). The GPS-600 antenna produced by NovAtel takes into account the polarization of the signals to reduce the level of multipath (NovAtel, 2000). This antenna was used to collect the GPS data in this thesis.

## 2.7 Receiver Noise

Receiver noise is any noise that is generated by the receiver itself while taking measurements. This noise is considered to be white noise in GPS receivers for a typical sampling interval. The noise is not correlated between the GPS code and carrier phase measurements since each uses a different tracking loop. The noise is principally caused by tracking loop jitter (Raquet, 1998).

Typically, the level of receiver noise is less than 1% of the wavelength. In Raquet (1998) the carrier phase noise level was shown to have a maximum standard deviation of 0.8 mm for L1 and 1.3 mm for L2 for a high-grade receiver. It was also shown that the noise level of the code and carrier phase measurements decreases as the elevation angle increases up to about 45°, where it becomes constant. The code measurement noise level decreases from 58 cm to 15 cm as the elevation increases.

The requirements given in Chapter 1 specify the need for centimetre level positioning over time. Given the requirement and the noise level of code measurements, carrier phase techniques are needed. However, the application has a requirement that it must be able to operate in single point mode, which means that standard differential carrier phase approaches cannot be applied. For this reason, a combination of code and carrier phase

measurements are used whereby the code gives absolute range information, and the carrier phase provides accurate changes in the range.

## 2.8 Impact of Geometry

The accuracy of GPS positions is dependent on two factors. These are the accuracy of the range measurement and the geometric configuration of the satellites used in the solution. The accuracy of the range measurements is based on the errors discussed earlier. The relationship between position accuracy and the range measurement accuracy is given in Seeber (1993) as:

$$\sigma_p = DOP * \sigma_r \qquad\qquad (2.6)$$

where:

$\sigma_p$      standard deviation of point position (m),

DOP    dilution of precision (DOP), (unitless), and

$\sigma_r$      standard deviation of range measurement (m).

The DOP is a quantity computed from the covariance matrix used in GPS positioning. It can be calculated in any direction such as northing (NDOP), easting (EDOP) or height (VDOP). The time dilution of precision (TDOP) also can be determined. By combining the various DOP values, the three-dimensional dilution of precision (PDOP) and geometric DOP (GDOP) are found. The GDOP is the combination of the three-dimensional and the time dilution of precision. A derivation of the DOP values is given in Seeber (1993). A typical PDOP is 1.5-4.0, which will have an impact on this application. The changes in the measurement errors multiplied by the PDOP will give the change in the position errors. The EDOP and NDOP typically vary from 0.8-2.0, while the VDOP is much higher, with a range of 1.3-3.8.

**CHAPTER 3**

**METHODOLOGY**

**3.1 Carrier Smoothing Algorithm**

Standard carrier-smoothed code measurement uses the accurate range differences derived from the carrier phase to complement the instantaneous pseudorange measurements and thereby reduces the noise (Hatch, 1986). This involves weighting the code and carrier phase using a sliding scale as given below (Lachapelle et al., 1986):

$$\hat{P}_i = W_1 P_i + W_2 \left( \hat{P}_{i-1} + \left( \Phi_i - \Phi_{i-1} \right) \lambda \right) \tag{3.1}$$

where:

$\hat{P}_i$      smoothed range at $T_i$ (m),

$\hat{P}_{i-1}$      smoothed range at $T_{i-1}$ (m),

$P_i$      pseudorange at $T_i$ (m),

$\Phi_i$      phase measurement at $T_i$ (cycles),

$\Phi_{i-1}$      phase measurement at $T_{i-1}$ (cycles),

$W_1$      weight of the pseudorange measurement

$W_2$      weight of the carrier phase predicted range, where $W_2 = 1 - W_1$, and

$\lambda$      wavelength of the carrier wave (m).

In the above equation, the pseudorange weight is gradually decreased from 1 to 0.01 (i.e. 100% to 1%). Although this method works well in practice, since there is partial weight on the code, it does not generally give centimetre-level results over time. As mentioned in Chapter 2, the standard deviation of the noise level of code measurements is 15-58 cm depending on the elevation, which causes inadequate results from equation (3.1). It should also be noted that there is divergence over time associated with this equation since

the code and carrier phase observations are affected by the ionosphere by the same magnitude but with the opposite sign. This can be alleviated by resetting the code and carrier weights at regular intervals that can be determined by the level of the ionosphere. However, this still leads to changes in the position errors before the weights are reset.

In the proposed approach used herein, the carrier phase is fully weighted such that the code measurement only provides the initial range information. In this case, the ambiguity can be removed since the carrier phase measurements are differenced between epochs. Equation (3.2) is used because the noise level of the new measurement is based only on the noise level of the carrier phase measurements, which is less than 1 mm. The resulting equation is:

$$\hat{P}_1 = P_1 \qquad\qquad \text{first epoch}$$

$$\hat{P}_i = P_{i-1} + \left(\Phi_i - \Phi_{i-1}\right)\lambda \qquad\qquad \text{thereafter} \qquad\qquad (3.2)$$

The current generated range measurement is therefore the sum of the previous raw code measurement and the range difference in cycles computed from the carrier phase. This is equivalent to resetting equation (3.1) every epoch with $W_2 = 1$. $P_{i-1}$ is simply the code measurement given by the receiver during the previous epoch. For this reason the accuracy of all generated measurements is dependent on the previous epoch's code measurement. The noise of the computed range is much less than from equation (3.1) since the total weight is on the carrier, however there will be a bias of which the magnitude is a function of the initial pseudorange error. Figure 3.1 shows a flow chart of the smoothing methodology of the measurements and positions.
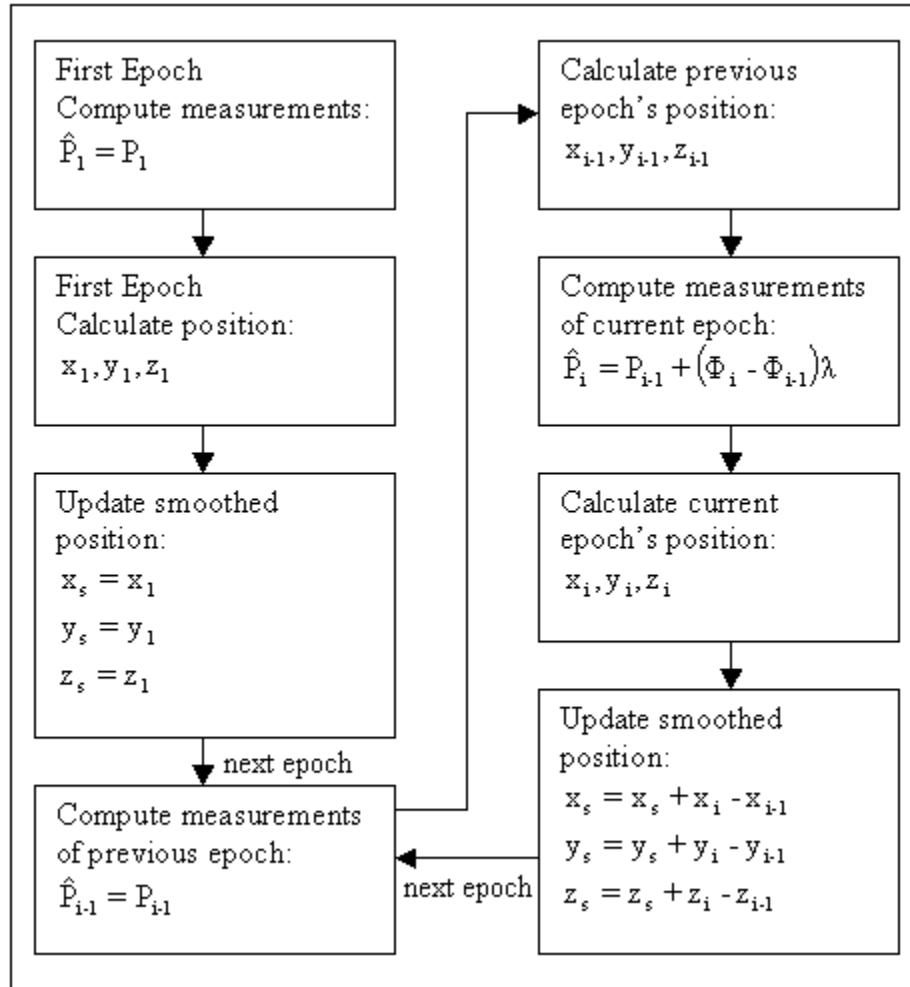
Figure 3.1: Flowing chart of carrier phase and position smoothing methodology

## 3.2 Removing Position Jumps

To ensure the relative positions over time are meaningful, position jumps must be removed from the results. There are several causes for these jumps, such as changes in the satellite geometry. Other factors are a change in the broadcast ephemeris used, and undetected small cycle slips.

It should be noted that this method is for single point positioning, but can be used for differential positioning as well. It does not attempt to explicitly determine a float or fixed

solution for the integer ambiguities. Alternative methods have been used in fixed-integer ambiguity differential position mode to take temporal correlations into account. Methods in Radovanovic (2001) and Howind et al. (1999) take temporal effects into account in the covariance matrices in determining the double-difference ambiguities.

### 3.2.1 Changes in the Satellite Geometry

If a satellite is acquired or lost there is a jump in the computed GPS position and in the DOP values of the solution (Bruton, 2000; Brozena and Childers, 2000). This is because there are different observations in the least squares adjustment if a satellite is acquired or lost. Since a least squares adjustment minimizes the square of the residuals of the observations, the results are different when the observations are different. A method to mitigate the jumps using predicted positions is proposed in Zhodzishsky et al. (1999). This algorithm was proposed when SA was still a major factor, and a less complicated algorithm is used here. Other methods can be used which average the velocity before and after the data point to try to determine the change in position. This method is much noisier than using the carrier phase measurement to compute the position.

The proposed algorithm is as follows:

1.  Compute the position solution at the first epoch ($T_0$), using only code measurements.
2.  Compute the carrier smoothed measurement at ($T_1$), using measurements given by equation (3.2).
3.  Compute the position solution at ($T_1$), using the carrier smoothed measurements.
4.  If the satellites are the same for the two solutions add the differences in the positions computed by $T_1$-$T_0$ to the code solution from $T_0$. Repeating steps 1-4 for each epoch will give a time series in which the position errors change very little over time.

To remove position jumps in the case of satellite changes a number of cases must be considered. These include:

a.      A new satellite is used at $T_1$ that was not used at $T_0$

b.      A satellite used at $T_0$ is lost at $T_1$

c.      A new satellite is used at $T_1$ that was not used at $T_0$, and a satellite used at $T_0$ is lost at $T_1$

In case (a), the position is recomputed for the measurements at $T_1$ using the same satellites observed at $T_0$. The new satellite is not used in recomputing the solution at $T_1$. After this, the difference between the new solution at $T_1$ and the solution at $T_0$ is added to the code solution at $T_0$.

Case (b) requires the opposite method of case (a). In case (b), the position is recomputed for the measurements at $T_0$ using only the satellites available at $T_1$. The lost satellite is not used in recalculating the solution. After this, the difference between the solution at $T_1$ and the new solution at $T_0$ is added to the code solution at $T_0$.

Removing the position jump in case (c) requires a combination of what is done in case (a) and (b). The positions at $T_0$ and $T_1$ should be recomputed using only the common satellites available at both epochs. After the positions are recomputed, the difference between the new solutions at $T_1$ and $T_0$ is added to the code solution at $T_0$.

## 3.2.2 Changes in the Broadcast Ephemeris

When a new broadcast ephemeris is used, the satellite coordinates typically change by up to a few metres. This change will cause a jump in the computed GPS position. To prevent this, the first measurement is removed from the least-squares adjustment when a satellite has a new broadcast ephemeris. Based on the algorithm described in Section 3.3.1, this means the solution for the previous epoch will be recomputed with the relevant satellite removed.

The software used in this application is a post-mission software package. This allows the program to select the closest ephemeris, rather than just the most recent one. It is possible using the algorithm described above that many satellites would be removed in the same epoch, leading to no position being computed. To prevent this, an offset of up to 30 seconds, depending on the identification number of the satellite, has been incorporated into selecting the closest ephemeris.

### 3.2.3 Undetected Cycle Slips

In order to ensure there have not been cycle slips in the carrier phase measurements, a detection filter is implemented. The filter predicts the phase measurement using the previous phase and Doppler measurements. The equation for computing the predicted phase measurement is the following:

$$\Phi_{pred} = \Phi_{i-1} + \frac{\left(\dot{\Phi}_i + \dot{\Phi}_{i-1}\right)}{2}\Delta t \qquad (3.3)$$

where:

$\Phi_{pred}$    predicted phase measurement (cycles),

$\Phi_{i-1}$    phase measurement at previous epoch (cycles),

$\dot{\Phi}_i$    Doppler measurement at current epoch (cycles/s),

$\dot{\Phi}_{i-1}$    Doppler measurement at previous epoch (cycles/s), and

$\Delta t$    time difference between current and previous epochs (s).

The filter flags a cycle slip if the difference between the predicted and actual phase measurement is greater than a specified threshold. For the static data in this investigation a threshold of 3.5 cycles is used. However, it is possible for cycle slips of less than 3.5 cycles to occur. A cycle slip of 3.5 cycles on L1 is 66 cm, which is an error of a large enough magnitude to cause a position jump. To remove the observation in this case, the

residuals are compared for two epochs to ensure they are less than 0.02 cm apart. The 0.02 cm value was determined empirically, by testing the software. In a case involving significant vehicle dynamics this value is increased, as well as the cycle slip detection threshold.

## 3.3 Limitations

All of the algorithms in Section 3.2 have been implemented in the GPS software package $C^3NAVG^2$ (Petovello et al., 2001) as extensions to the original software. The one limitation of the proposed algorithm is if there are not enough satellites to compute a position. Typically, five satellites are needed to compute an accurate position. In most cases there are at least five GPS satellites in view so this is not a problem. However, sometimes a cycle slip can occur on all of the satellites, so there are no satellites in the solution. Another possibility is that the signals from several satellites are blocked, so there are less than five satellites available. Signal blockage is generally not a concern in airborne magnetometry, but it is in cases such as urban vehicular navigation (Lachapelle et al., 1997).

Normally, the three dimension position components are determined, in addition to the receiver clock error. Since there are four estimated quantities, five satellites are needed to have one degree of freedom, which permits an analysis of the residuals to ensure errors are detected. For the algorithm described in Section 3.2, if a position cannot be computed, the algorithm simply starts again by resetting. A position jump would occur at the point where a position cannot be computed, followed by normal execution of the program. This means that the data across the position jump cannot be used, as it is not a precise relative position.

In March 2002, it was announced that the European Union will develop a satellite based positioning system named Galileo. The technical details of the Galileo system are being finalized, and the system designers intend to make it interoperable with GPS (EU, 2002).

Simulations of proposed satellite constellations have shown that Galileo will provide improved reliability and geometry if used in conjunction with GPS (O'Keefe, 2001). This would reduce the likelihood of a position not being computed for the proposed algorithm.

## 3.4 Error Source Analysis

An objective of this thesis in to analyze the temporal characteristics of GPS error sources in order to determine the best processing method for obtaining precise relative single point positions. To analyze the error sources in this thesis three main techniques are used. One is computing the RMS of the change in the error in the over many time intervals. The error is computed first using the methods described later in this chapter, and then a time series of the changes in the error can be calculated for any interval of interest. The time series used in calculating the RMS contains the changes in the errors of all possible satellites for the given interval. For the application, the time intervals of most interest for the RMS values are 2-50 seconds. To further analyze the errors, intervals of up to 30 minutes are investigated.

A second method involves an analysis of the time correlation of the errors. To give results which can be compared most easily, unbiased data sets were used. An unbiased data set means the mean has been removed. As with the RMS analysis, time intervals of 2-50 seconds, and 1-30 minutes will be examined. The autocorrelation of a data set is found by using the following formula (Press et al., 1988):

$$\varphi(\tau) = \int_{-\infty}^{\infty} g(\tau)g(\Delta t + \tau)d\tau$$

(3.4)

where:

g        data set (m)

$\tau$        time of observation (s)

$\Delta t$        time lag (s).

The third method investigates the error in the frequency domain. The power spectral density is the magnitude of the Fourier transform of the data squared. Again, unbiased data sets are used in determining the power spectral density. To better compare the results in the frequency domain, the cumulative power up to a particular frequency was found. The algorithm used to compute this quantity is as follows:

1.  Compute the power spectral density at all frequencies.
2.  Use the trapezoid rule to estimate the power between each two consecutive frequencies.
3.  Find the total power by summing the results in step 2.
4.  Divide the results in step 2 by the sum in step 3 and multiply by 100 to obtain a percentage.
5.  Find the cumulative total for any given frequency by adding all the results from step 4 below the frequency of interest.

## 3.4.1 Orbital Error Computation

The orbital error in this thesis will be determined by comparing the computed orbits based on the broadcast ephemeris with those computed using the precise ephemerides. The broadcast orbits are computed using the equations described in Spilker (1996a). Precise orbits are computed by fitting a ninth-order Lagrange polynomial to the nearest ten data points, which are spaced at 15 minute intervals. Details on the implementation of a Lagrange polynomial are given in Cheney and Kincaid (1994). As mentioned earlier, the final orbits obtained from NRCan are accurate to 5 cm. The result from subtracting the precise orbits from the broadcast values gives coordinates in the Earth-Centred-Earth-Fixed (ECEF) frame. To better analyze the results, the orbits are converted into the Satellite-Centred-Satellite-Fixed (SCSF) frame. Figure 3.2, given in Beutler (1998), shows the SCSF frame. In the SCSF frame, the x, y, and z components refer to across-track, along-track, and radial directions, respectively.
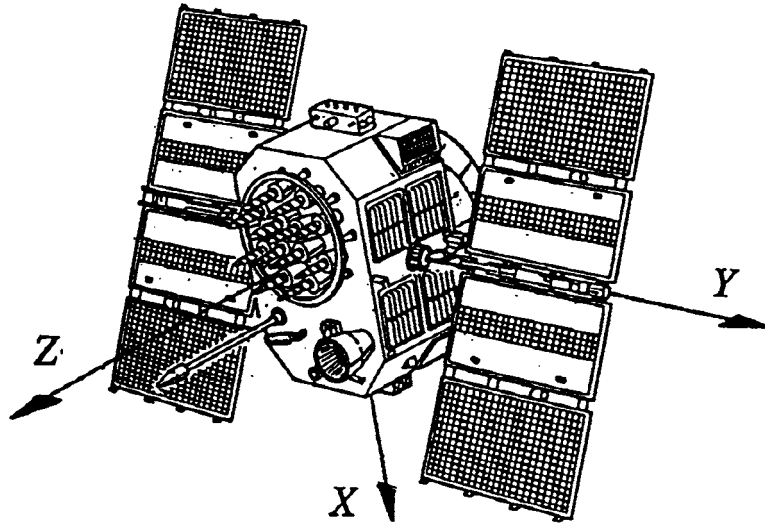
Figure 3.2: Satellite-Centred-Satellite-Fixed reference frame (Buetler, 1998)

To convert the results from ECEF to SCSF, the following equations given in Fortes (2002) are used. First, rotate the coordinates to radial, along-track, across-track:

$$\begin{vmatrix} x'_{PC} \\ y'_{PC} \\ z'_{PC} \end{vmatrix}_{SCSF} = R_3(\varphi)R_1(i)R_3(\Omega) \begin{vmatrix} x_{PC} \\ y_{PC} \\ z_{PC} \end{vmatrix}_{ECEF} \qquad (3.5)$$

where:

$\varphi$      argument of latitude (radians)

$i$      inclination of orbit (radians), and

$\Omega$      longitude of the ascending node (radians).

Next, the precise orbits need to be corrected for the satellite antenna offsets (see Appendix A for values) and converted into the coordinate system as shown in Figure 3.2. To convert to across-track, along-track, radial, and to correct for difference in the satellite antenna offsets the following relationship is used:

$$\begin{vmatrix} x_{CM} \\ y_{CM} \\ z_{CM} \end{vmatrix}_{SCSF} = \begin{vmatrix} -z'_{PC} \\ -y'_{PC} \\ -x'_{PC} \end{vmatrix}_{SCSF} + \begin{vmatrix} \Delta x \\ \Delta y \\ \Delta z \end{vmatrix} \qquad (3.6)$$

where:

$\Delta x$     across-track satellite antenna phase center offset (m),

$\Delta y$     along-track satellite antenna phase center offset (m), and

$\Delta z$     radial satellite antenna phase center offset (m).


**3.4.2 Satellite Clock Error Computation**


The satellite clock error is computed in much the same way as the orbital error. The broadcast satellite clock error is determined using equation (2.4). Precise orbits are computed by fitting a ninth-order Lagrange polynomial to the nearest ten data points, which are spaced at 30 second intervals. As mentioned previously, the precise clock corrections used in this thesis were computed and determined by NRCan. They offer two types of final precise clocks: Canadian and global clocks. Canadian clocks are available only for satellites in view over Canada. For this reason, the clock corrections do not exist for every clock at all times. When interpolating the precise clock correction error herein, the value is only computed if the ten closest data points are less than 200 seconds from the data point.


**3.4.3 Ionospheric Error Computation**


Errors due to the ionosphere are computed using the L1 and L2 phase measurements. Code measurements could be used, but the noise of the pseudorange measurement is much larger than the ionospheric error over short time intervals. This analysis does not use the absolute ionospheric errors, since the ambiguities of the L1 and L2 phase measurements are unknown. For this investigation, the ambiguity terms were neglected,

since only the change over time is desired. The following equation in Kaplan (1996) is used to determine the first-order ionospheric advance:

$$d_{ion} = \frac{f_2^2}{f_1^2 - f_2^2}\left(\Phi_1\lambda_1 - \Phi_2\lambda_2\right)$$ (3.7)

where:

f        is the carrier frequency of L1 or L2 (Hz),

λ        is the wavelength of L1 or L2 (m), and

Φ        is the carrier phase measurement on L1 or L2 (cycles).

Cycle slips must be removed from the data using equation (3.3) for the analysis to be meaningful. Once the ionospheric advance is computed for each epoch, the time series can be analyzed for each satellite.

### 3.4.4 Remaining Error Computation

Errors due to the tropospheric error, multipath, and noise are computed by removing the other errors from the observations, since these cannot be easily isolated. This is done through the following procedure:

1.        Use precise orbits and clocks to determine the satellite coordinates and satellite clock error. Compute the estimated range between the satellite and the receiver by the following:

$$\rho = \sqrt{\left(x_s - x_a\right)^2 + \left(y_s - y_a\right)^2 + \left(z_s - z_a\right)^2}$$ (3.8)

where:

$\rho$                                computed geometric range (m),

$x_s, y_s, z_s$            satellite coordinates (m), and

$x_a, y_a, z_a$            receiver antenna coordinates (m).

2.      Use dual frequency phase measurements to determine the first order ionospheric effects using equation (3.7). To give valid results the data must be free of cycle slips. It be noted that higher-order ionospheric effects will remain in the estimation of the remaining error. It should also be noted that the remaining error will be a relative, rather than absolute, quality.

3.      Estimate the receiver clock error by using the receiver as a reference station in differential GPS processing. This is valid when the data is collected at a known point, since it allows the position to be fixed. To ensure a smoothly changing satellite clock the constellation must be the same. This is done with the method detailed in Section 3.2.1.

4.      If desired, determine the theoretical tropospheric correction. In this thesis the modified Hopfield model is used to calculate the tropospheric correction. The partial pressure of the water vapor is computed using the method in Himmelblau (1974).

5.      To determine the remaining errors, remove the estimated range, ionospheric advance, tropospheric delay, satellite clock correction, and receiver clock error from the phase measurement. The total equation is as follows:

$$\Delta\Phi = \lambda\Phi - \rho + c(dt - dT) + d_{ion} - d_{trop} \tag{3.9}$$

It should be noted that the remaining errors could be investigated before and after a tropospheric correction. The difference in the results will give an indication of the nature of the tropospheric error. However, the remaining errors after a tropospheric correction will still contain noise, multipath, higher-order ionospheric effects, and the error in the tropospheric correction model.

## 3.5 Real-Time Software

A modified version of the $C^3NAVG^2$ software, which incorporates the algorithms described above, has been developed for real-time operation. Since the precise clocks and orbits are not available for real-time positioning they are not part of this software. An ionospheric correction is used, as well as the carrier smoothing algorithm described in Section 3.2. The only other difference from the post-mission software is that the most recent, rather than the closest, navigation message is used in computing the broadcast satellite coordinates and clock correction. The effect of this would be largest just before a new navigation message is received, since the message being used would have a time of ephemeris almost two hours different than the observations. Normally, the maximum difference would be one hour.

# CHAPTER 4

## DATA DESCRIPTION

There are three main data sets in this thesis. The first set is static data collected in November 2001 at the University of Calgary. The second data set is marine data collected on a boat in the St. Lawrence Seaway in February 2002. The final data set is airborne data collected on an airplane near San Jose in June 2000.

Precise clock corrections and satellite orbits for the same days were obtained from the Geodetic Survey Division at NRCan (Kouba and Héroux, 2001). The orbits used are updated every 15 minutes, while the clocks are updated every 30 seconds.

## 4.1 Static Land Data

Data was collected continuously from November 2 to 10, 2001 using a NovAtel OEM-4 receiver and a NovAtel 600 antenna. Raw code and phase data were collected on a fixed pillar on the roof of the Engineering Building at the University of Calgary on both the L1 and L2 frequencies at 2 Hz. At the receiver's location, the multipath environment is moderate. The coordinates of the point are known, which allows the algorithm described in Section 3.4.4 to be used.

As mentioned in Chapter 3, the quality of GPS positions is dependent on the geometry of the solution. Better geometry leads to a lower PDOP, which means the position will be more accurate. Figure 4.1 shows a plot of the PDOP on November 9, while Figure 4.2 shows the number of satellites in the solution on the same day. On this day the PDOP varied between 1.5 and 4.9, with an average of 2.05. The number of satellites in the solution varied between 5 and 10, with an average of 7.8. These numbers include all satellites above 10° elevation, and are typical for all of the days in the data set. A 10°

elevation mask was used because it is the best balance between availability and reliability of the solution. Atmospheric errors, multipath, and noise, are all increased as the elevation decreases, although the geometry is better when lower elevation satellites are used in estimating the position.
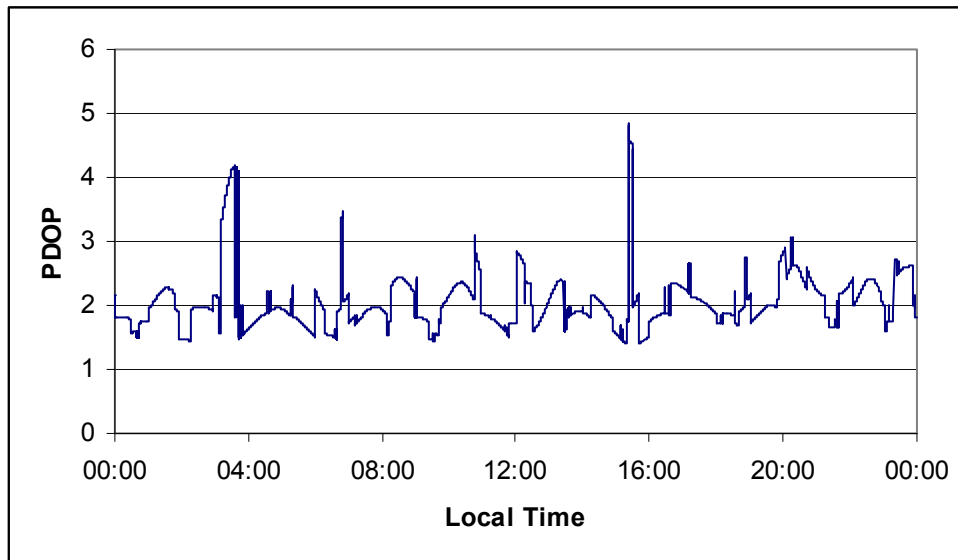


Figure 4.1: PDOP of solution on November 9
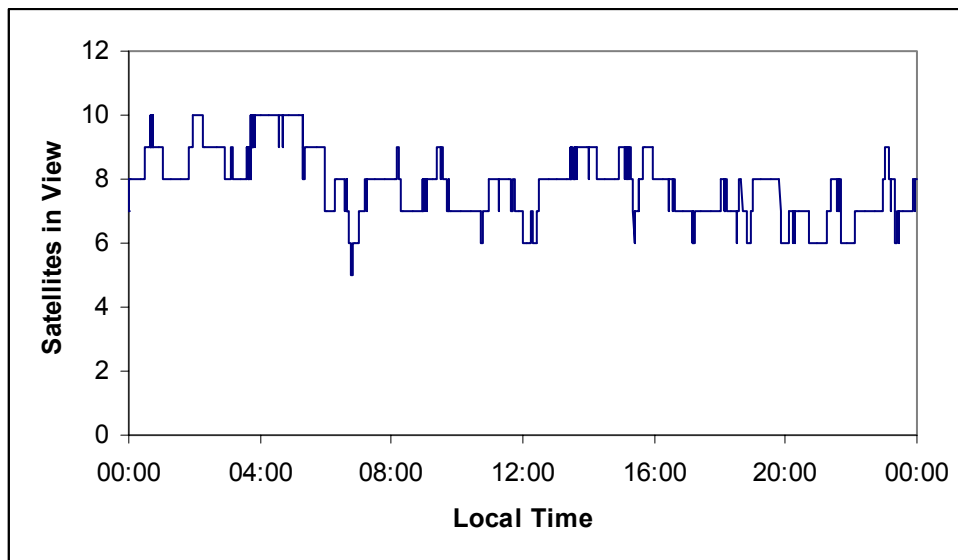


Figure 4.2: Number of satellites in view above 10° elevation on November 9

**4.2 Marine Data**

Marine data was collected on February 18, 2002 in the St. Lawrence Seaway near Trois-Rivieres, Quebec on the ship HMS Martha L. Black. This data was given by the Canadian Coast Guard, and their contribution is acknowledged here. Data was collected using a NovAtel OEM4 receiver at a 10 Hz data rate. The data was collected on both L1 and L2 frequencies from about 12:00-15:30 local time. The multipath environment was moderate at the antenna's position. Overall, the ionosphere conditions on this day were moderate. However, due to the time of day the data was collected the ionosphere has a significant effect.

For the marine data, the time period studied will be from 13:20-15:10 local time, which is when the ship was in motion. There were 4-7 satellites in view over the time period, and the PDOP varied between 1.8 and 12.1. The PDOP reached a peak of 3.3 when 5 or more satellites were in view, and the average PDOP for the data set was 2.2. Figure 4.3 shows a plot of the PDOP for the data set, while Figure 4.4 shows the number of satellites in the solution. The average number of satellites used in the position solution was 6.5.



Figure 4.3: PDOP of solution for marine data
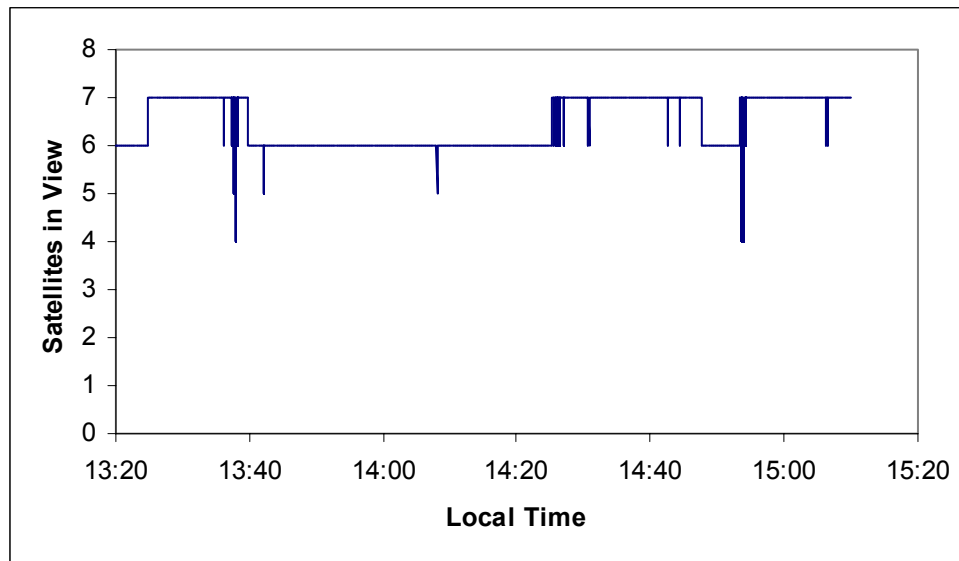
Figure 4.4: Number of satellites in view above 10° elevation for marine data

A plot of the velocity of the boat is shown in Figure 4.5, and the trajectory is given in Figure 4.6. The typical horizontal velocity of the vessel ranged from 4-8 m/s, while the vertical velocity was close to nil. The position of the boat at the first epoch has been set at the origin in Figure 4.6. The boat traveled 12 km southeast, and then returned to close to the original position. In the middle of the trip, about 9 km from the start, the boat made a loop of about 0.75 by 0.25 km. The base station's position is shown by the triangle in the upper right hand corner of the plot.
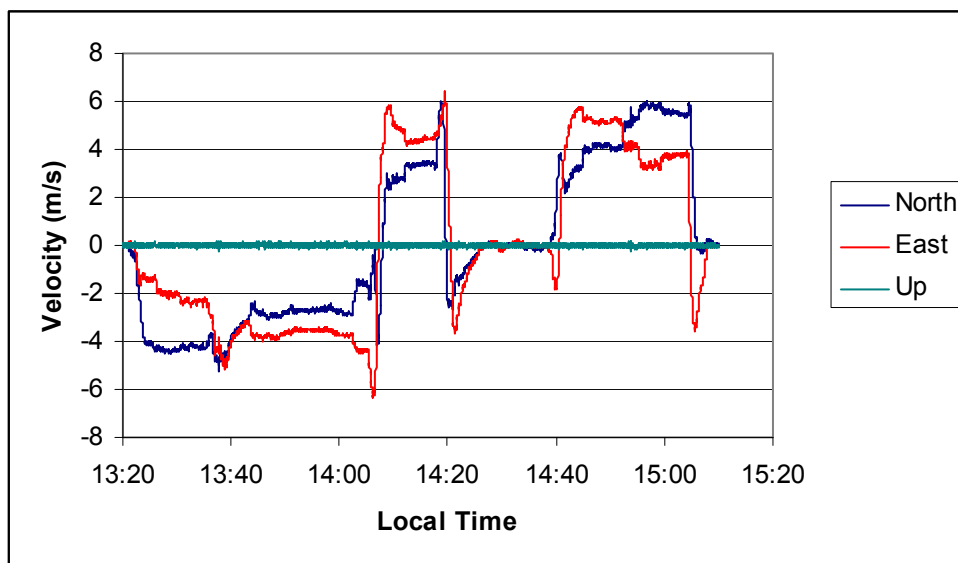
Figure 4.5: Velocity of marine data set
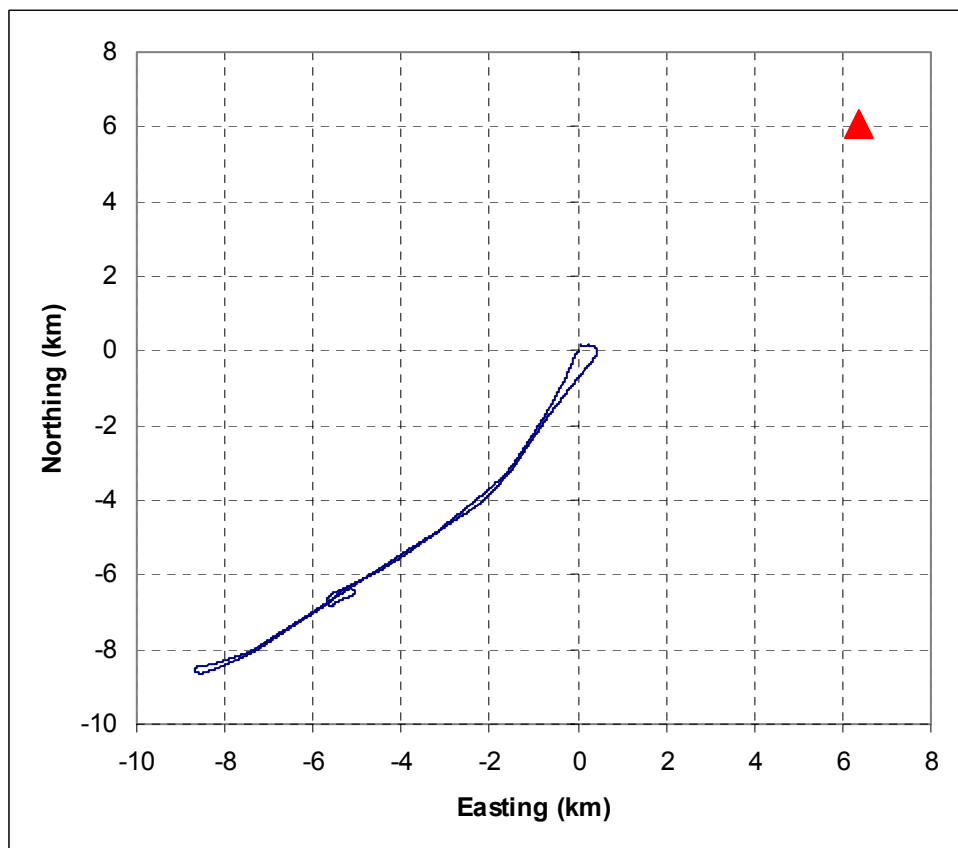


Figure 4.6: Trajectory of marine data set

**4.2.1 Marine Truth Data Determination**

To determine the position errors in the marine data a truth trajectory must be obtained. To obtain a truth position for the marine receiver, fixed integer ambiguity carrier phase differential GPS was used. The software package used to compute the truth trajectory is FLYKIN, developed at the University of Calgary. This is shown to give very good position stability over time in Figure 4.7, which was computed using data with an inter-receiver distance of 3 m, while for the marine data set the distance is up to 15 km. The errors contributing to the bias in Figure 4.7 are predominantly the changes in multipath and noise, magnified by the geometry. Since the inter-receiver distance for the marine data is much longer, the position error changes of the truth trajectory will be degraded with respect to Figure 4.7, which could lead to a computed degradation in the single point results. For the marine results the position error is computed by subtracting the FLYKIN position from the computed single point positions. This method is used because it is the change in the position errors that is of interest, rather than the absolute errors.
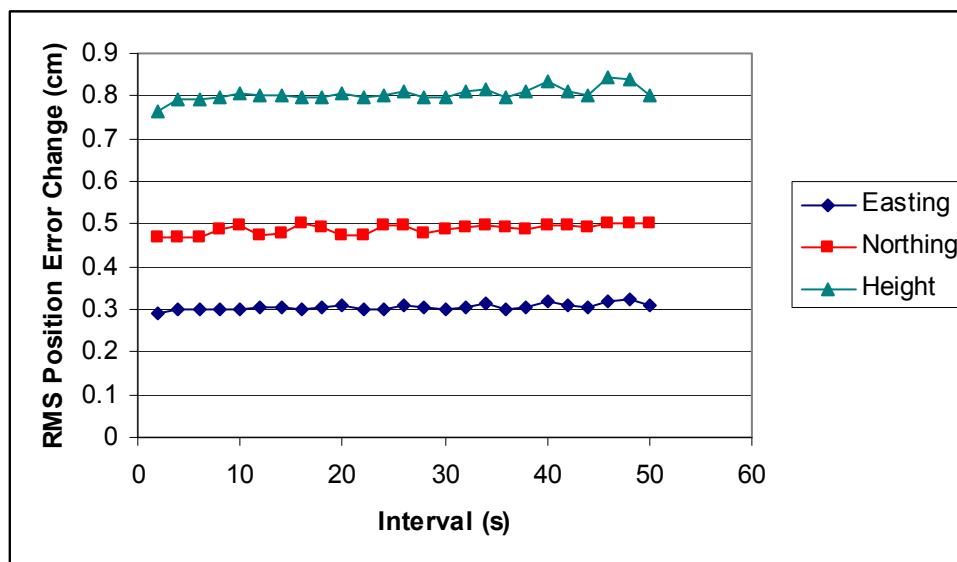


Figure 4.7: RMS position error change over time for double-differenced fixed-ambiguity positioning

**4.3 Airborne Data**

Airborne data was collected on June 22, 2000 on an aircraft doing an aerial survey near San Jose, California. Applanix is thanked for providing the aircraft data described in this section. Data was collected using a NovAtel OEM3 receiver at a 2 Hz data rate. The data was collected from 09:30-11:20, and the height of the aircraft ranged from 995 to 1155 m.

For the airborne data set, 5 to 8 satellites were in view at all times. On average, there were 6.5 satellites above 10° elevation. The PDOP of the computed GPS positions had a range of 1.6-3.9, and an average of 2.9. The PDOP is shown in Figure 4.8 and the satellites in view are given in Figure 4.9. As is clear in Figure 4.9, the satellite constellation is much more constant for the airborne data than the other two data sets. This is due to the location of the antenna, which is not blocked by the surrounding environment. The results are displayed from 09:40-11:20, which is the period in which the aircraft was in motion.

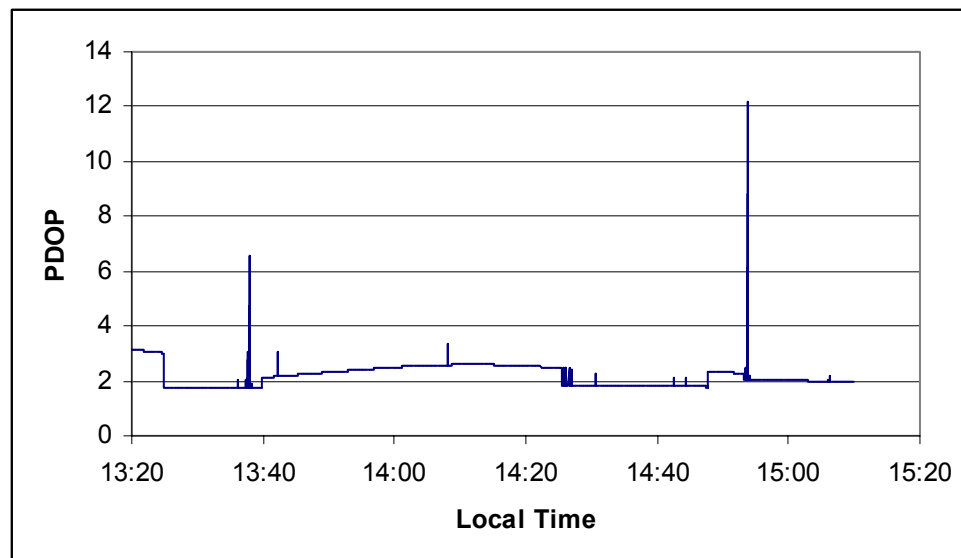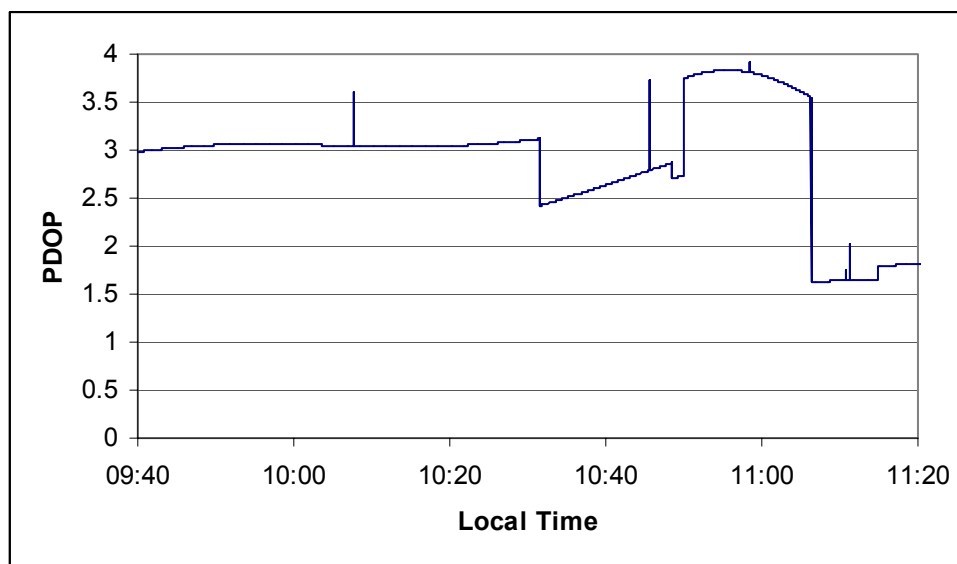

Figure 4.8: PDOP of solution for airborne data
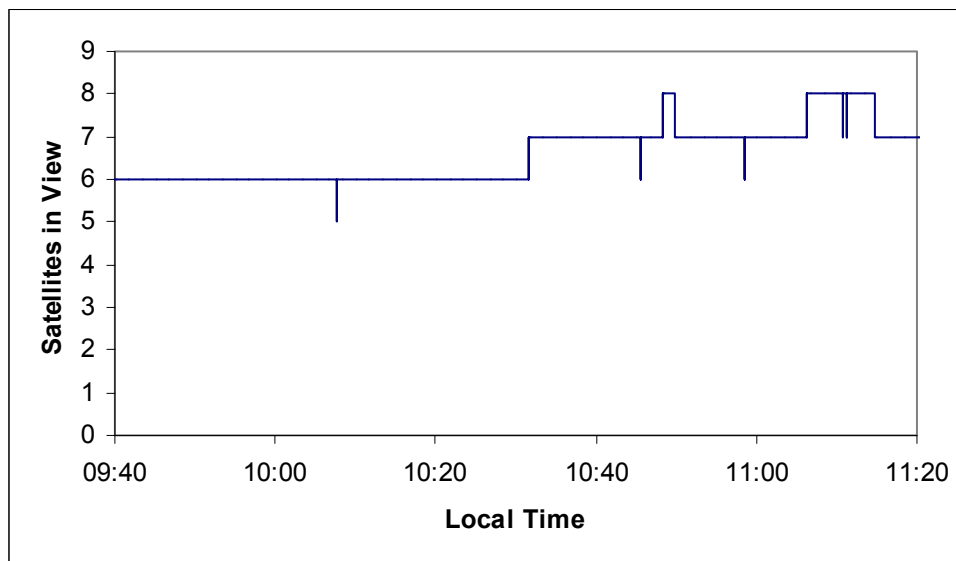
Figure 4.9: Number of satellites in view above 10° elevation for airborne data

The velocity of the aircraft is shown in Figure 4.10, while the trajectory is shown in Figure 4.11. The horizontal velocity of the aircraft typically varied between 73-81 m/s. The flight involved 11 U-turns and several flight lines. As with the marine data, the initial position of the plane has been set as the origin of Figure 4.11.
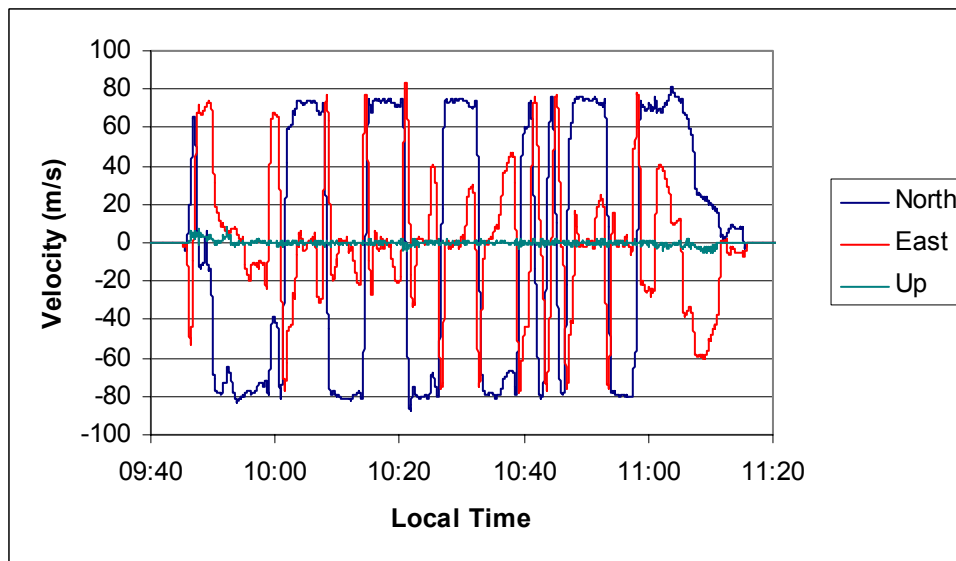


Figure 4.10: Velocity of airborne data set
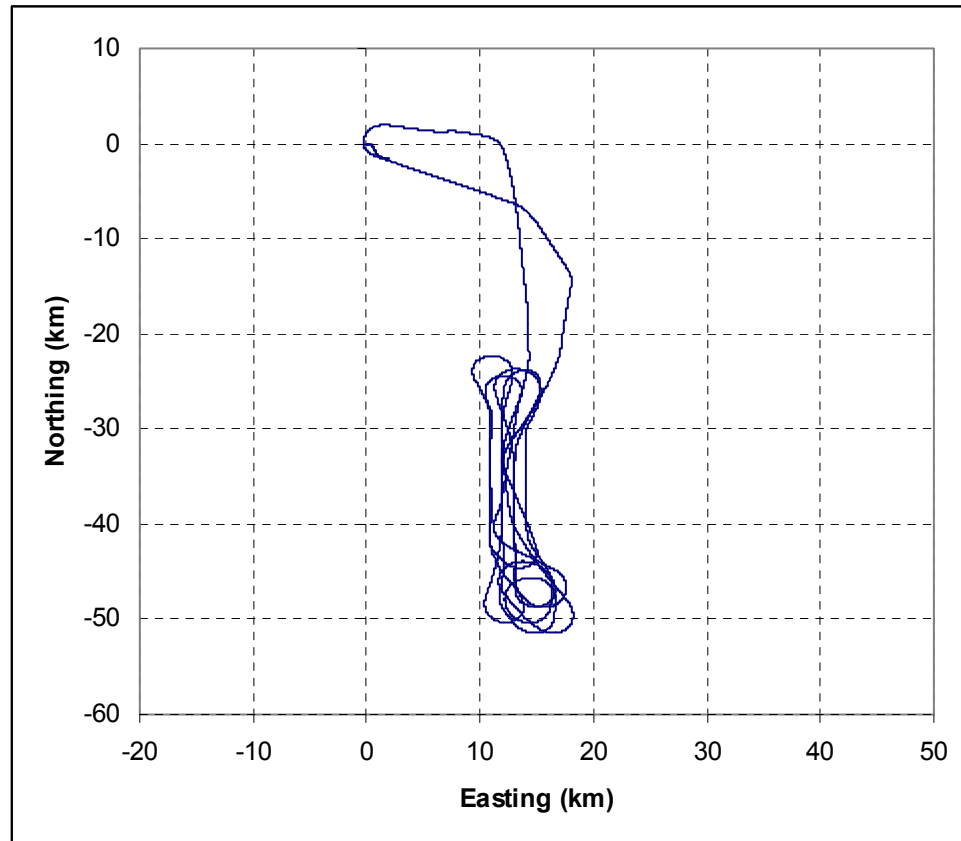
Figure 4.11: Trajectory of airborne data set

## 4.3.1 Airborne Truth Data Determination

The truth trajectory for the aircraft was determined using differential GPS with multiple reference stations. The location of the reference stations with respect to the trajectory is given in Figure 4.12 (Cannon et al., 2002). The ten reference station positions are computed using Bernese GPS Software Version 4.2 (Hugentobler et al., 2001). Once the coordinates of the reference stations were known, differential corrections were computed using the NetAdjust software package, which was developed at the University of Calgary. This software is based on the method described in Fortes (2002). The differential corrections are used by Trimble Geomatics Office Software Version 1.0 (Trimble, 1999) to determine the truth position. The results have been shown to be accurate to the 10 cm level. The solution has fixed integer ambiguities, so the effect of the errors in this

trajectory will have an effect on the computed single point position error, but only a small effect on the relative single point positions. More information about the differential position results for this data set is given in Cannon et al. (2002).
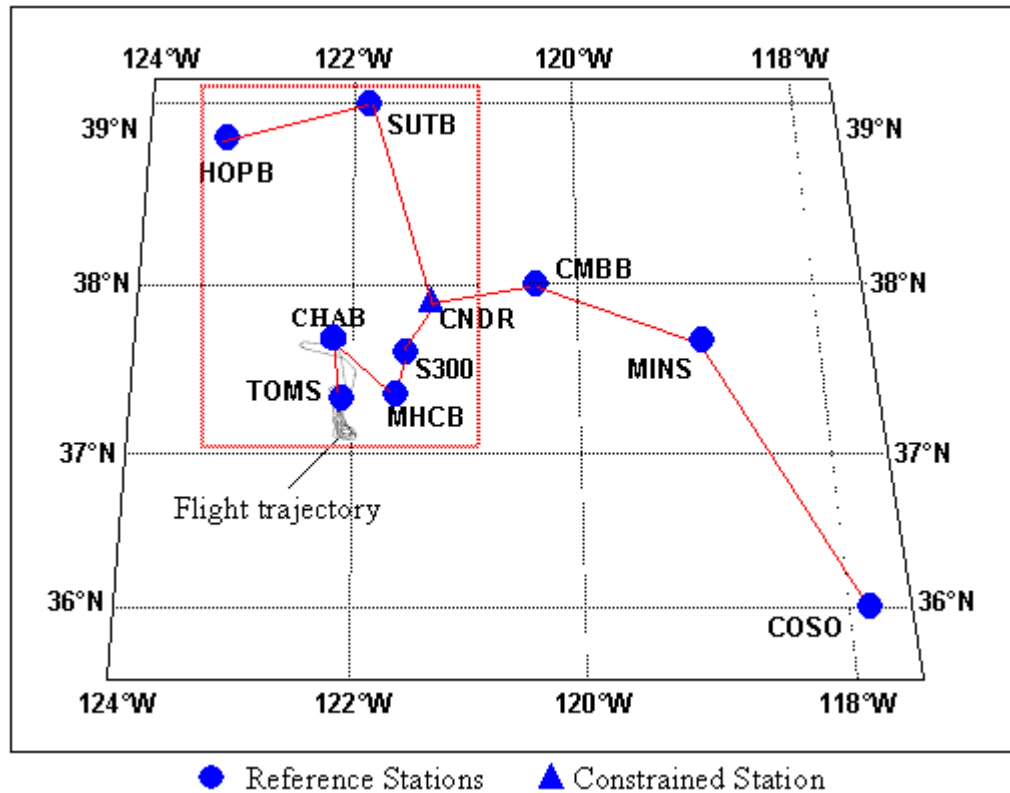


Figure 4.12: Location of Reference Stations (Cannon et al., 2002)

# CHAPTER 5

## TEMPORAL CHARACTERISTICS OF GPS ERROR SOURCES

This chapter contains an analysis of the temporal characteristics of several GPS error sources. The analysis will be done primarily of the static data collected in November, 2001. A brief discussion is also included for the marine and airborne data sets.

### 5.1 Orbital Error

The absolute orbital error for SV 4 on November 9 in all three components, as well as the three-dimensional error, is given in Figure 5.1. Errors in this plot are typical of the absolute orbital error on this day for all satellites. The discontinuities in the graph are due to a change in the broadcast ephemeris record that was used in the satellite position determination. These occur at 02:00, 04:00, and 06:00 local time. The discontinuities in the error of the across-track and radial directions average about 3 cm, as compared to an average of 60 cm in the along-track direction. The discontinuities due to a different broadcast ephemeris are omitted in the analysis of the changes over time. In the position domain, the error due to a new broadcast ephemeris can be removed, as described in Section 3.2.2. The three-dimensional error ranges from about 2.8 to 6.5 m, with clear trend of several hours. These results are consistent with those shown in Langley et al. (2000) and Fortes (2002).
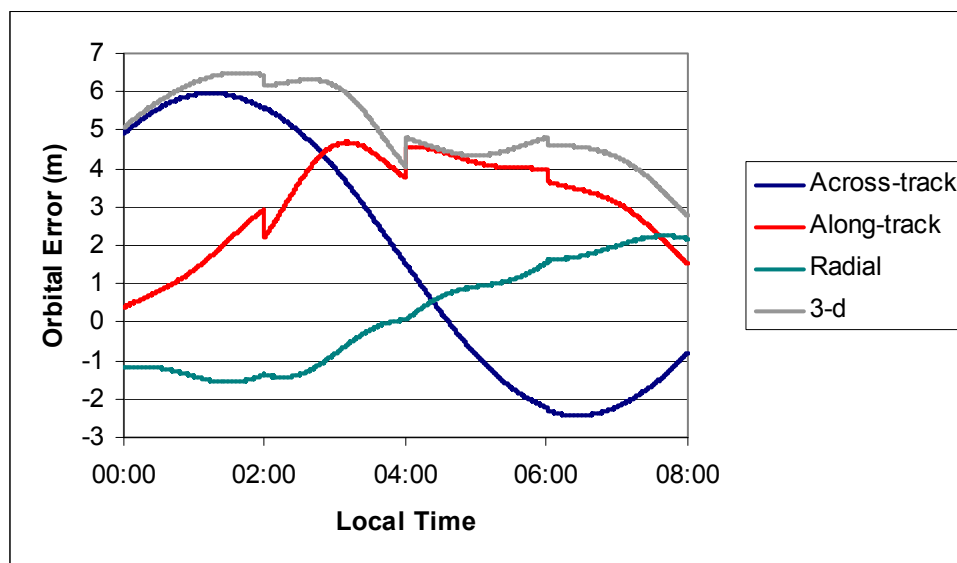
Figure 5.1: Absolute orbital error of one satellite on November 9

## 5.1.1 Temporal Variations in Orbital Error

Figure 5.2 shows the RMS of the changes in the three-dimensional orbital error over intervals of up to 50 seconds for the entire day on November 9. The results in this plot are typical of those for each day of the entire data set. Each line has a linear trend, with the RMS increasing from 0.1 to 0.2 cm over 2 seconds to 1.8 to 7.0 cm over 50 seconds. This will lead to an increase in the changes in errors over time in the position domain, with the effect being most significant over longer time periods. The two outlying satellites are SVs 6 and 23. These two satellites showed poor performance as compared to the other satellites on each day the static data was collected.

The average RMS orbital error change over time for each component on November 9 is given in Figure 5.3. The radial direction has the smallest change in errors over time, with the effect increasing to 0.8 cm over 50 seconds. The errors in the radial direction are significant, since they will transfer almost directly into a range error. The changes in the errors in the along-track and across-track components are higher, since the radial direction is the most precisely measured by the control segment (Zumberge and Bertiger,

1996).   The RMS change in the three dimensional error increases from 0.2 cm over 2 seconds to 2.8 cm over 50 seconds.
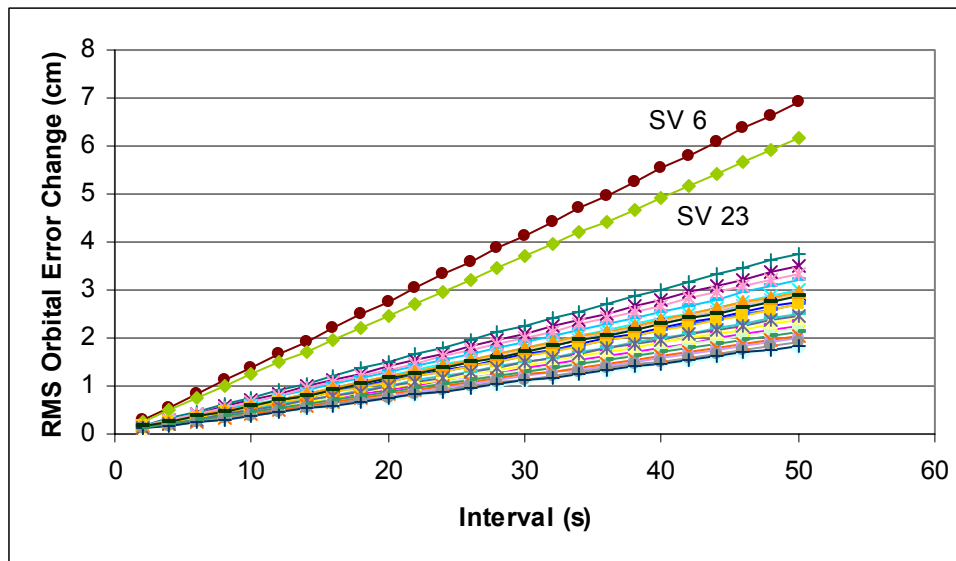


Figure 5.2: RMS three-dimensional orbital error change over time for each satellite for November 9
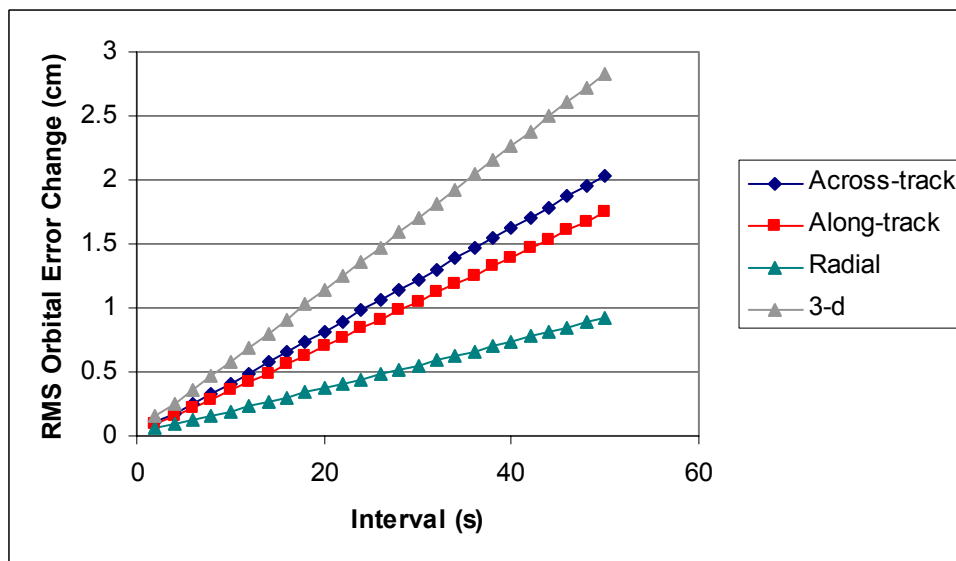


Figure 5.3: Average RMS orbital error change over time intervals of up to 50 seconds for each component on November 9

As shown in Figure 5.4, the changes in the three-dimensional orbital error are about the same from day-to-day. The range is from 0.14-0.16 cm over 2 seconds, to 0.48-0.57 cm over 10 seconds, to 2.35-3.05 cm over 50 seconds. Each day on the graph shows a linear increase as a function of the time interval.
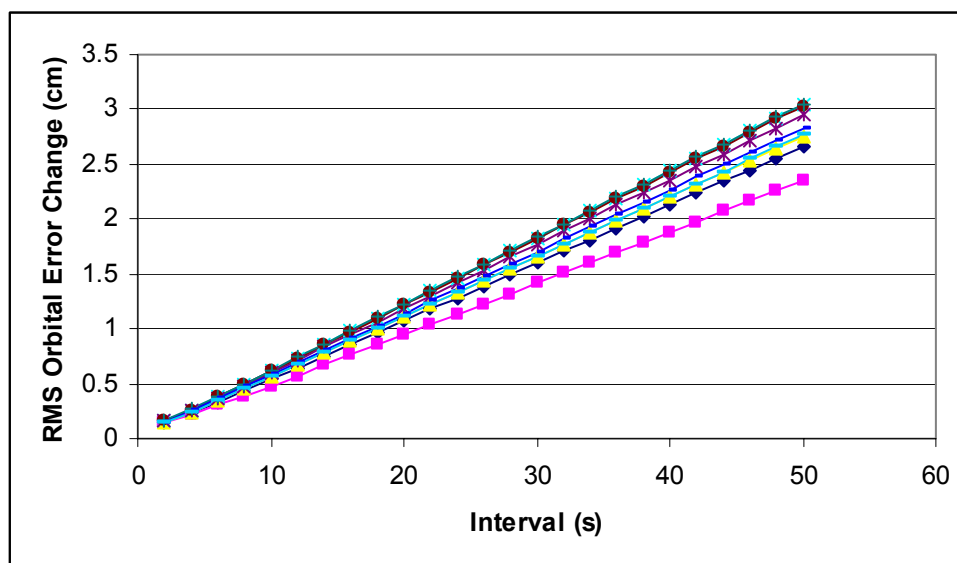


Figure 5.4: Average RMS three-dimensional error over time for each day from November 2-10

Figure 5.5 is similar to Figure 5.3, but with a maximum interval of 30 minutes. The change in the three-dimensional RMS error increases to 70 cm over 30 minutes. Once again the radial error has the smallest changes of any of the components. The changes in the errors in the radial direction show a linear increase for intervals up to 30 minutes. However, the other two components do not increase at a linear rate after a 15 minute interval. Positions computed with broadcast ephemerides will show trends in the errors of longer than 15 minutes due to the decorrelation in the orbital errors.
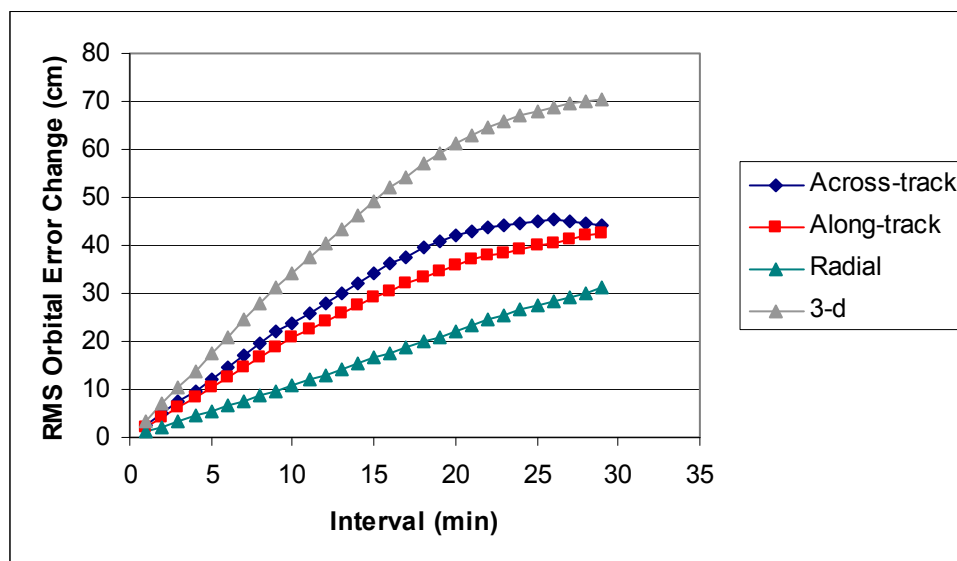
Figure 5.5: Average RMS orbital error change over time intervals of up to 30 minutes for each component on November 9

The orbital error results for the marine and airborne data sets are shown in Figures 5.6 and 5.7, respectively. Changes in the errors of the broadcast orbit results are somewhat smaller than for the static data on November 9. Since the data set in these cases is only two hours, only the satellites in view were used for the results. Satellites 6 and 23, which have the worst performance for the land data, were not in view when the marine data was collected. This is a significant cause of the differences between Figures 5.3 and 5.6. Both of these satellites were in view for the airborne data, but satellite 23 performed similarly to the other satellites. The broadcast orbit for satellite 6 for the airborne data performed much worse than the other satellites. The results for the airborne data are worse than those for the marine data over the time period studied.
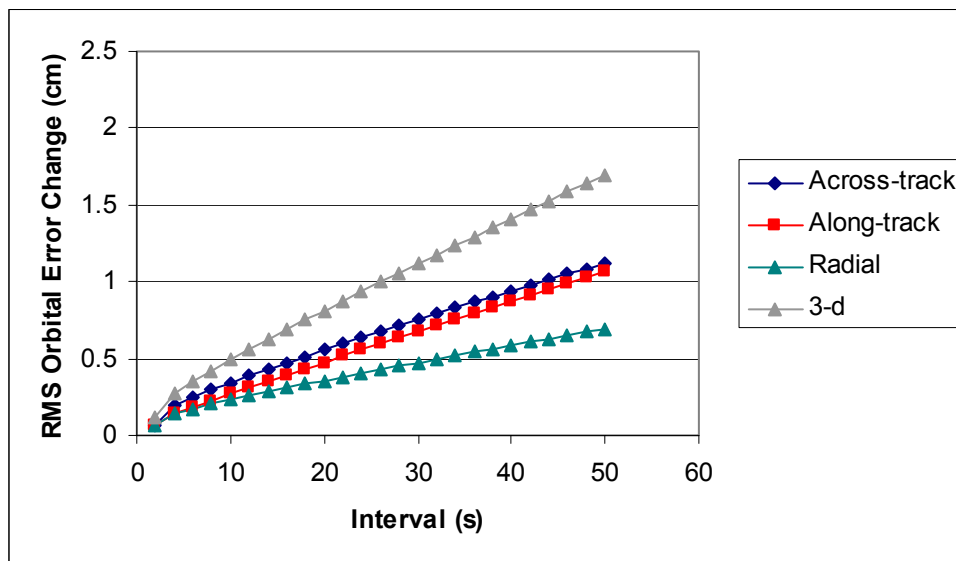
Figure 5.6: Average RMS orbital error change over time for each component for the marine data set
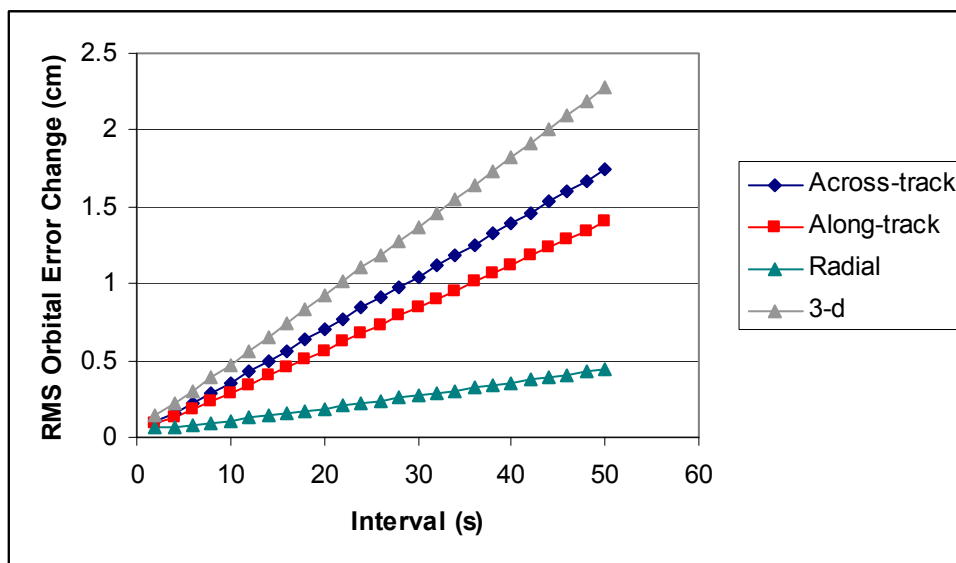


Figure 5.7 Average RMS orbital error change over time for each component for the airborne data set

**5.1.2 Autocorrelation of Orbital Error**

The average autocorrelation function for the orbital error in each component is given in Figures 5.8 and 5.9. Figure 5.8 shows the correlation over intervals of up to 50 seconds, while Figure 5.9 has intervals up to 30 minutes. The autocorrelation functions in this paper were computed using unbiased data sets, i.e. the means were removed. As well, the functions have been normalized so the peak is one for each function. This eliminates the effect that higher variances have on the results. Over time intervals of up to 50 seconds the orbital errors are highly correlated, at 0.978 for the across-track and in the along-track components, and 0.981 for the radial direction at 50 seconds. Over longer time intervals, the errors decorrelate further to 0.219 in the across-track component, 0.206 in along-track, and 0.232 in the radial direction after 30 minutes.
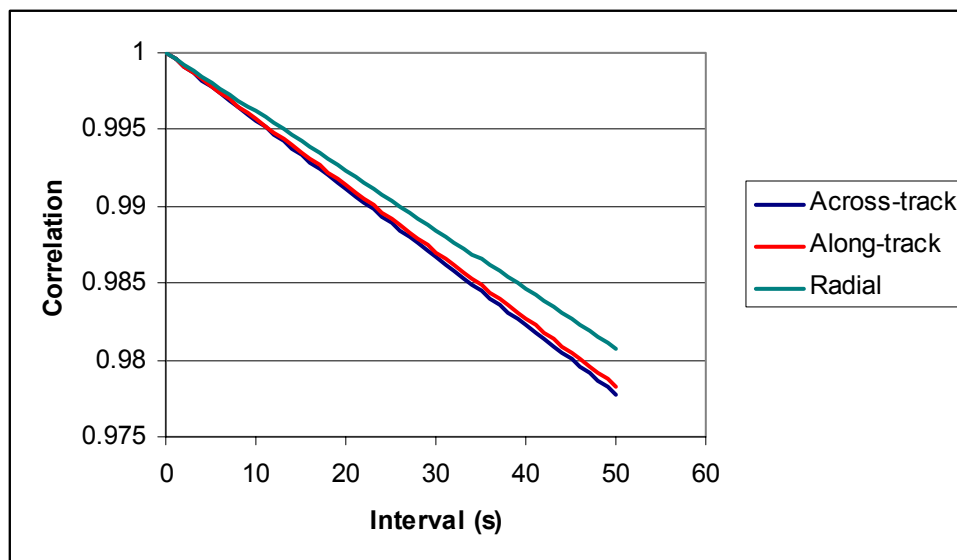
Figure 5.8: Average autocorrelation function for orbital error of all satellites for November 9 up to a 50 second interval
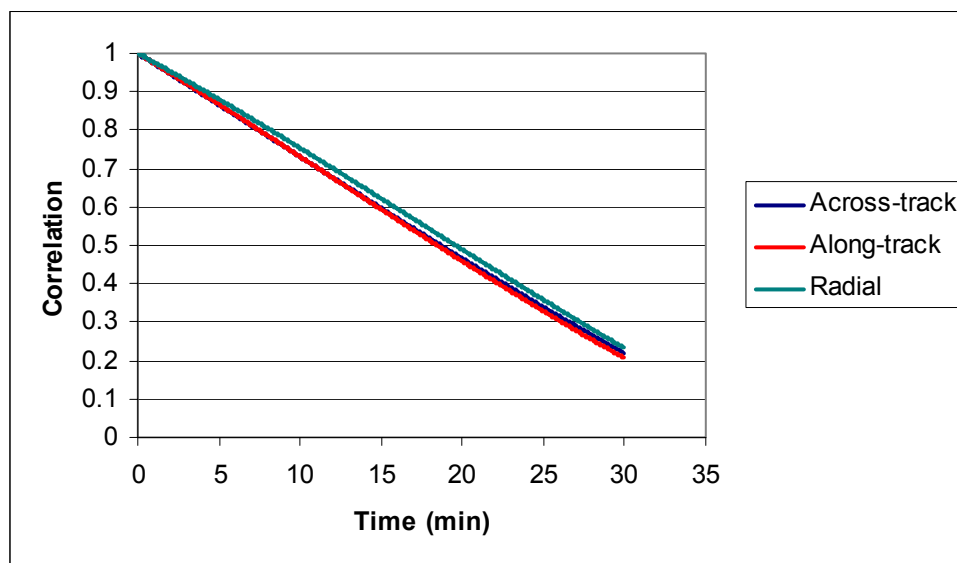
Figure 5.9: Average autocorrelation function for orbital error of all satellites for
November 9 up to a 30 second interval

## 5.1.3 Frequency Domain Analysis of Orbital Error

The power spectral density (PSD) gives the power as a function of frequency. In this case the power is very high at low frequencies. This concurs with the long-term trend present in the error. Figure 5.10 shows the PSD at less than 0.005 Hz, while Figure 5.11 gives it at 0.1-0.5 Hz. Due to the different variances of the time series for the three components, these results are not easily comparable just based on the PSD.

Figure 5.12 shows the percentage of the total power at frequencies below a given frequency, as computed using the method in Section 3.4. This allows much better comparison of the three directions. As is clear by the graph, the cumulative power is about the same at all frequencies for the across-track, along-track and radial components. The three lines in the plot are almost directly above each other. For each component, the power is highest at low frequencies, which is the cause of the trends in both the measurement and position domains. About 90% of the power is below 0.001 Hz for all components. It can be concluded from these results that the error behavior in the

frequency domain is about the same for each of the across-track, along-track, and radial directions.
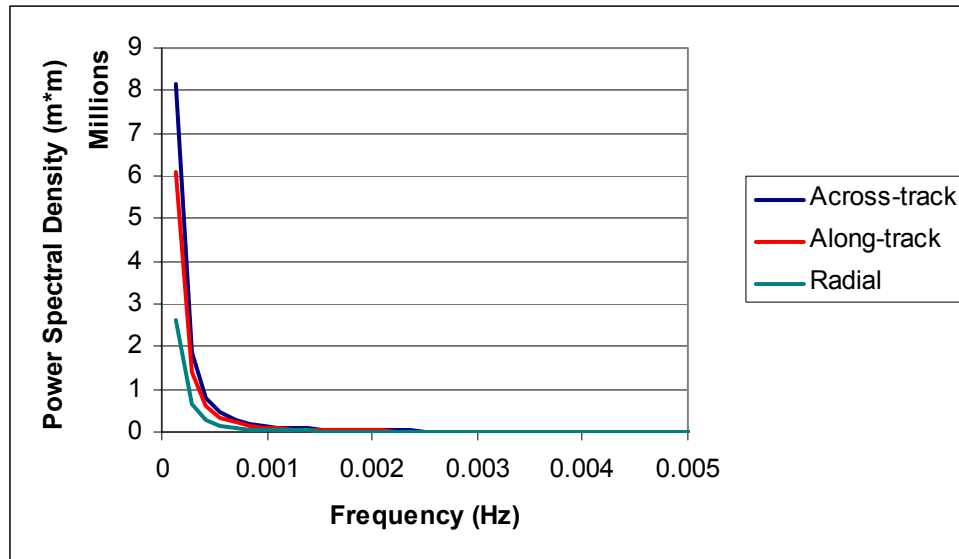


Figure 5.10 Average PSD of orbital errors on November 9 up to 0.005 Hz
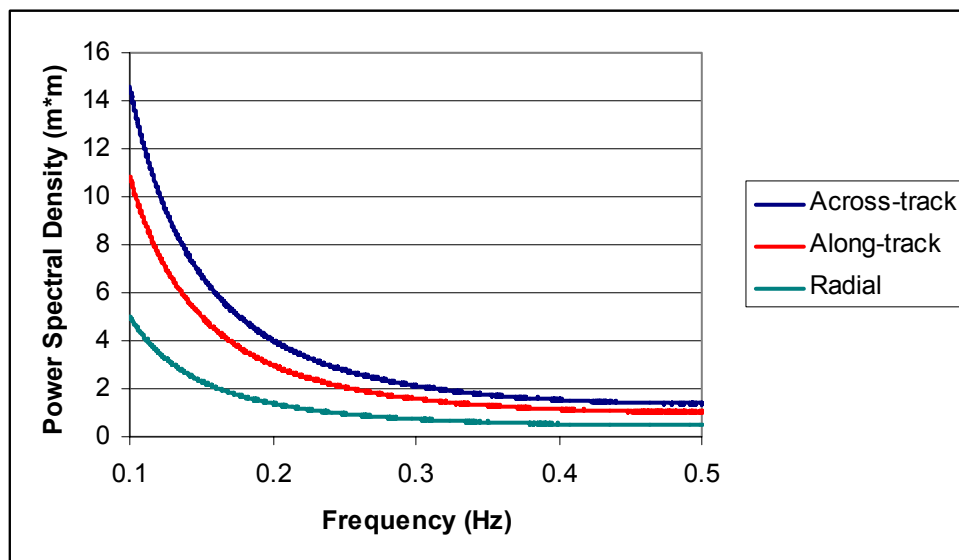


Figure 5.11 Average PSD of orbital errors on November 9 up to 0.5 Hz
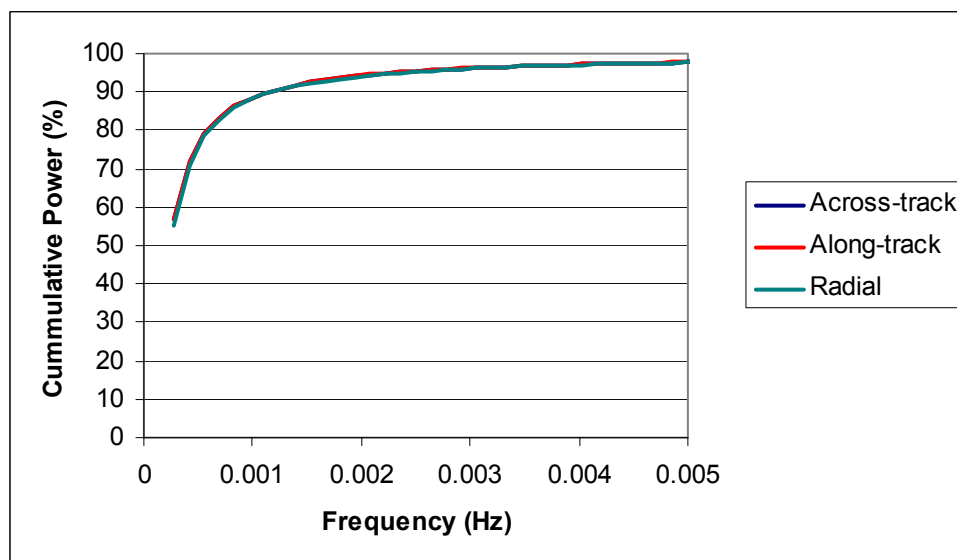
Figure 5.12: Average cumulative power as a function of frequency for orbital error of all satellites on November 9

## 5.2 Satellite Clock Error

The clocks on the GPS satellites are different depending on the block of the satellite. Block II and II A satellites have two cesium clocks and two rubidium clocks. Block II R satellites have three rubidium clocks, and also have the capability to do inter-satellite observations. Block II satellites were launched in 1989-1990, Block II A in 1990-1997, and Block II R in 1997-2001.

Errors due to the satellite clock error behave much differently depending on the oscillator. Figure 5.13 shows the satellite clock error on November 9 for one satellite from each block. Variations over several hours are evident in the Block II and II A satellites. However, SV 13, which is a Block II R satellite, does not show a significant trend that lasts more than 5 minutes. The plot shows the clock error scaled to metres.
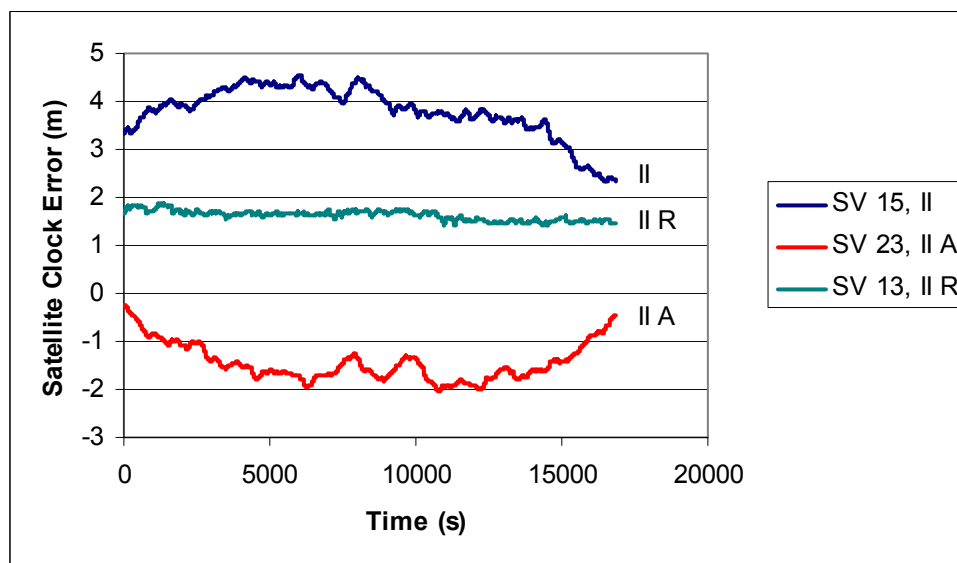
Figure 5.13: Absolute satellite clock error on November 9

## 5.2.1 Temporal Behavior of Satellite Clock Error

The satellite clock error change over time for each satellite on November 9 is given in Figure 5.14. The errors in the Block II R satellites are closely grouped, and vary between 2 and 3 cm over a 50 second interval. For Block II and II A satellites, the results have a much larger range, and are much less consistent. The Block II and II A satellites currently operating with the rubidium oscillators performed much better then those using cesium oscillators. This is the reason for the large spread in the results for these satellites. The averages of the RMS values for each block in Figure 5.14 are given in Figure 5.15. It is clear on this plot that the Block II R clocks perform the best, while the older Block II satellites have the poorest clock performance. As new satellites are launched it can be expected that the satellite clock stability will improve.
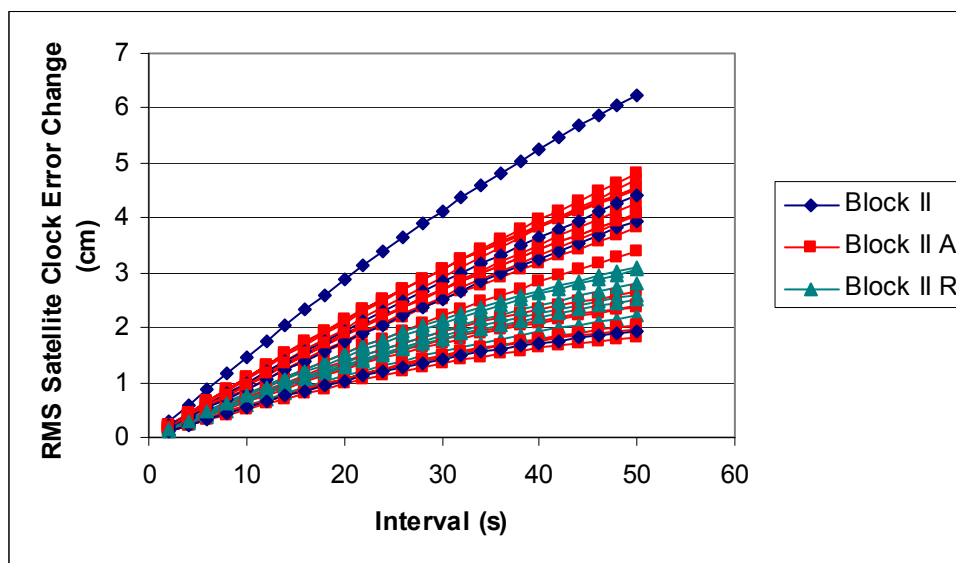
Figure 5.14: RMS satellite clock error changes over time for all satellites for November 9
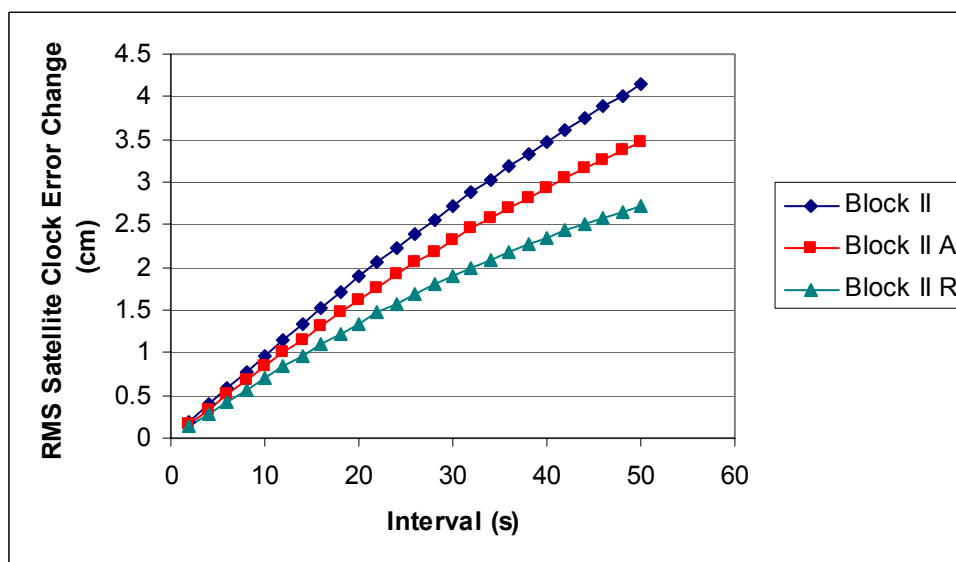


Figure 5.15: Average RMS satellite clock error changes over time for each Block of satellites for November 9

The average for all satellites of the RMS changes in the satellite clocks errors for intervals of up to 50 seconds is shown in Figures 5.16. The RMS change increases from 0.2 cm over 2 seconds, to 0.8 cm over 10 seconds, to 3.4 cm over 50 seconds. Based on

this plot, it seems probable that using precise clocks will have an impact in the position domain.
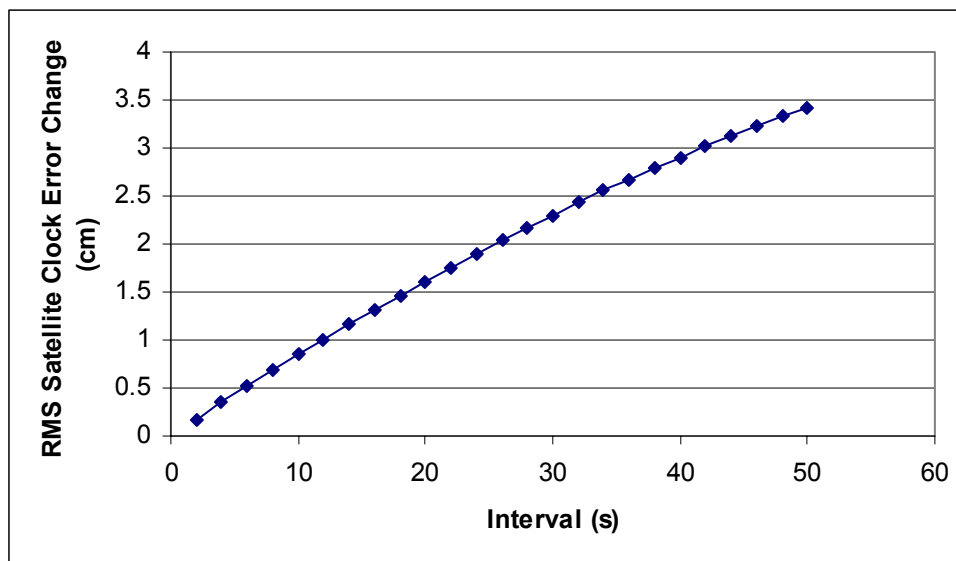


Figure 5.16: Average RMS satellite clock error change over time intervals of up to 50 seconds on November 9

The changes in the satellite clock error for each Block over intervals of up to 30 minutes are given in Figure 5.17. For Block II R satellites, the changes do not increase over intervals of more than 10 minutes. However, the other two Blocks show significant increases, and have much larger changes in the errors. The Block II satellites have the worst performance up to a 27 minute interval, at which point the Block II A satellite average is higher.

As with the orbital errors, the satellite clock errors behaved similarly from day-to-day. Figure 5.18 shows the average RMS change for each day. The range in average changes is 0.16-0.23 cm over 2 seconds, 0.63-0.83 over 10 seconds, and 3.20-3.60 cm over 50 seconds. This range is larger than with the orbital errors at shorter time intervals, but smaller over long time intervals. Over 2 seconds, the range is 44%, while it is about 12-13% for time intervals longer than 20 seconds.
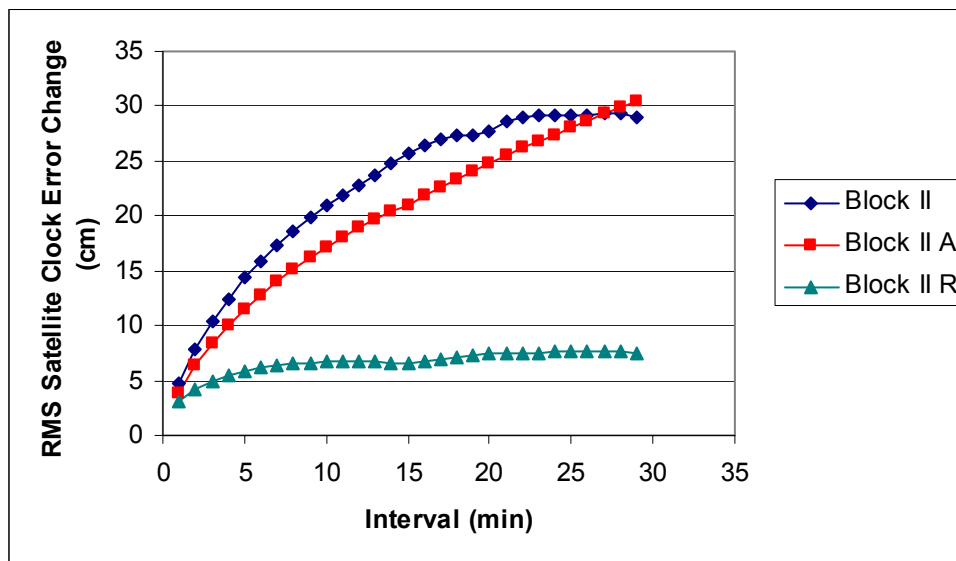
Figure 5.17: Average RMS satellite clock error change over time for November 9
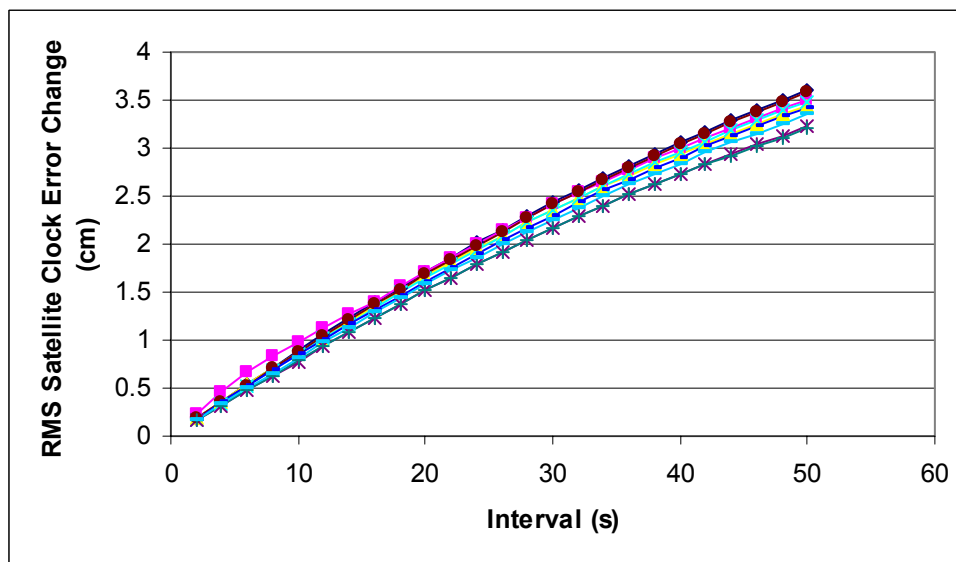


Figure 5.18 Average RMS of satellite clock error changes over time on November 2-10

The satellite clock error results for the marine and airborne data are shown in Figures 5.19 and 5.20, respectively. The results for the boat data are about the same as those for the land data. For the airborne results, only one of the eleven satellites in view was a Block II R satellite. The aircraft results were collected in June 2000, and at that time

only three of the six Block II R satellites available in November 2001 had been launched. This is the reason the results in Figure 5.20 are worse than those for the marine and land data.
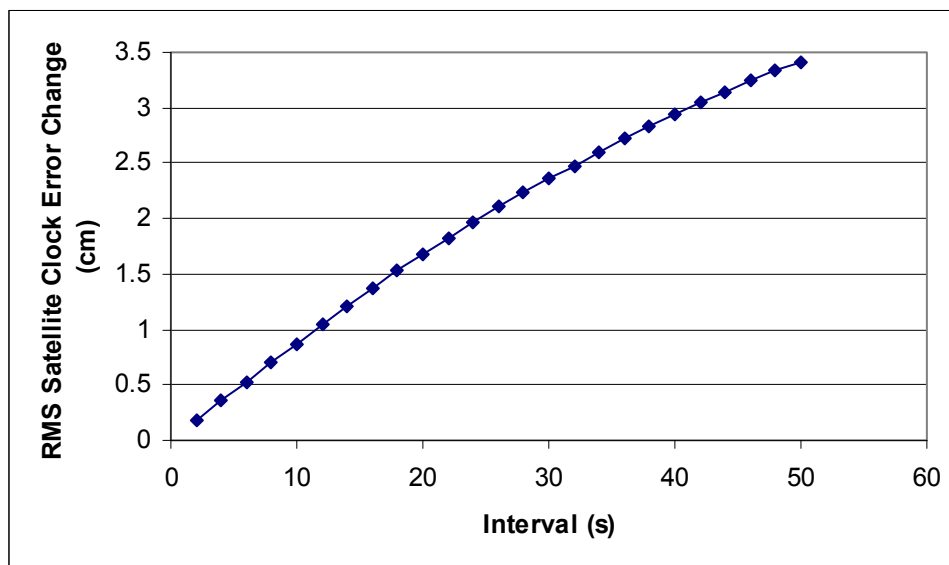


Figure 5.19: Average RMS satellite clock error change over time for marine data set
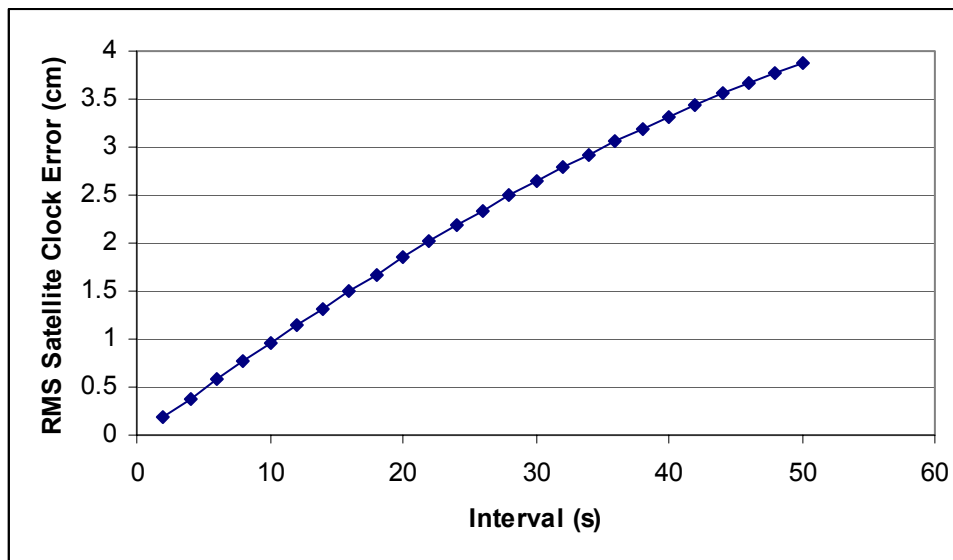


Figure 5.20: Average RMS satellite clock error change over time for airborne data set

**5.2.2 Autocorrelation of Satellite Clock Error**

Figures 5.21 and 5.22 shows the autocorrelation function for each Block of satellites on November 9. As with the orbital error correlation, Figure 5.21 has a maximum interval of 50 minutes and Figure 5.22 has a maximum of 30 minutes. These plots have been normalized to have a maximum of one. It is clear from the plots that the Block II R satellite clock errors decorrelate much faster than the other Blocks. However, if the plot is not normalized, the peaks for the Block II and II A satellites are on the order of several hundred due to the high variance, while they are less than 50 for the II R satellites. Block II and IIA satellites have a much higher trend in the clock error, which leads to the higher peak in the correlation before it is normalized. This means that the quality of the clock correction is much better in the Block II R satellites. Block II and II A clock errors have a correlation of 0.986 and 0.966, respectively, over 50 seconds, while the II R clocks errors have a correlation of 0.852. All three blocks decorrelate significantly over 30 minutes.

Since the errors of the oscillators in the Block II R satellites decorrelate so quickly, the effect of this error is not large on this application. The errors of the other two satellite Blocks have a more significant effect. Using precise clocks will have a larger effect on the relative position results over time if more of the satellites are Block II and II A satellites.
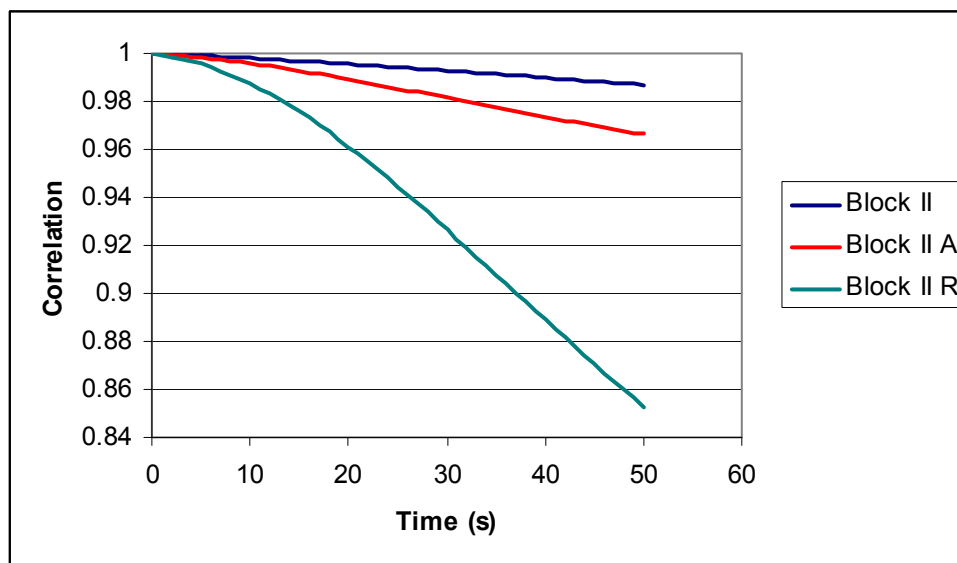
Figure 5.21: Autocorrelation function of the satellite clock error for each block of satellites for November 9 up to a 50 second interval
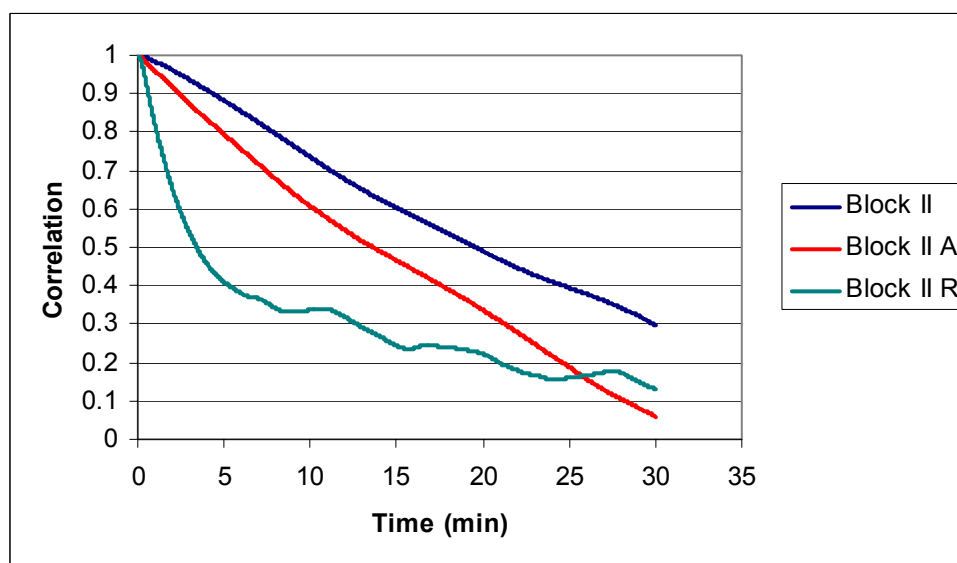


Figure 5.22: Autocorrelation function of the satellite clock error for each block of satellites for November 9 up to a 30 minute interval

**5.2.3 Frequency Domain Analysis of Satellite Clock Error**

The power spectral density is very different depending on the Block of the satellite. Block II and II A satellites have similar patterns. In this analysis, only four Block II satellites are available. Since there are few Block II satellites, the average of the PSD for these satellites is much more uncertain than for Block II A, which may explain why the power is higher at low frequencies for the II A satellites. The PSD of the satellite clock errors at two different frequency ranges are given in Figures 5.23 and 5.24. The large low frequency components of the Block II and II A satellites suggest the effect of using precise clocks will be largest over longer time intervals.

The cumulative power of the satellite clock error as a function of frequency is shown in Figure 5.25. Block II R satellites have a much smaller low frequency power component than the other two blocks. This is consistent with the results in Figure 5.13, which did not show a significant long-term trend. The power below 0.001 Hz is about 70% for the Block II R satellites, while it is about 95% for the other two blocks. The percentage of the power above 0.005 Hz is 0.63% for Block II, 1.05% for II A, and 4.75% for II R.
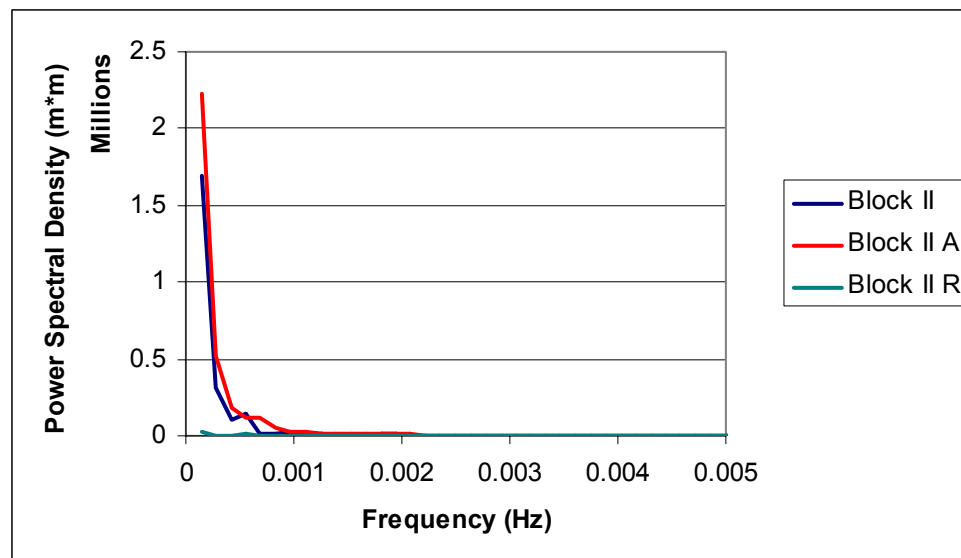
Figure 5.23: Average PSD of satellite clock error on November 9 up to 0.005 Hz
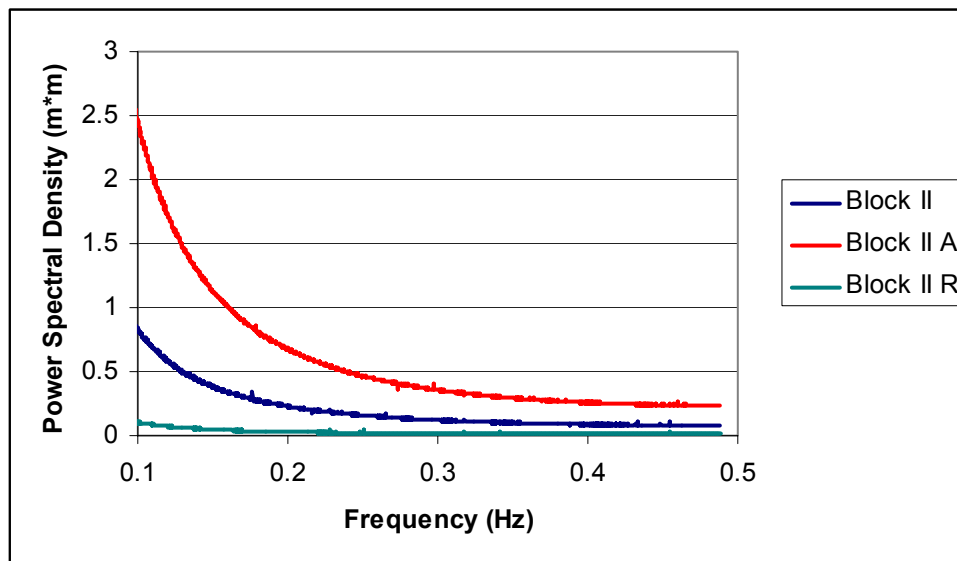
Figure 5.24: Average PSD of satellite clock error on November 9 up to 0.5 Hz
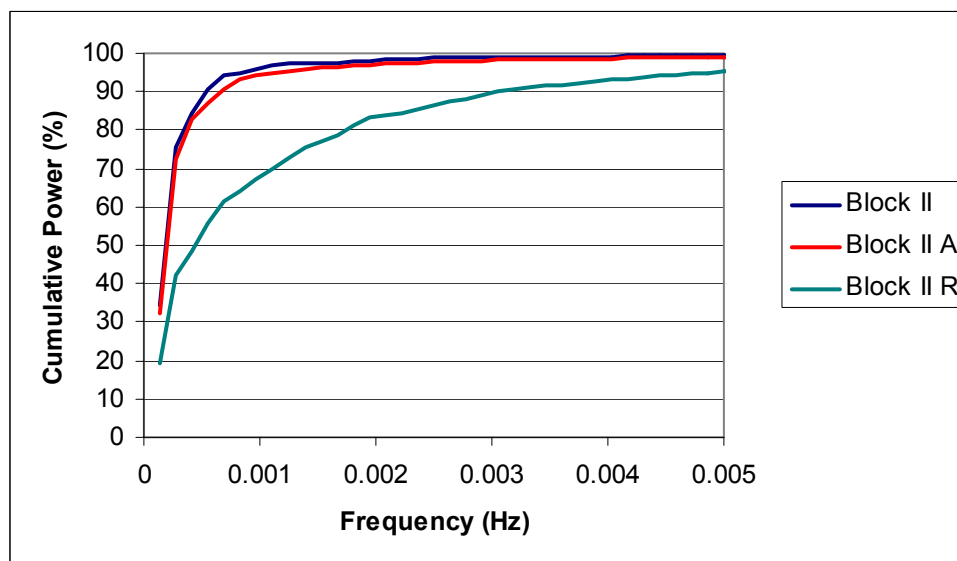


Figure 5.25: Average cumulative power as a function of frequency for satellite clock

error of all satellites on November

**5.3 Ionospheric Error**

Changes in the ionosphere varied substantially from day to day. In this analysis, the results from a typical day will be shown first. The results from November 6, a day with a severe ionospheric storm, are then presented for comparison purposes.

The local K index is a measure of geomagnetic substorm activity. This index has a range from 0 to a maximum of 9; with a larger K index corresponding to higher changes in ionospheric activity. A derivation of this index is given in Mayaud (1980). Figure 5.26 shows this index at the Meanook Geomagnetic Observatory from November 2 to 10, 2001, and there is a clear spike starting on November 5 and continuing to November 6. The Meanook station is 3.5° north and 0.6° east of the data collection point, so it can be assumed this storm had a large effect on the observed data. For the analysis of a typical day, results from November 9 will be given.
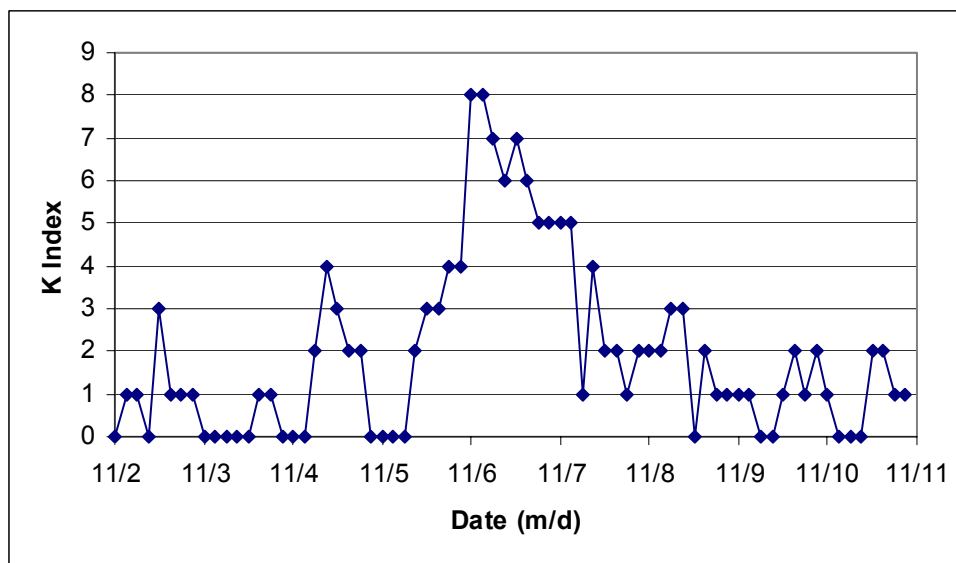


Figure 5.26: Local K index at Meanook Geomagnetic Observatory

The relative ionospheric error for several satellites on November 9 is given in Figure 5.27. This is not an absolute error, because the ambiguities of the carrier phase

measurements are unknown.  Figure 5.27 shows that the effect of the ionosphere is correlated with the time of day.  On this day, up to 09:00, the changes in errors are about 2 m for each satellite pass.  However, from this point on the errors increase significantly, with 10 to 15 m changes for many satellite passes.  Another cause of the discrepancies is the elevation angle of the satellite, which will be examined later.  The typical pattern of the ionospheric error over a satellite pass is that it decreases as the satellite is rising, and increases as the satellite is setting.
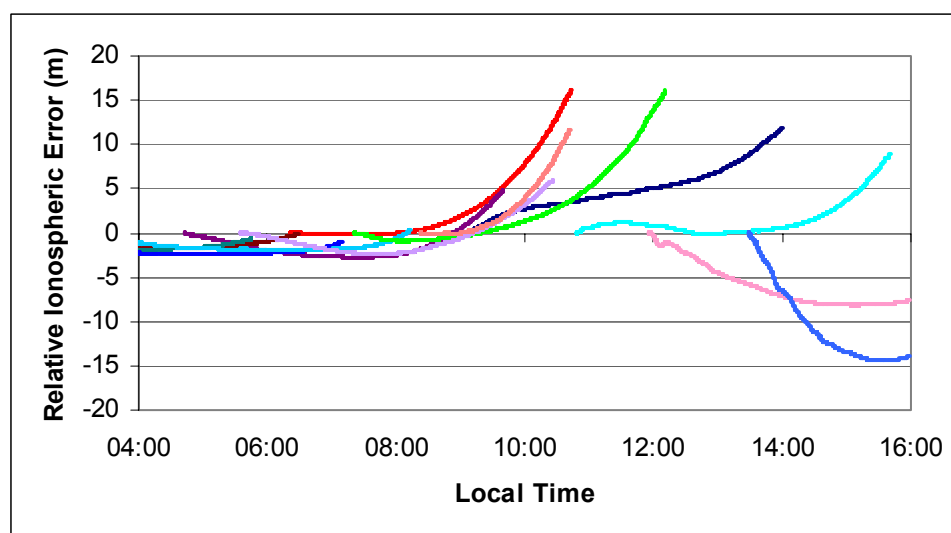


Figure 5.27 Changes in ionospheric error of several satellites on November 9

### 5.3.1 Temporal Behavior of Ionospheric Error

Figure 5.28 shows the ionospheric error temporal changes for each satellite on November 9.  The error increases with time in a linear manner similar to the orbital error.  This is due to the fact that there are significant trends, lasting several hours, in the ionospheric error on this day.  The RMS of the change in errors ranges from 0.6 to 1.2 cm over a 2 second interval on November 9.  This increases to a range of 0.9-2.7 cm over 10 seconds, and a range of 1.9-14.0 cm over 50 seconds.  This will cause changes in the errors of the computed positions, especially over long periods of time.
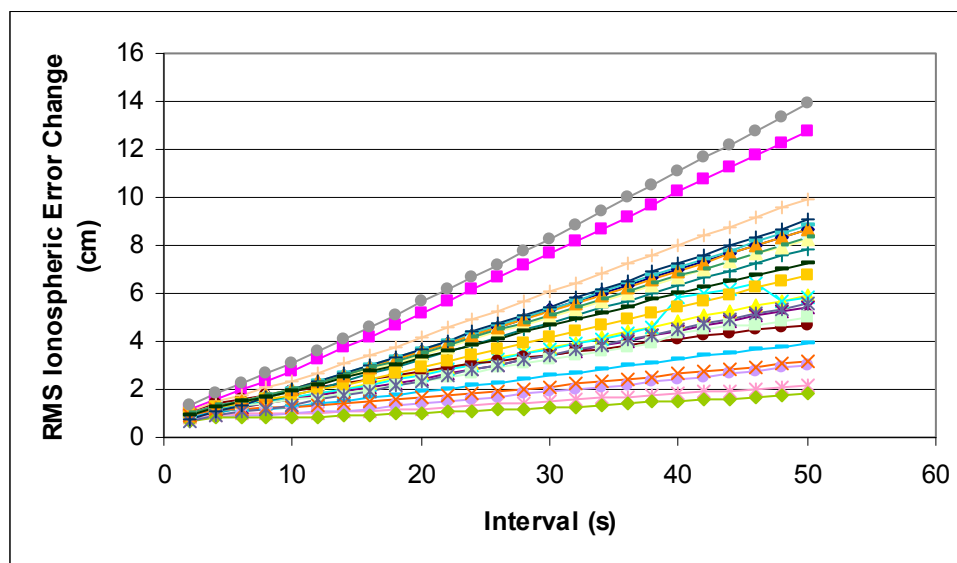
Figure 5.28: RMS ionospheric error changes over time for all satellites on November 9

The RMS ionospheric error change is significantly influenced by the elevation angle. As is expected, Figure 5.29 shows that the error change increases as the elevation angle decreases. This is consistent with what was expected, since the lower elevation signals travel through more of the ionosphere to reach the antenna. This means the highest elevation mask possible should be used to get the best possible position stability. However, this must be balanced against the effect of a larger PDOP on the positions.

The average RMS change in the ionospheric errors on a typical day is shown in Figures 5.30 and 5.31 for intervals of up to 50 seconds and 30 minutes, respectively. The RMS increases at a linear rate up to 15 minutes, at which point the rate of increase starts to decrease. The RMS continues to increase up to 30 minutes, which is reasonable since trends of more than 30 minutes are present in the errors. The RMS over a 30 minute interval is much larger than both the orbital and satellite clock errors. Due to the increasing nature of the change in the error, the ionosphere will negatively affect the position stability. Results in Skone (1998) show the variance increases up to about a 35 minute interval, after which the variance does not have a discernable trend. The

magnitude of the variance over 30 minutes in Skone (1998) is 8 TEC units on an active ionospheric day, which corresponds to 128 cm on L1.
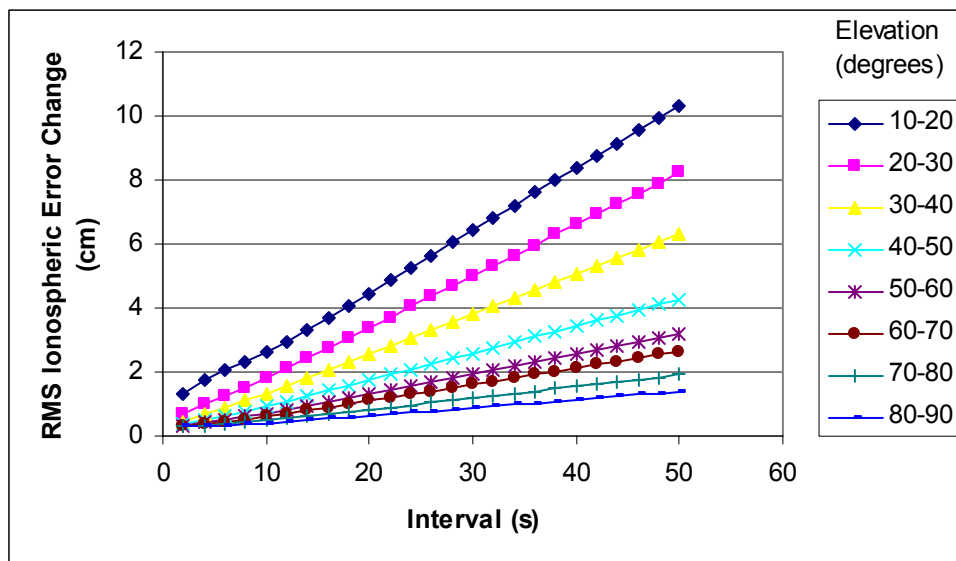


Figure 5.29: Average RMS ionospheric error changes over time for each elevation angle band on November 9
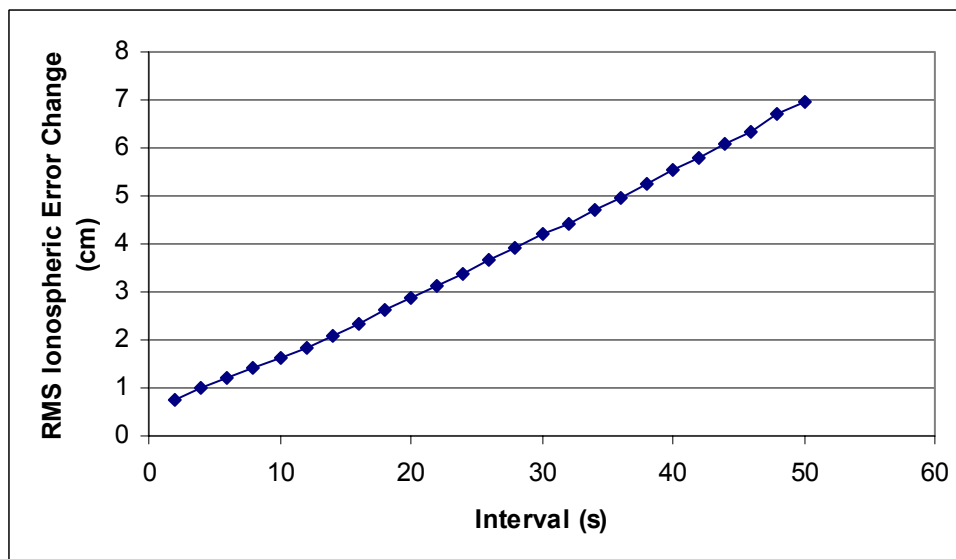


Figure 5.30: Average RMS ionospheric error changes over time intervals of up to 50 seconds for all satellites on November 9
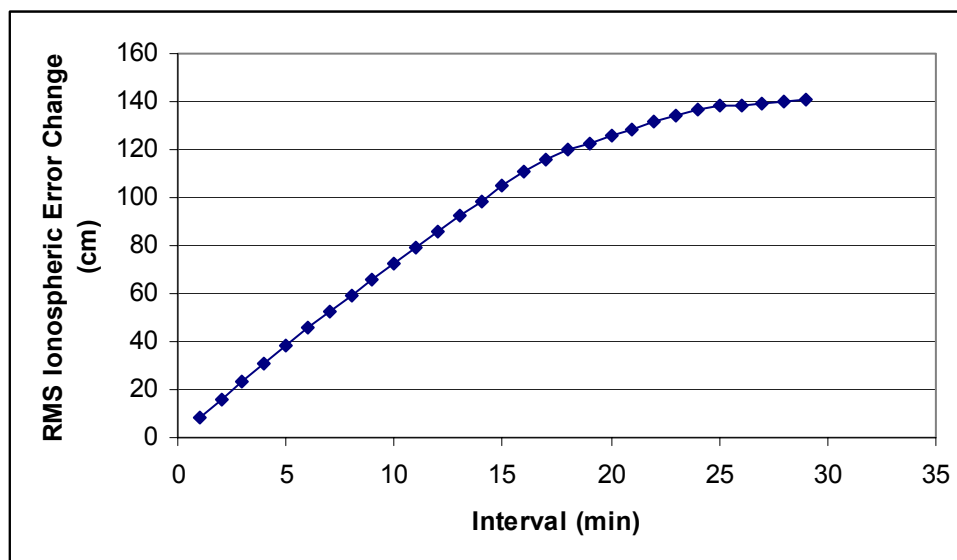
Figure 5.31: Average RMS ionospheric error changes over time intervals of up to 30 minutes for all satellites on November 9

Figure 5.32 shows the average RMS ionospheric error change for each day from November 2 to 10. The large changes in the graph are most likely due to the ionospheric storm on November 5-6 (NOAA, 2001). The error changes are 3.6 to 4.7 times larger on November 6 than on November 9 over intervals of between 4 and 50 seconds. The impact of using dual frequency data to apply an ionospheric correction will be much larger on the two days of the storm event, as compared to the other days.

The changes in the ionosphere errors for the individual satellites are much larger under the storm conditions. Figure 5.33 shows the changes in the ionospheric over time for each satellite on November 6. The change in the error reaches a maximum of 62 cm over 50 seconds. In Figure 5.28 the changes over 50 seconds ranged from 2-14 cm.
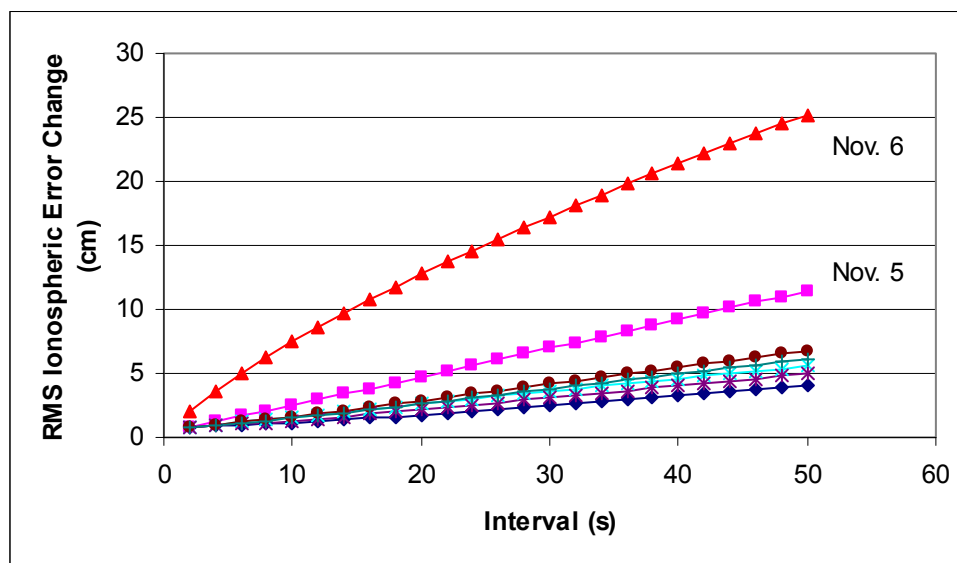
Figure 5.32: Average RMS ionospheric error changes over time on each day
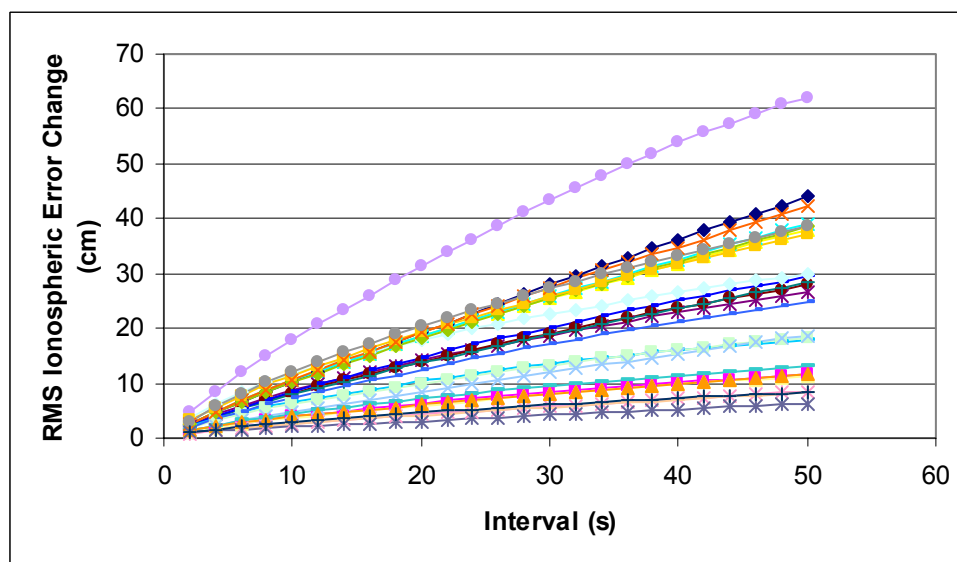


Figure 5.33: RMS ionospheric error changes over time for all satellites on November 6

Figures 5.34 and 5.35 show the changes in the ionospheric errors over time for the marine and airborne data sets. Both graphs show higher ionospheric errors than all but the two severe ionospheric days in the static data set. The reason for this discrepancy is primarily the time of day the data was collected. The results in Figure 5.27 showed that the hours

around 12:00 local time have larger ionospheric changes than earlier in the day. The marine data was collected from 13:20-15:10, while the airborne data was collected from 09:30-11:20. Over a 2 second time interval, the RMS change in the ionospheric error is 0.8 cm for each of the static, marine, and airborne data. Over 50 seconds the airborne data values are 8.7 cm, as compared to 7.9 cm for the marine data, and 7.0 cm for the static data on a typical day.
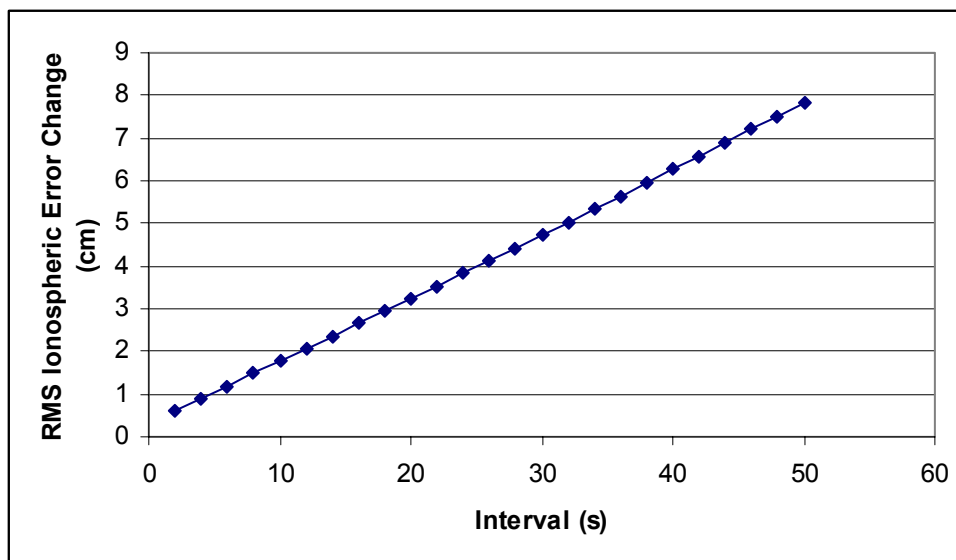


Figure 5.34: Average RMS ionospheric error changes over time for all satellites in view for marine data
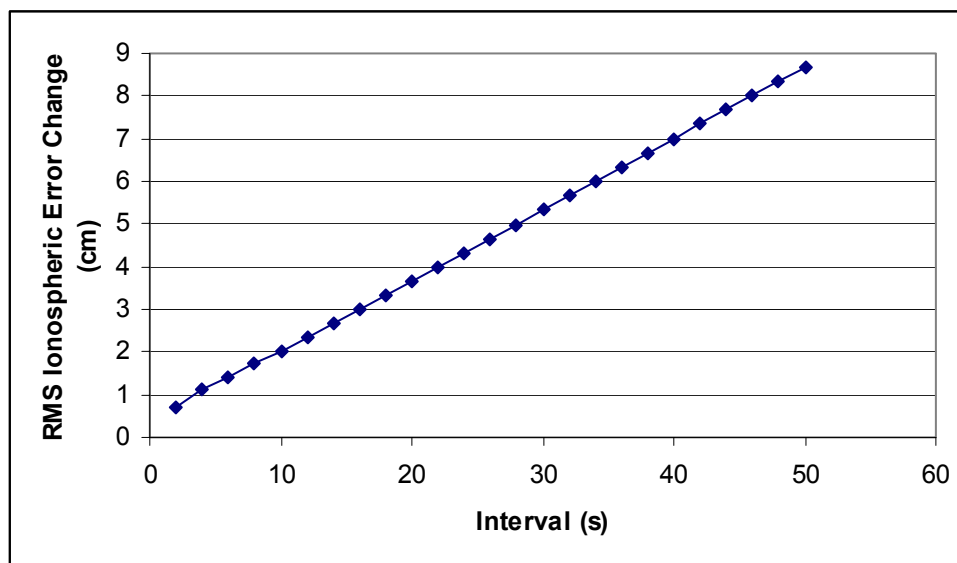
Figure 5.35: Average RMS ionospheric error changes over time for all satellites in view for airborne data

## 5.3.2 Autocorrelation of Ionospheric Error

The autocorrelation functions for one typical satellite under normal and high ionospheric conditions over intervals of up to 50 seconds and 30 minutes are given in Figures 5.36 and 5.37, respectively. The errors become less correlated over time, with the error on the severe day decorrelating much faster. This is consistent with the results in Skone (1998). Over 50 seconds, there is very little decorrelation in each case. However, over 30 minutes the ionospheric error decorrelates almost entirely on the severe ionosphere day.
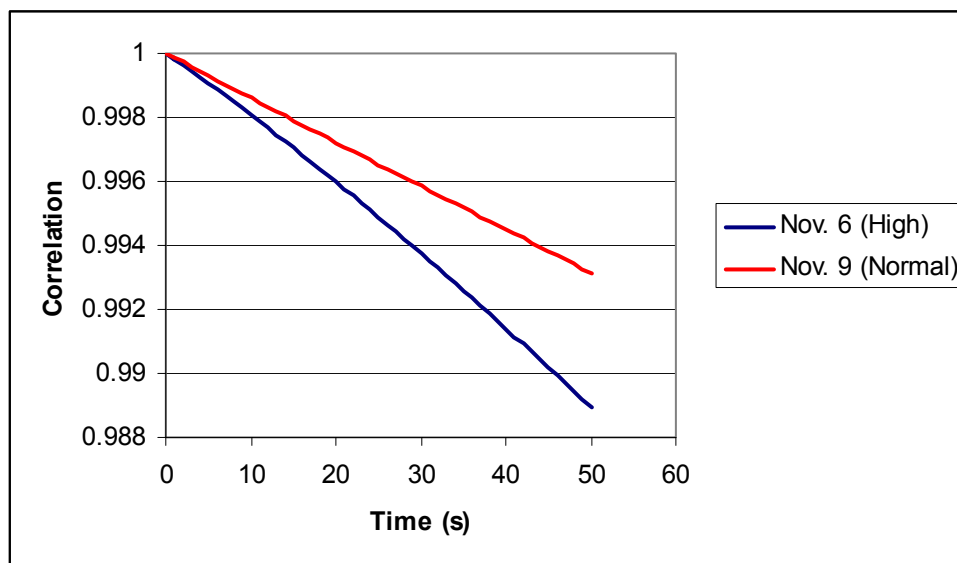
Figure 5.36: Autocorrelation function for ionospheric error of SV 10 on November 6 (high) and 9 (normal) up to a 50 second interval
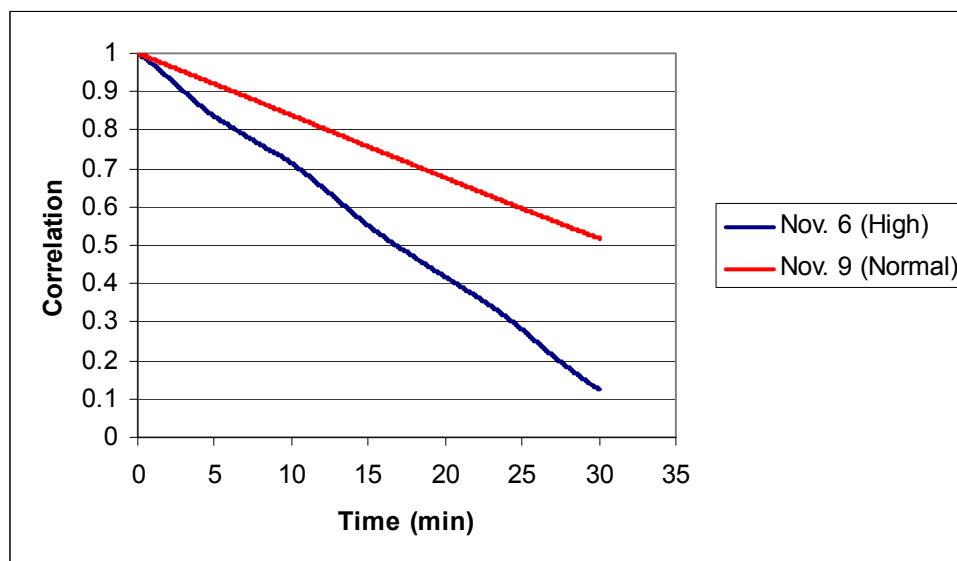


Figure 5.37: Autocorrelation function for ionospheric error of SV 10 on November 6 (high) and 9 (normal) up to a 30 minute interval

### 5.3.3 Frequency Domain Analysis of the Ionospheric Error

A frequency domain analysis of a moderate and extreme ionospheric day shows significant differences.  This analysis is done with the same satellite as was used in Section 5.3.2.  At low frequencies the results in Figure 5.38 do not show a smooth line for the high ionosphere day.  The PSD increases much higher on four separate occasions.  This did not occur for the moderate ionosphere day, or on the PSD plots for the orbital and satellite clock errors.  This indicates that the higher frequency part of the error is much more significant under extreme ionospheric conditions.  The results for higher frequencies given in Figure 5.39 show a much noisier plot than for the orbital and satellite clock errors.  This is due to the fact that real measurements are used for each data point, rather than interpolated values.  The computed ionospheric results are also influenced by other carrier phase errors, such as noise and multipath.

The lines in Figure 5.40 show there is less power at the high frequencies during high ionospheric conditions.  The error varies much faster, leading to more power in the high frequency components.  However, this is neutralized due to the high magnitudes of the changes over longer time periods.
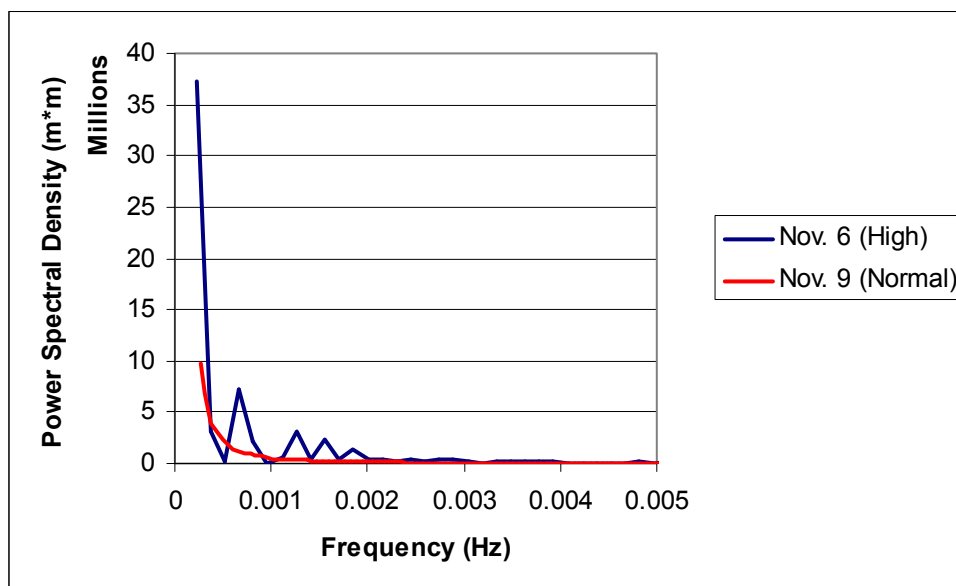
Figure 5.38: PSD of ionospheric error of SV 10 on November 6 (high) and 9 (normal) up to 0.005 Hz
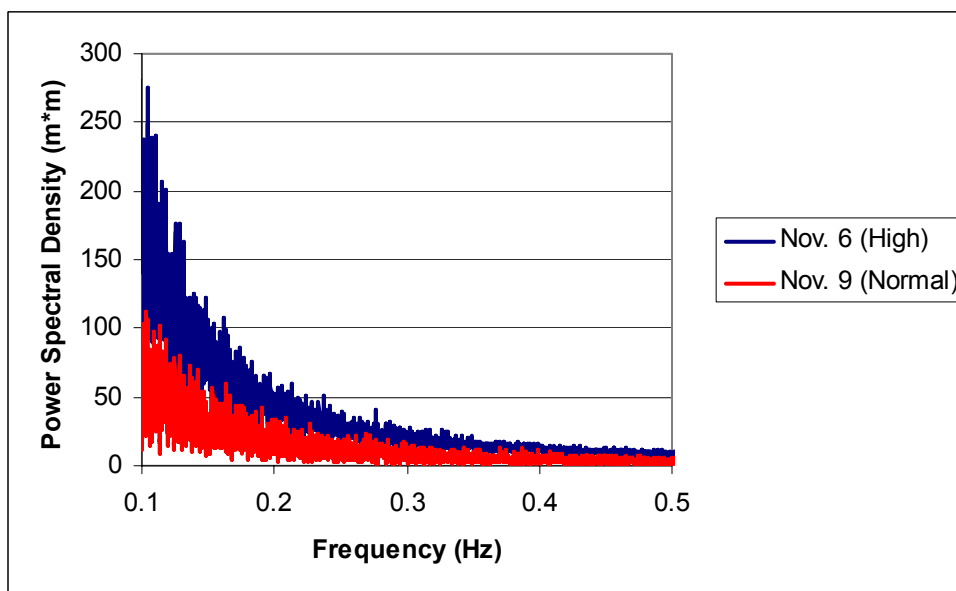


Figure 5.39: PSD of ionospheric error of SV 10 on November 6 (high) and 9 (normal) up to 0.5 Hz
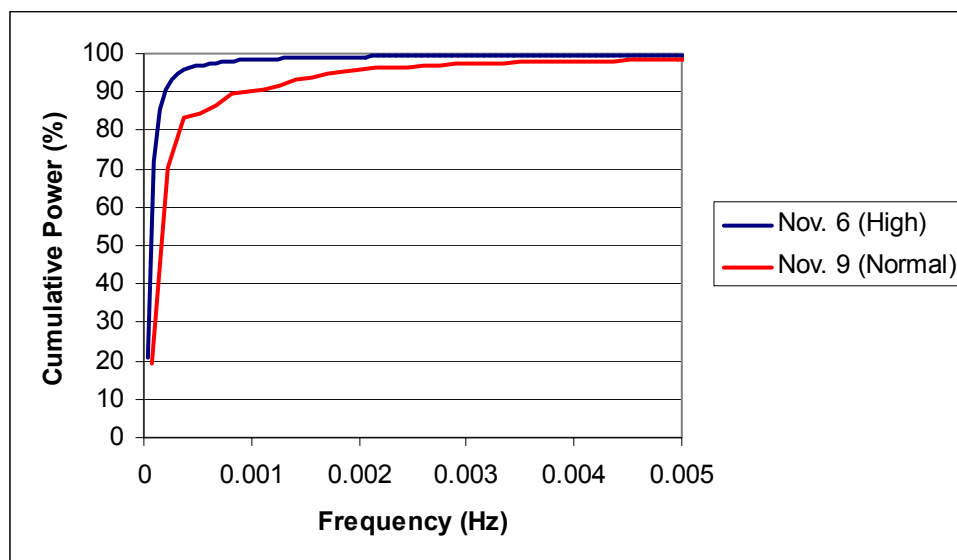
Figure 5.40: Average cumulative power as a function of frequency for ionospheric error
of SV 10 on November 6 (high) and 9 (normal)

## 5.4 Remaining Errors

If the tropospheric correction is not applied, the magnitude of the tropospheric effect, in
addition to the remaining errors, will be large. The remaining errors include multipath,
noise, and higher order ionospheric effects. The tropospheric error is heavily dependent
on the elevation angle. As is shown in Figure 5.41, the errors decrease at higher
elevations. The change in the remaining errors varies between 4-12 m over a satellite
pass in the plot. These errors will have a significant effect on the computed GPS
positions, which is why typically a correction is applied in GPS processing to account for
the troposphere. As with the ionospheric error, the characteristic pattern is that the
remaining errors decrease as the satellite rises, and increase as the satellite sets.
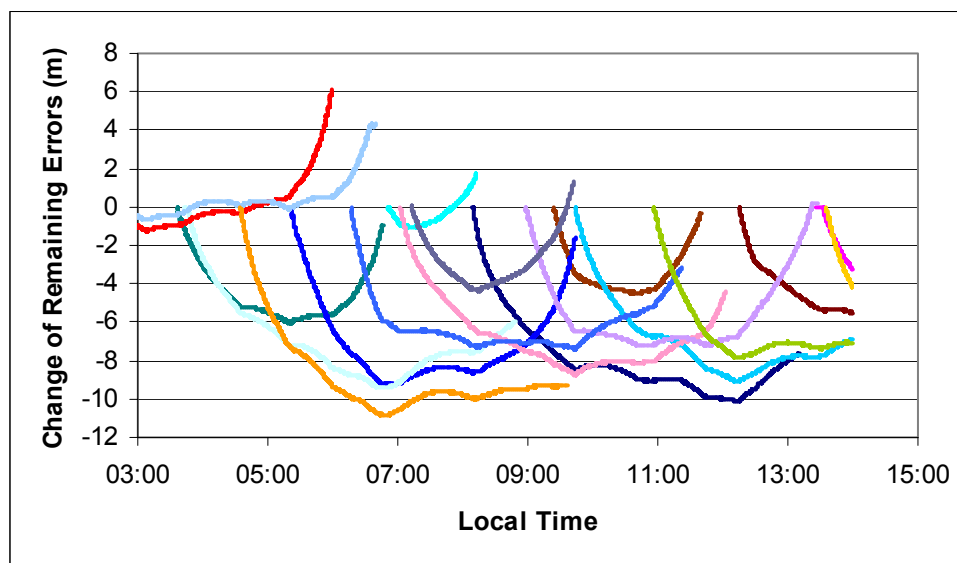
Figure 5.41: Change in remaining errors before applying tropospheric correction for several satellites on November 9

The error behavior is much different if a tropospheric correction is applied, as only the residual error remains. The remaining errors in this case are given in Figure 5.42. The change in the remaining errors over a satellite pass typically ranges from 1-2 m, which is far lower than the 10 m changes evident for some satellites when the tropospheric correction is not applied. The errors are increasing at higher elevation angles, suggesting the correction overcompensated for the tropospheric error.

When the tropospheric correction is applied it takes into account the temperature, humidity, and pressure of the atmosphere. Due to the fact that the results are processed over an entire day while the atmosphere changes there will be some inaccuracy in these quantities. Often in GPS processing a standard atmosphere is used. Due to the cold weather and low humidity in Calgary in November, the tropospheric delay is overestimated by the standard atmospheric parameters.
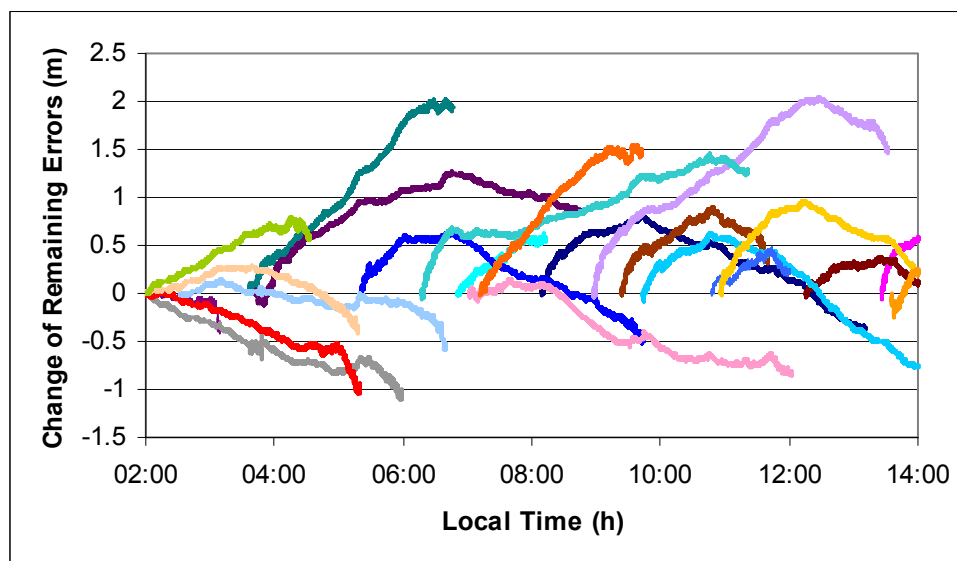
Figure 5.42: Change of remaining errors after applying tropospheric correction for several satellites on November 9

## 5.4.1 Temporal Behavior of Remaining Errors Before Tropospheric Correction

The change in the remaining errors is shown in Figure 5.43. The majority of the lines on this plot show a linear increase in the RMS over time. This suggests that changes in the tropospheric error are the dominant effects, since the multipath and noise errors do not have the trends of more than 50 seconds shown in this graph.

As would be expected, the changes in the remaining errors are largest for lower elevation bands. Figure 5.44 shows the changes are 2-3 cm over 50 seconds with elevations higher than 40°. Over lower elevations the changes are much higher. This is due to all of the remaining errors, such as the tropospheric error, multipath and noise, which have a larger effect when the satellite is closer to the horizon.
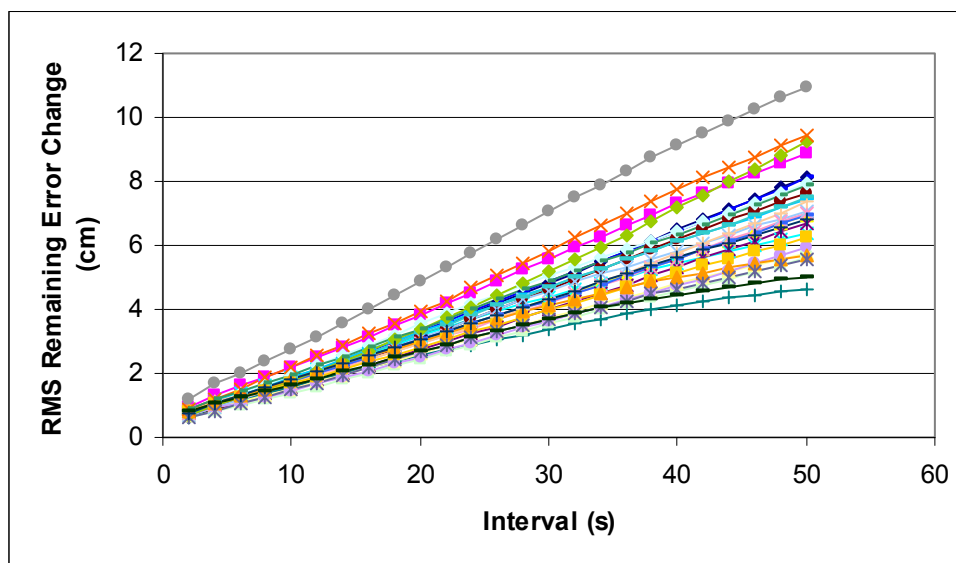
Figure 5.43: RMS of remaining error changes over time for all satellites for November 9
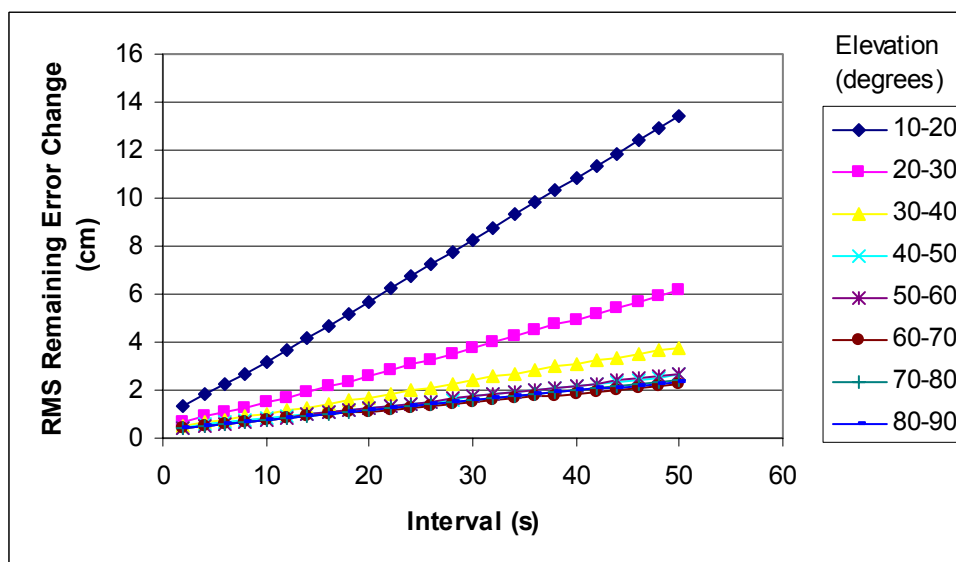


Figure 5.44: RMS of remaining error changes over time for all satellites for several elevation bands on November 9

There are minor day-to-day differences in the remaining errors. The changes are most obvious over the shortest time periods, as shown in Figure 5.45. On the day with the extreme ionospheric conditions represented by Figure 5.26, the remaining errors are 75%

larger over 2 seconds. This may be due to increased noise because of the ionospheric conditions. Other factors include the changes in higher-order effects of the ionospheric error. However, over the longer time intervals in Figure 5.45 the temporal behavior of the remaining errors in similar, with a range of 7.0-7.7 cm over 50 seconds.
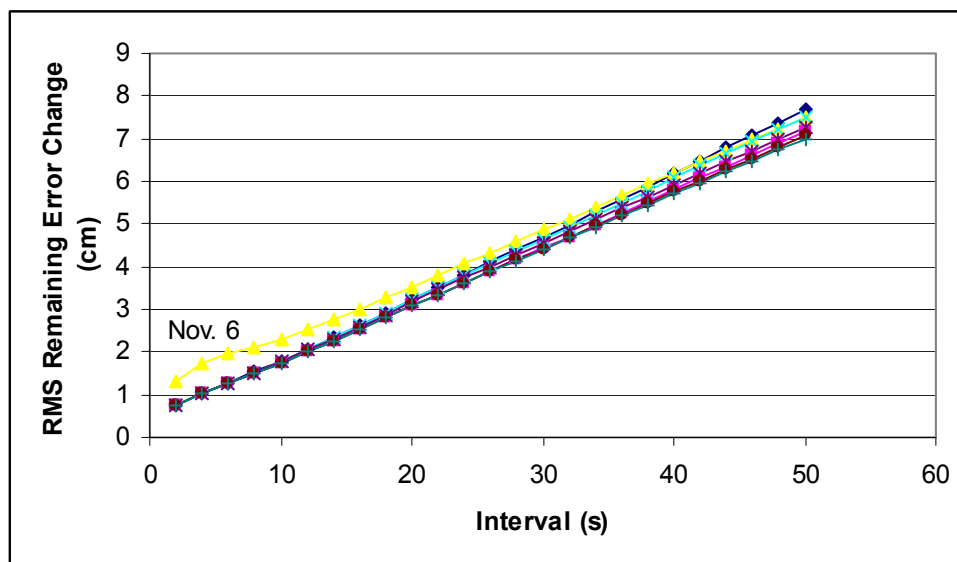


Figure 5.45: Average RMS of remaining error changes over time for all satellites for each day on November 2-10

## 5.4.2 Temporal Behavior of Remaining Errors After Tropospheric Correction

As shown in Figure 5.46, the temporal changes in the remaining errors are significantly reduced when a tropospheric correction is applied. The correction models the troposphere, but does not entirely remove the effects. The inaccuracy in the model, specifically with respect to the wet delay results in some residual errors. The noise and multipath are also present in the remaining errors. The results without the correction applied have an RMS range of 4.5-11.0 cm over a 50 second interval, while the corresponding amount is 1.2-2.2 cm with the correction applied. The slope in the lines is steepest between a 2-4 second interval, suggesting that the changes in multipath have a large effect over this range. However, the lines are much flatter for the rest of the graph.
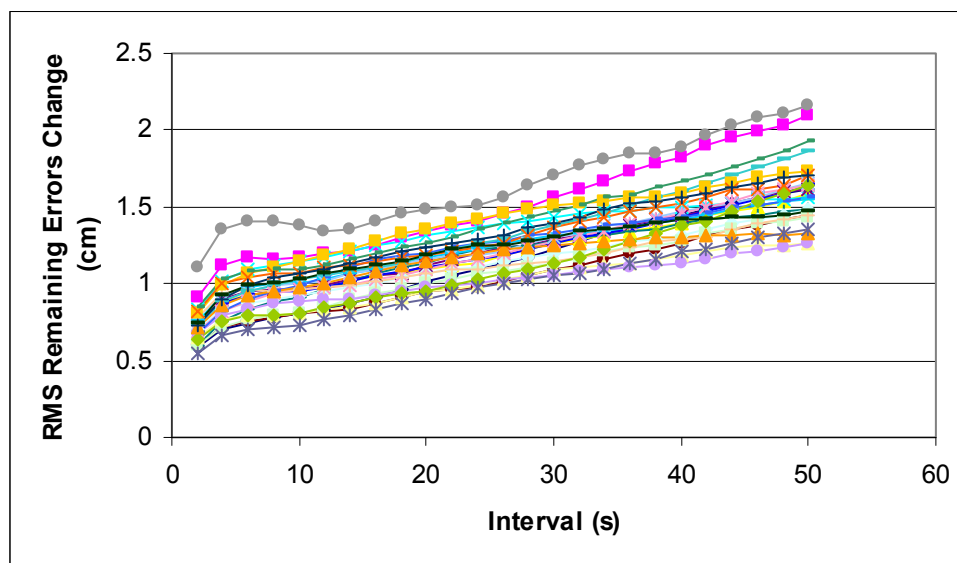
Figure 5.46: RMS of remaining error changes over time for all satellites for November 9

The magnitude of the change in the remaining GPS errors is still dependent on the elevation angle after a tropospheric correction is applied. Figure 5.47 shows that the remaining errors behave similarly above a 30° elevation angle. Above 30°, the RMS of the change in errors range from 0.4 cm over 2 seconds to 1.2 cm over 50 seconds. In the 10° to 20° elevation band the change is 1.2 cm over 2 seconds, and 2.6 cm over 50 seconds.

There are substantial changes from day-to-day for the remaining errors once the tropospheric error has been removed. On the day with severe ionosphere effects the changes in the remaining errors are far larger than the other days, as shown in Figure 5.48. The errors are much larger over all time intervals, which is different than when no tropospheric correction was applied. This is due to the fact that the tropospheric error is the major error in Figure 5.45, while it is not as large a factor in Figure 5.48. Errors due to multipath and noise are a larger factor, although the magnitude of the phase multipath is not dependent on the ionospheric conditions.
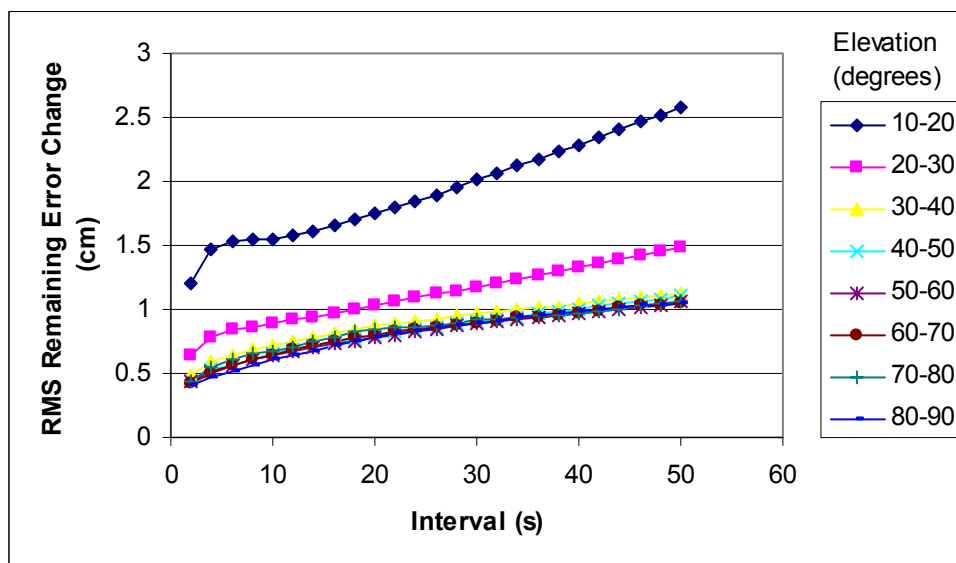
Figure 5.47: RMS of remaining error changes over time for all satellites for several elevation bands on November 9
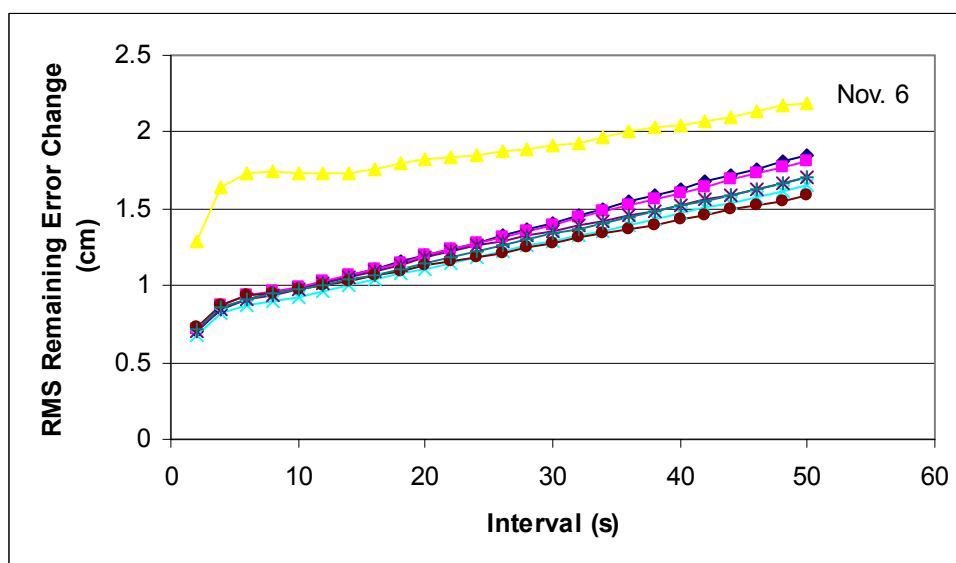


Figure 5.48: Average RMS of remaining error changes over time for all satellites for each day on November 2-10

It was mentioned earlier that the standard atmosphere overestimated the tropospheric effects. Figure 5.49 shows the RMS of the changes in the remaining error with both an

estimated and standard atmosphere. The estimated atmosphere has a much lower temperature and humidity than the standard values, due to the weather in Calgary in November. The results show an improvement with estimated atmospheric parameters over the longer time intervals. The improvement increased from 0% over 2 seconds to a maximum of 11% over 50 seconds. For this reason, an estimated atmosphere, rather than a standard atmosphere is better in this case, and will be used in computing the position results.
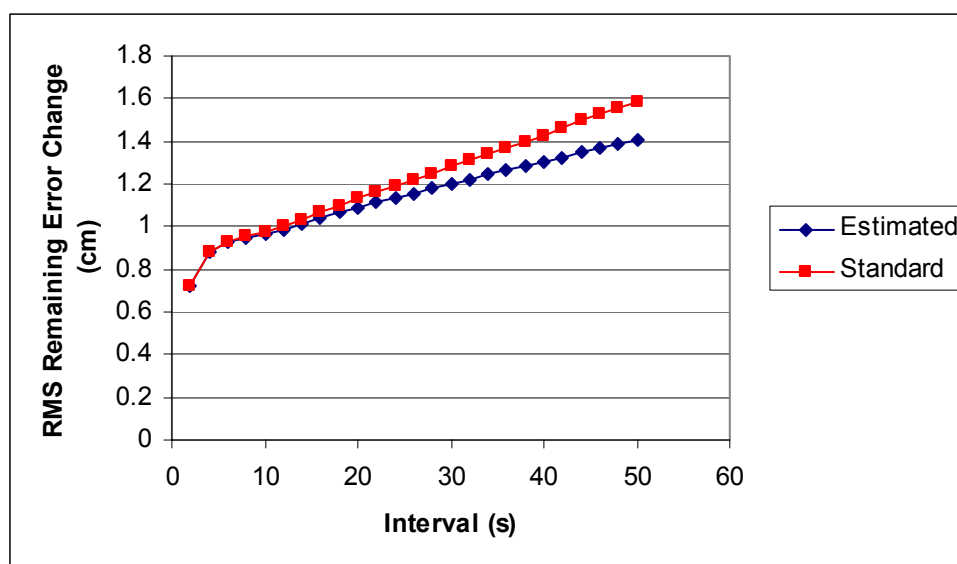


Figure 5.49 Comparison of changes in remaining errors over time when applying tropospheric correction with estimated and standard atmospheric parameters

The remaining errors for the marine and airborne data sets are shown in Figures 5.50 and 5.51. It should be noted that the positions used to compute the receiver clock error are DGPS positions, rather than known positions. This will increase the change in the remaining errors, due to the inaccuracy in the true range, and the inaccuracy in the computed receiver clock error. The marine and airborne results are similar to November 9 results, although they are larger in magnitude. In addition to the reasons mentioned earlier, the increase is due to the elevation of the satellites. It has been shown that the change in the remaining errors decreases as the elevation angle increases, and a larger

percentage of the satellites are at low elevations for these two data sets than for the land data. This will also lead to degraded results in the position domain.
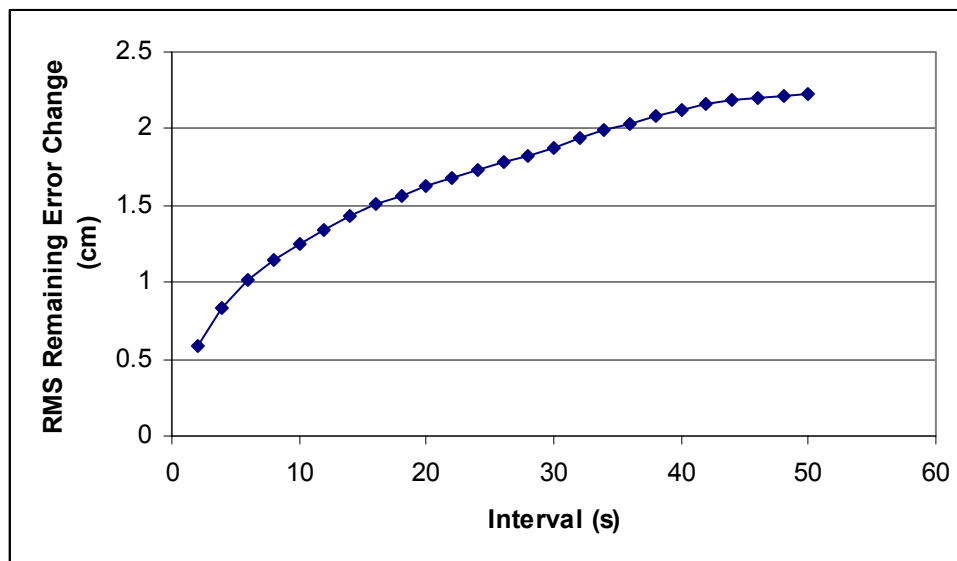


Figure 5.50: Average RMS of remaining error changes over time for all satellites after applying tropospheric correction for marine data set
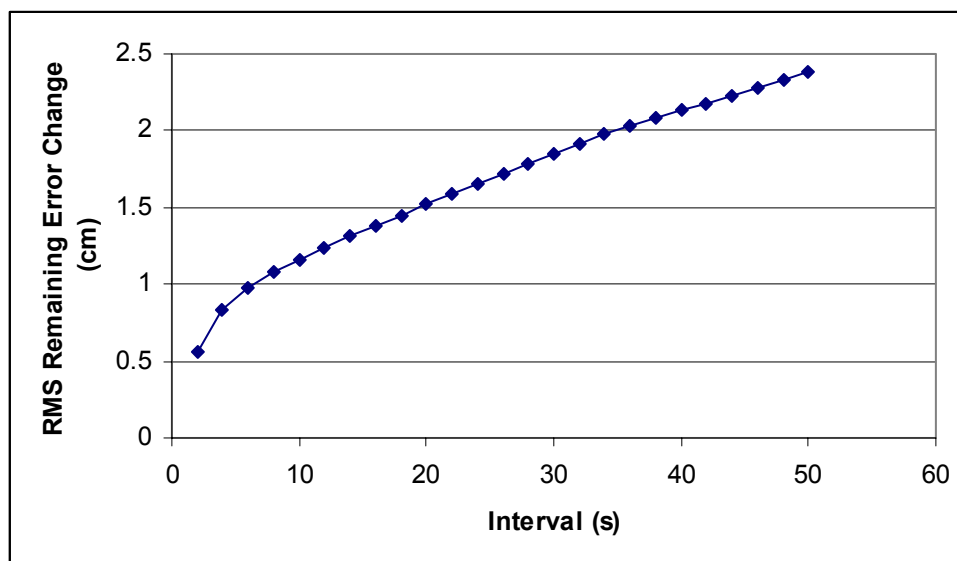


Figure 5.51: Average RMS of remaining error changes over time for all satellites after applying tropospheric correction for marine data set

### 5.4.3 Comparison of Temporal Behavior of Remaining Errors

There are significant differences in the changes in the remaining errors over time depending on whether or not a tropospheric correction is used. Figure 5.52 shows the difference between the changes, based on the elevation band. It was computed by subtracting the results in Figure 5.47 from those in Figure 5.44. The results show that over intervals less than 10 seconds for elevations over 30° there is little change. The effects due to multipath and noise are larger than the impact of the correction. However, for lower satellites, and longer time intervals there are significant changes in the remaining errors. The increase is linear for each satellite, suggesting that trends much longer than 50 seconds are the dominant part of the remaining errors.
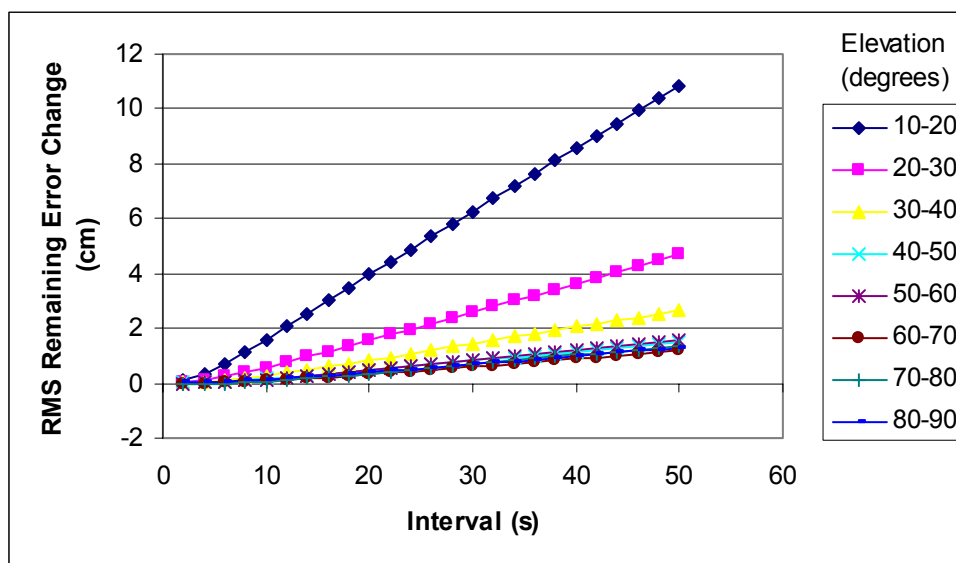


Figure 5.52: Average change in RMS of remaining error changes over time for several elevation bands with and without tropospheric correction on November 9

### 5.4.4 Autocorrelation of Remaining Errors

The remaining errors remain heavily correlated over intervals of less than 50 seconds, as shown in Figure 5.53. The errors before the tropospheric correction do decorrelate faster

than after the correction. Figure 5.54 shows the correlation over longer intervals. The remaining errors before the correction continue to decorrelate faster than the errors after the correction.
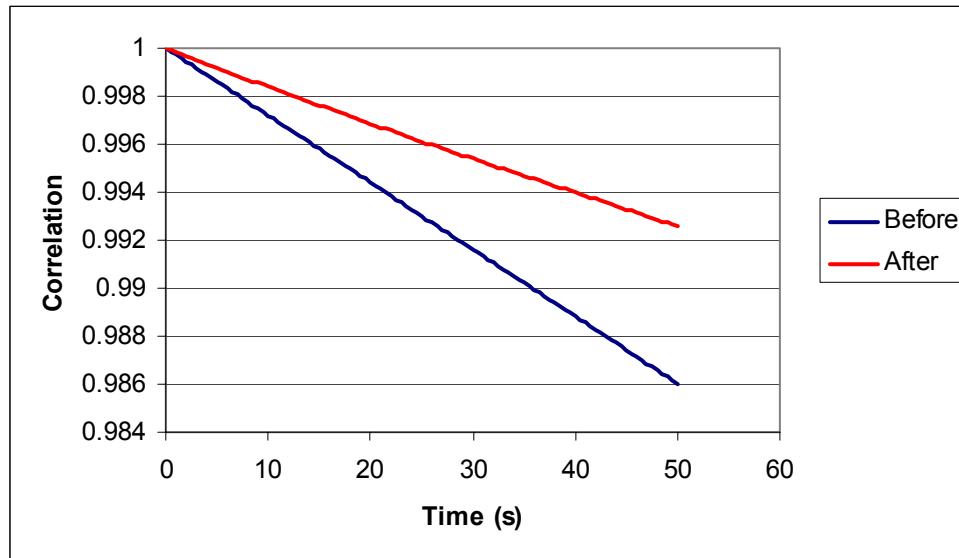


Figure 5.53: Correlation of remaining errors correction of SV 25 on November 9 before and after tropospheric correction for intervals of up to 50 seconds
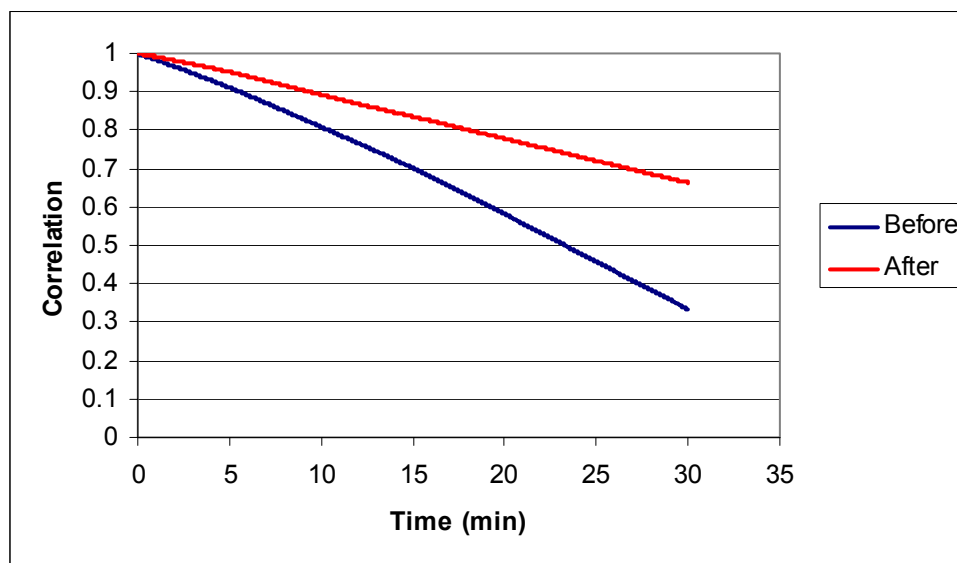
Figure 5.54: Correlation of remaining errors correction of SV 25 on November 9 before
and after tropospheric correction for intervals of up to 30 minutes

## 5.4.5 Frequency Domain Analysis of Remaining Errors

The PSD of the remaining errors before and after a tropospheric correction are shown in
Figures 5.55 and 5.56. For very low frequencies the PSD is much higher before the
tropospheric correction. However, for higher frequencies the results are very similar. As
with the PSD of the ionospheric error, the lines are very noisy in the PSD plot. Almost
all of the power is at lower frequencies, which means the impact on the position domain
will be largest at longer time intervals.

The remaining errors before and after a tropospheric correction have a similar percentage
of the power over 0.001 Hz, as shown in Figure 5.57. At very low frequencies, the
results before the correction is applied have a higher percentage, due to the impact of the
tropospheric error. The high frequency errors are responsible for more of the power once
the correction has been applied. However, the change is not as significant as other
studies, such as the difference between the satellite clock errors for each satellite block.
The long-term trends still dominate the errors. If the tropospheric correction were

perfect, it would be expected that much more of the power would be at high frequencies after the correction is applied.
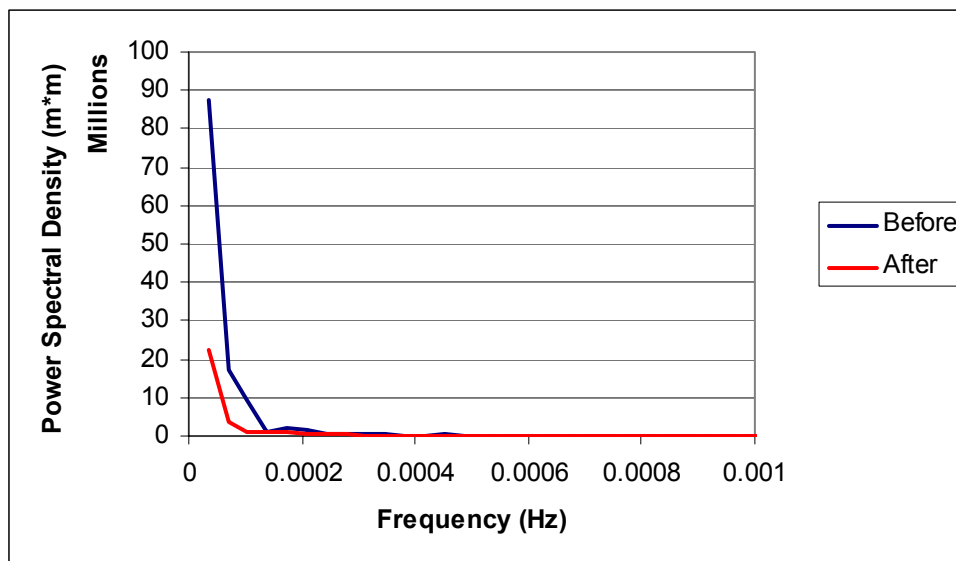


Figure 5.55: Power Spectral Density of remaining errors correction of SV 25 on November 9 before and after tropospheric correction up to 0.001 Hz
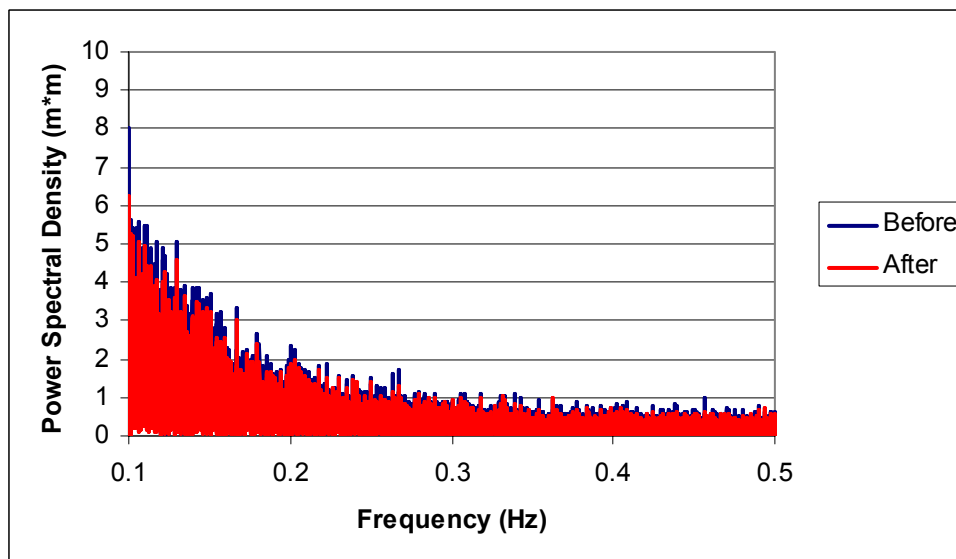


Figure 5.56: Power Spectral Density of remaining errors correction of SV 25 on November 9 before and after tropospheric correction up to 0.5 Hz
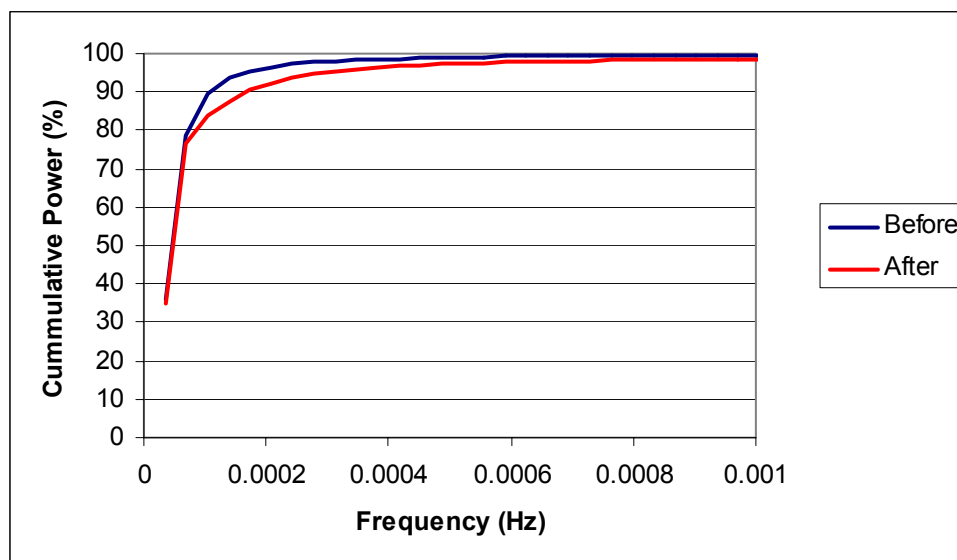
Figure 5.57: Cumulative power as a function of frequency for remaining errors of SV 25 on November 9 before and after tropospheric correction

## 5.5 Summary of Temporal Characteristics of Error Sources

A summary of the errors is given in Table 5.1. The error source with the largest changes over time periods up to 50 seconds is the ionosphere. On the day with severe ionospheric conditions the changes are very large, and the error decorrelates almost entirely over 30 minutes. This will have a very large negative effect on the precision of the relative positioning over time. On the moderate ionosphere day, the changes in the ionospheric errors are still larger than all of the other errors when a tropospheric correction is applied. The orbital errors have the most power above 0.001 Hz, with the exception of the satellite clock errors for Block II R. The large power component in this higher-frequency band will decrease the effectiveness of using precise clocks for Block II R satellites. The magnitude of the changes in the clock errors is larger than for the orbit errors over a 50 second interval, but it was shown earlier the changes are much lower for the clock errors over 30 minutes.

Table 5.1: Comparison of temporal characteristics of error sources

| Error | | RMS Change over 50 seconds (cm) | Correlation over 30 minutes | Power over 0.001 Hz (%) |
|---|---|---|---|---|
| Orbit | Across-track | 2.0 | 0.22 | 10.3 |
| | Along-track | 1.7 | 0.21 | 10.3 |
| | Radial | 0.9 | 0.23 | 10.6 |
| Satellite Clock | Block II | 4.1 | 0.30 | 3.3 |
| | Block II A | 3.5 | 0.06 | 5.1 |
| | Block II R | 2.7 | 0.15 | 30.3 |
| Ionosphere | Moderate | 7.0 | 0.52 | 1.6 |
| | Severe | 25.2 | 0.12 | 3.2 |
| Remaining | No correction | 7.1 | 0.33 | 0.5 |
| | With correction | 1.6 | 0.67 | 1.4 |

**CHAPTER 6**

**TEMPORAL BEHAVIOR OF GPS POSITION ERRORS**

This chapter contains an analysis of the change in the position errors over time. Section 6.1 gives results for the land data collected in November, 2001. Most of the results given are for November 9, with some results from November 6. The ionosphere was very active on November 6, and while it was moderate on November 9. A detailed examination of the marine data results is given in Section 6.2. Finally, Section 6.3 provides a brief assessment of the performance for the airborne data.

**6.1 Land Position Results**

This section will give the position stability results after several different corrections are applied. These corrections affect the results due to orbital, satellite clock, tropospheric, and ionospheric errors. The changes in the position errors will first be given with no corrections applied. Next the impact of the tropospheric error will be given. The tropospheric correction is nearly always applied in GPS processing. For this reason, it will be applied when the orbital, satellite clocks, and ionospheric corrections are analyzed. A table at the end of this section summarizes the results over different time intervals.

**6.1.1 Initial Results**

Figure 6.1 shows the RMS position error change over time on November 9. This is the change before any of the errors, including the tropospheric delay, have been removed. Broadcast orbits and clocks are used, along with L1 only data. The results are similar to those in past work given in Cannon et al. (2001). The RMS of the changes in the height error increases from 0.7 cm over 2 seconds to about 11.8 cm over 50 seconds. The

vertical component is the worst due to a higher DOP value in this direction. The horizontal components perform better, with a change of 5.6 cm in northing and 3.9 cm in easting over a 50 second interval.
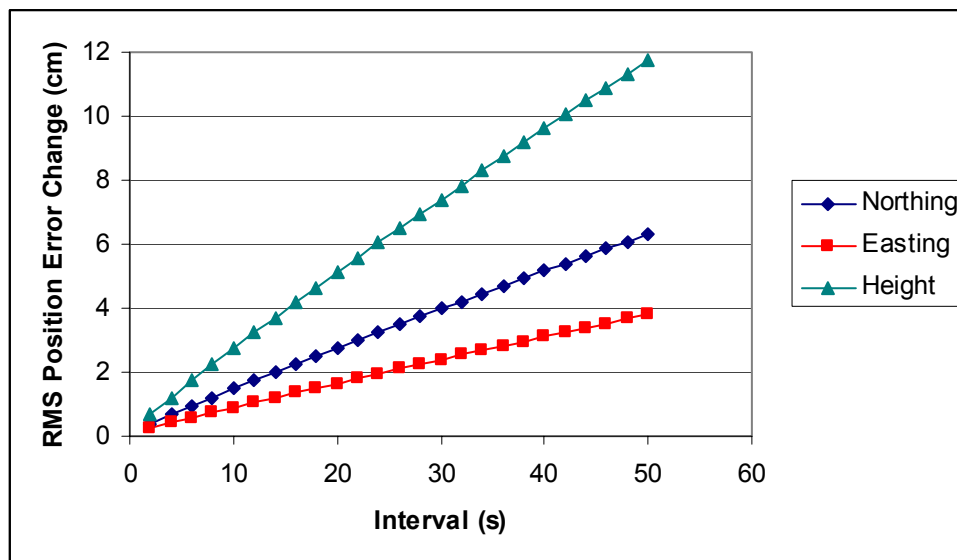


Figure 6.1: RMS position error change over time on November 9

### 6.1.2 Tropospheric Error Results

Figure 6.2 shows the changes in the position error changes after the tropospheric correction has been applied. The gray lines show the results before the tropospheric correction was used. There is an improvement in the northing and height components, especially over longer periods of time. However, for the easting component there is very little change in the changes of the errors. This suggests that the other GPS errors have a larger effect on the solution than the tropospheric error.

The tropospheric correction is almost always applied in GPS processing. For this reason, in Sections 6.1.3 to 6.1.6 the computed position error changes will be compared to the values in Figure 6.2. That will allow an realistic analysis of the impact that each error has on the results.
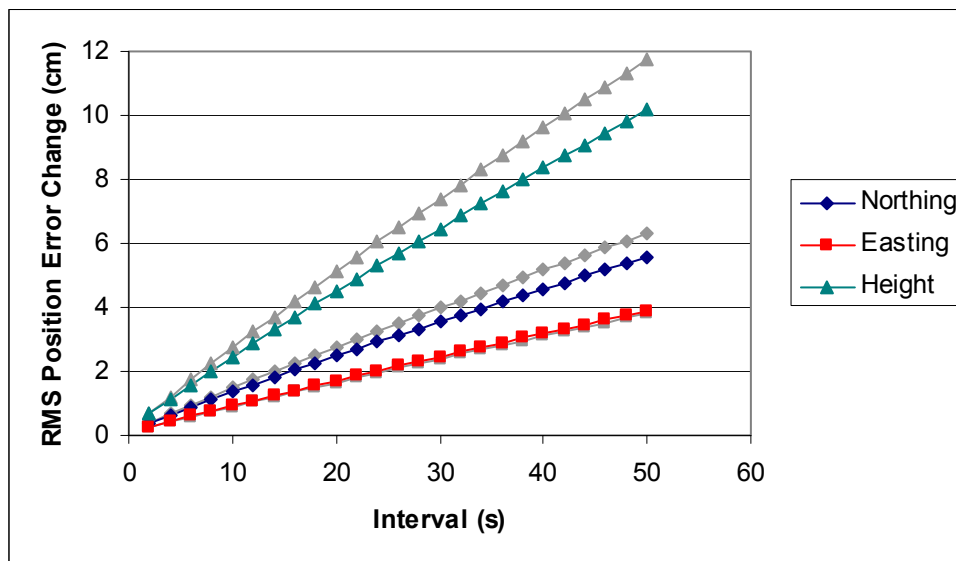
Figure 6.2: RMS position error change over time after applying tropospheric correction for November 9

## 6.1.3 Orbital Error Results

To determine the effect in the position domain, the same data used for Figure 6.2 was processed but using precise, rather than broadcast, orbits. Figure 6.3 shows the results when precise orbits are used. The gray lines in the figure indicate the results with broadcast orbits after the tropospheric correction has been applied. The difference in RMS results shows an improvement over every time period studied when the orbital errors are removed. For time intervals of more than 20 seconds the RMS reductions stay steady at about 10% in northing and easting, and 20% in height. This means the orbital error changes had a significant effect on the positions. The effect is largest over the longest time intervals, which is consistent with the power being predominantly at frequencies below 0.001 Hz for the orbital errors.
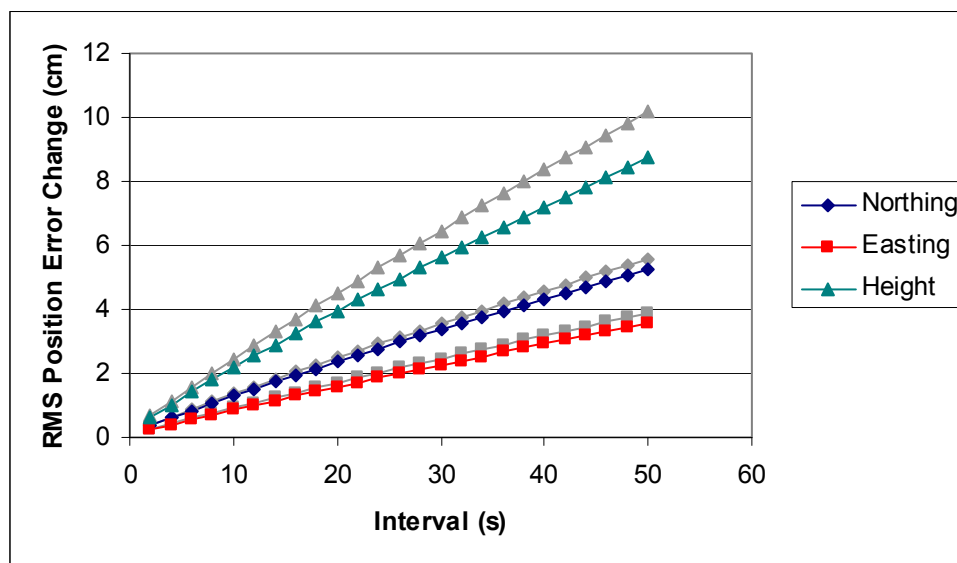
Figure 6.3: RMS position error change over time after removing orbital error for

November 9

## 6.1.4 Satellite Clock Error Results

To compute the results in Figure 6.4, the same method was used as in Figure 6.3, except precise clocks were used, along with broadcast orbits. In this case the horizontal errors are hardly changed from the initial results. The initial lines are barely even visible in Figure 6.4, since they are directly underneath the new results. The height error shows an improvement, but not as large when precise orbits are used. This suggests that errors with a long-term trend such as the orbits and ionosphere have a larger effect on the position error changes than short-term errors. As new Block II R satellites are launched, it is expected that the differences between the position error changes with and without precise clocks will be further reduced. This is because the Block II R satellite clock errors have far more power at higher frequencies than II and II A satellites.

To compute Figure 6.5, both precise orbits and clocks were used. This leads to a significant improvement in all three components at all times. This suggests that the quality of the orbits is dependent on having a better clock correction. It also suggests the

orbital and clock errors are very correlated over time.  The results in Figure 6.5 are much better than when the precise orbits and clocks were applied separately.
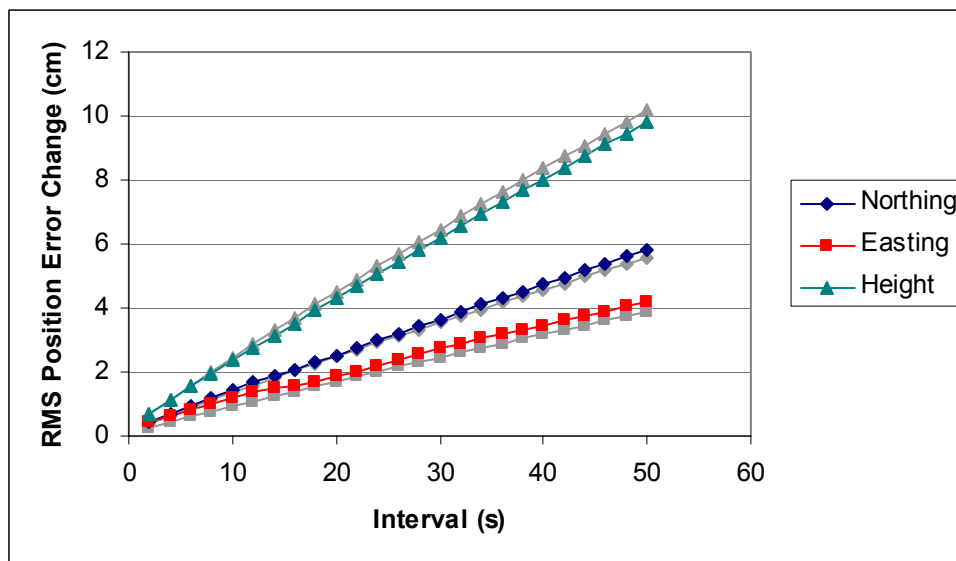


Figure 6.4: RMS position error change over time after removing satellite clock error for November 9
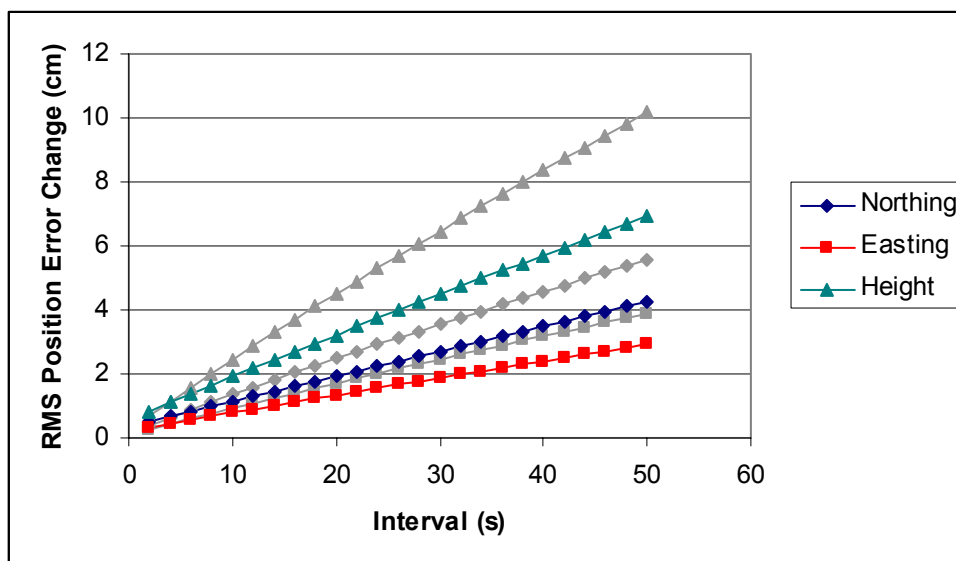


Figure 6.5: RMS position error change over time after removing orbital and satellite clock errors for November 9

**6.1.5 Ionospheric Error Results**

Figure 6.6 is a plot of the position results, with the change in the first-order ionospheric error removed through the application of the L1/L2 phase correction. The broadcast orbits and clocks are used to compute these results. Over 2 seconds the errors are substantially worse, with the RMS being over 80% higher than initially. This is due to the increased noise, since the observable is a linear combination of two measurements (L1 and L2 phase) instead of one. The noise is higher by a factor of 4.09. A derivation of the noise level of the ionospherically corrected observable can be found in Shi and Cannon (1995). However, after 10 seconds the results are better than those computed with L1 only data. The RMS improvement over 50 seconds is 21% in northing, 29% in easting, and 23% in height. As when the orbital error was removed, removing an error with a long-term trend increases the position stability over time. The interval at which the RMS values get better is important, because depending on the application, dual frequency data may not be desirable. If the range of interest was less than 10 seconds, an ionospheric correction should not be applied.
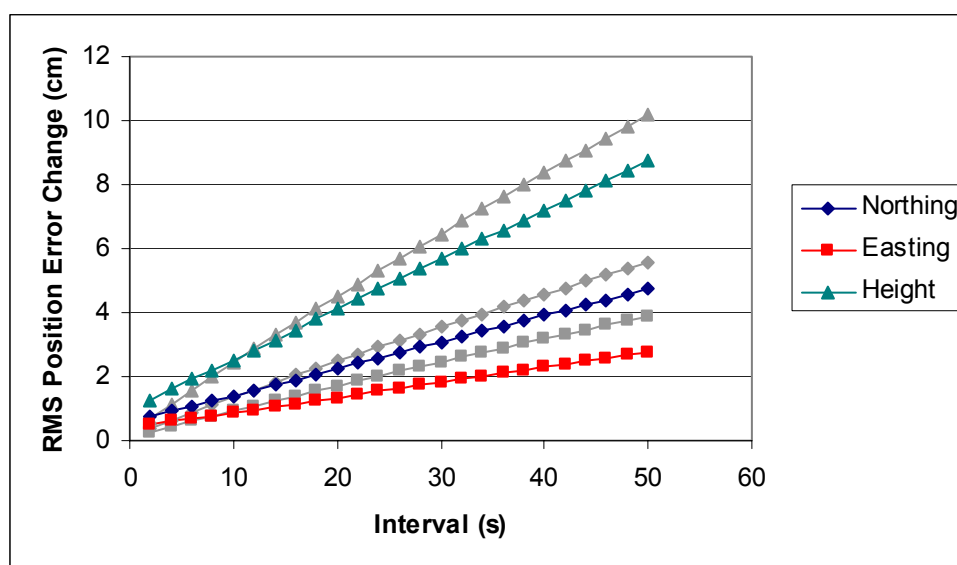


Figure 6.6: RMS position error change over time after removing ionospheric error for November 9

It has been previously shown that the ionospheric errors changed much more quickly on November 6 than on November 9.  Figures 6.7 and 6.8 show the results using L1 only data and then L1/L2 carrier phase observations on November 6.  With L1 only data, the results are much worse than those with a moderate ionosphere.  When dual frequency measurements are used, the RMS values are decreased by 50%.  In addition, when the changes in the ionospheric errors are removed, the results in the position domain are about the same as when dual frequency data is used on November 9.  The change in RMS values of the position error changes is higher due to the faster decorrelation of the ionospheric errors, as well as the fact that the ionospheric errors had a higher magnitude.  The point at which the dual frequency solution provides better results than with L1 only data is a 6 second interval.  This is lower than on November 9, suggesting the impact of removing the first-order ionospheric error is much more important on a day with a storm event.
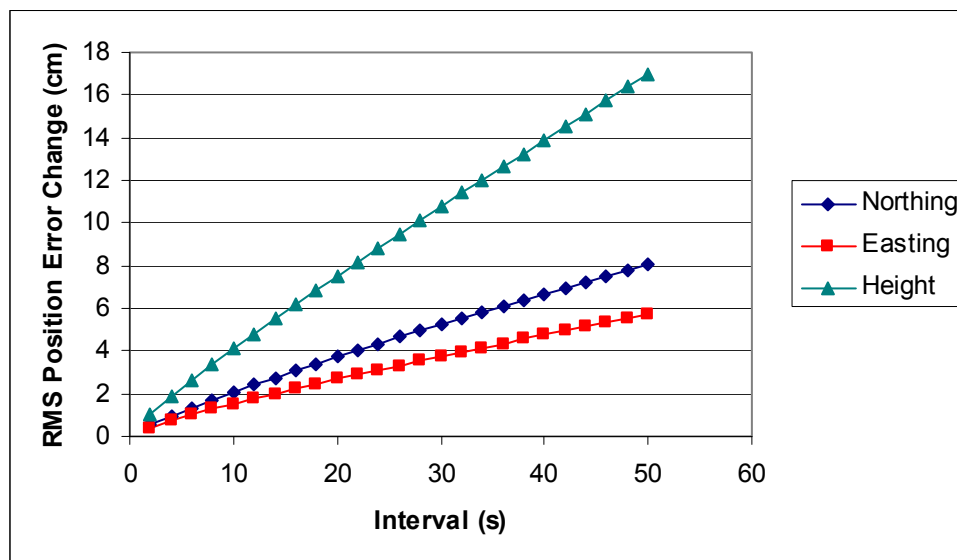


Figure 6.7: RMS position error change over time after removing only tropospheric error for November 6
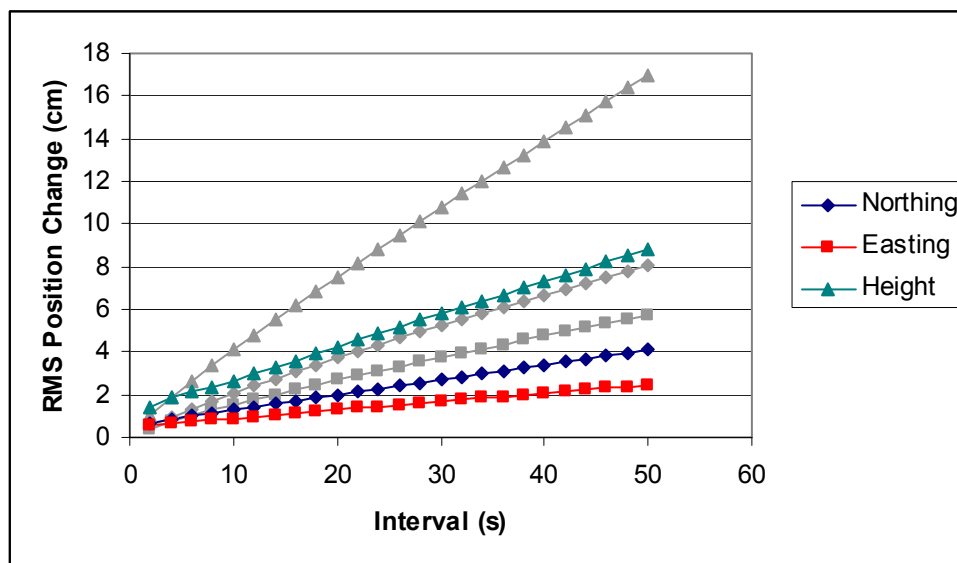
Figure 6.8: RMS position error change over time after removing ionospheric error for

November 6

## 6.1.6 Combination of All Four Error Results

Figure 6.9 shows the results when precise orbits, precise clocks, and dual frequency phase observations are used, in addition to applying the tropospheric correction. The RMS values are not improved for time intervals of less than 6 seconds, due to the increased noise of the linear combination of L1 and L2 phase measurements. This is lower than the 10 second level shown in Section 6.1.5. Once the positions are better, the improvement in RMS gradually increases to 54% in easting, 46% in northing, and 54% in height over 50 seconds. The remaining errors in the solution are due to factors such as receiver noise, multipath, and the inaccuracy in modeling the wet delay of the troposphere. The results for the severe ionospheric day are given in Figure 6.10. The changes in the position errors are similar to the results on the typical ionosphere day.
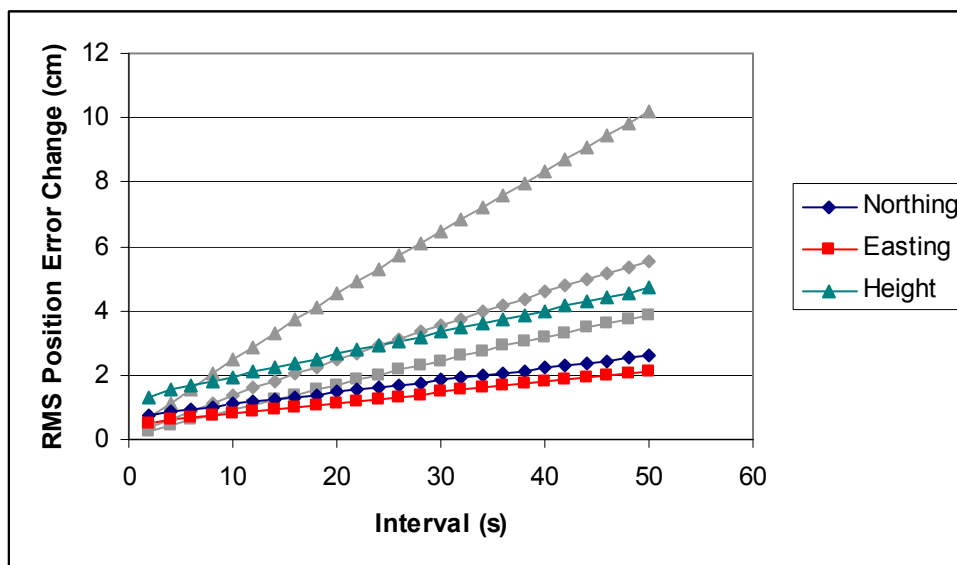
Figure 6.9: RMS position error change over time after removing ionospheric, satellite clock, and orbital error for November 9
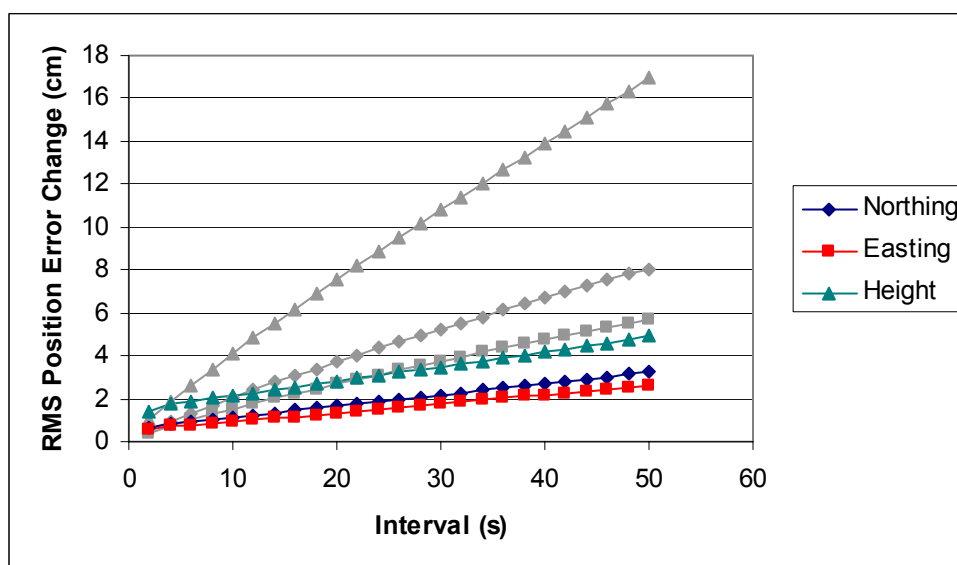


Figure 6.10: RMS position error change over time after removing ionospheric, satellite clock, and orbital error for November 6

**6.1.7 Comparison of Results**

The percentage improvement of the RMS values when all four errors are considered over the initial results is shown in Figure 6.11. As explained earlier, the results are much worse over short time periods, due to the ionospheric correction. However, for periods of greater than 10 seconds there is a significant improvement in all directions.
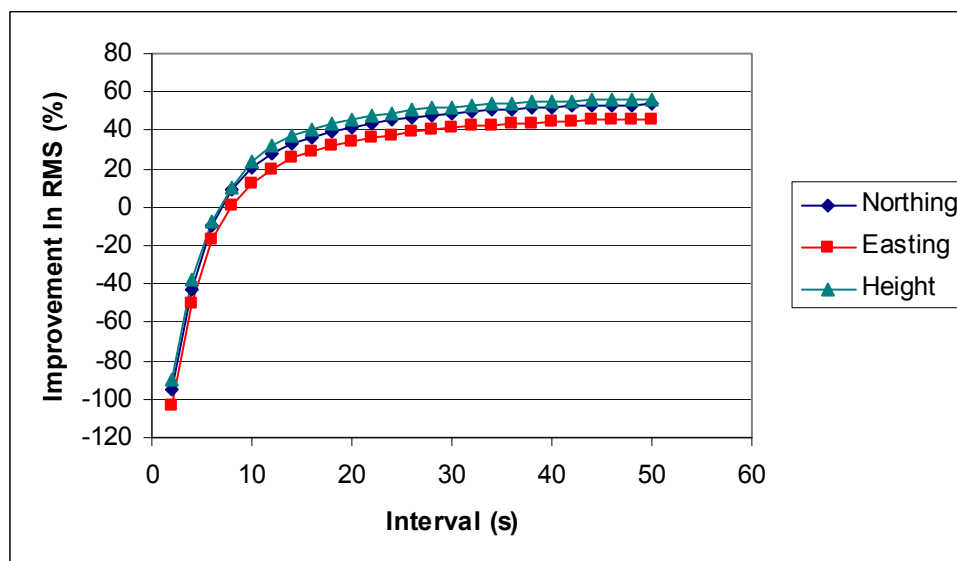


Figure 6.11: Improvement in RMS position error change over time after considering all four errors for November 9

A comparison of the results is given in Table 6.1. In this table the RMS is given in cm, while the column labeled % is the percentage improvement in the solution, as compared to the results when only the tropospheric correction is applied. The improvements are largest over the longest time intervals. When all of the errors are removed, over a 50 second interval the change in the height error is reduced from 10.2 to 4.7 cm. In real time, only the ionospheric and tropospheric corrections could be applied, which would lead to a solution weaker than the post-mission results.

Table 6.1: Comparison of RMS position error changes on November 9

| | Interval | Northing | | Easting | | Height | |
|---|---|---|---|---|---|---|---|
| | | RMS | % | RMS | % | RMS | % |
| None | 2 | 0.4 | | 0.3 | | 0.7 | |
| Orbit | | 0.4 | **2** | 0.3 | **3** | 0.6 | **5** |
| Clock | | 0.4 | **-4** | 0.3 | **-8** | 0.7 | **2** |
| Orbit/Clock | | 0.5 | **5** | 0.3 | **0** | 0.6 | **9** |
| Ionosphere | | 0.7 | **-91** | 0.5 | **-85** | 1.3 | **-88** |
| All | | 0.7 | **-86** | 0.5 | **-110** | 1.3 | **-80** |
| None | 10 | 1.5 | | 0.9 | | 2.7 | |
| Orbit | | 1.3 | **13** | 0.9 | 0 | 2.2 | 19 |
| Clock | | 1.4 | **7** | 0.9 | 0 | 2.4 | 11 |
| Orbit/Clock | | 1.1 | **27** | 0.8 | 11 | 1.9 | 30 |
| Ionosphere | | 1.4 | **7** | 0.9 | 0 | 2.5 | 7 |
| All | | 1.1 | **27** | 0.8 | 11 | 1.9 | 30 |
| None | 20 | 2.8 | | 1.7 | | 5.1 | |
| Orbit | | 2.4 | **14** | 1.6 | 6 | 3.9 | 24 |
| Clock | | 2.5 | **11** | 1.8 | -6 | 4.4 | 14 |
| Orbit/Clock | | 1.9 | **32** | 1.4 | 18 | 3.2 | 37 |
| Ionosphere | | 2.2 | **21** | 1.4 | 18 | 4.1 | 20 |
| All | | 1.5 | **46** | 1.1 | 35 | 2.6 | 49 |
| None | 50 | 5.6 | | 3.9 | | 10.2 | |
| Orbit | | 5.3 | **5** | 3.5 | **10** | 8.7 | **15** |
| Clock | | 5.9 | **-5** | 4.2 | **-8** | 9.8 | **4** |
| Orbit/Clock | | 4.3 | **23** | 2.9 | **26** | 6.9 | **32** |
| Ionosphere | | 4.6 | **21** | 2.8 | **29** | 8.6 | **23** |
| All | | 2.6 | **54** | 2.1 | **46** | 4.7 | **54** |

A comparison of the results on the extreme ionospheric day over a 50 second interval is given in Table 6.2. When all of the errors are removed, the change in height error improves from 17.0 to 4.9 cm.

Table 6.2: Comparison of RMS position error changes over a 50 second interval on November 6

|  | Northing | | Easting | | Height | |
|---|---|---|---|---|---|---|
|  | RMS | % | RMS | % | RMS | % |
| None | 8.1 |  | 5.7 |  | 17.0 |  |
| Ionosphere | 4.1 | **49** | 2.5 | **56** | 8.8 | **48** |
| All | 3.3 | **59** | 2.6 | **54** | 4.9 | **71** |

## 6.2 Marine Position Results

The marine position results will be presented in the same manner as the land data. As mentioned in section 4.2.3, the truth positions were determined using fixed integer ambiguity double difference positioning.

The results before any errors have been removed are given in Figure 6.12. These results are worse than those computed with the land data. This is due to a number of factors, such as the less satellites in view, which leads to a higher PDOP, and the time of day of the data set. As mentioned earlier, the time of day is 13:20-15:10, which is when the ionosphere is changing rapidly.

A plot of the changes in the position errors after the tropospheric correction has been applied to the measurements is given in Figure 6.13. The results are improved in the easting and height, but are somewhat worse in the northing direction. The temperature

was about -10° C when the measurements were taken, which would reduce the magnitude of the wet part of the tropospheric delay. This is taken into account, but it is clear that the troposphere was not a main driver of the errors in this case.
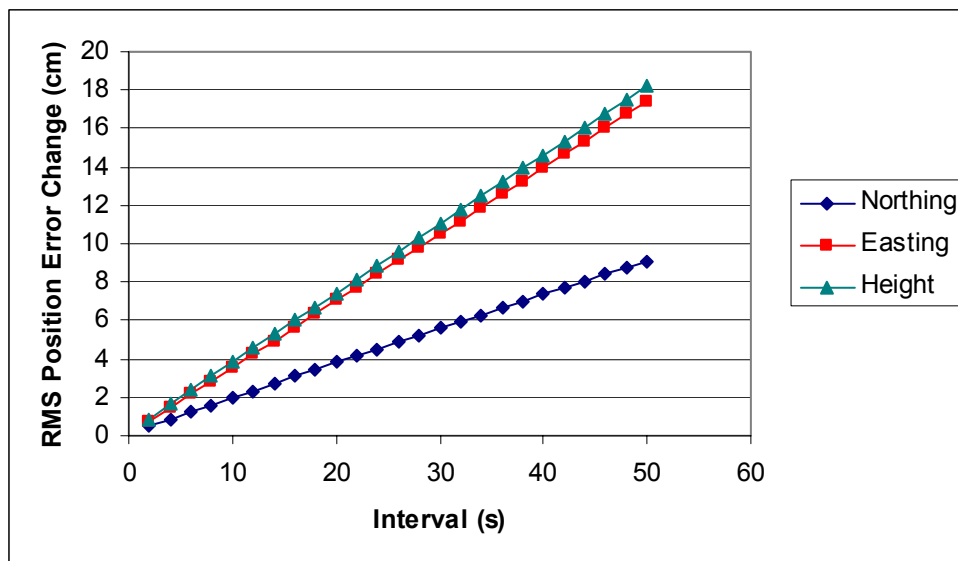


Figure 6.12: RMS position error change over time for marine data
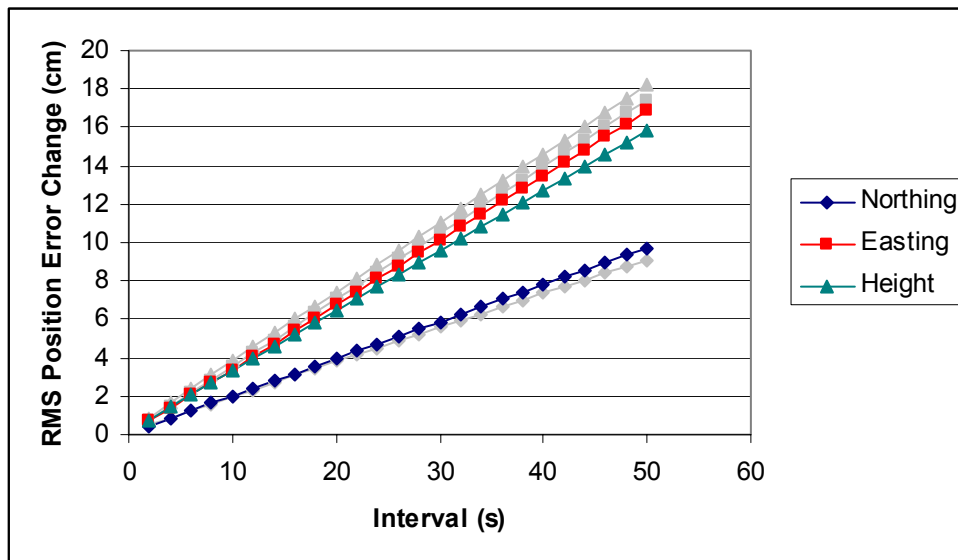


Figure 6.13: RMS position error change over time after applying tropospheric correction for marine data

The results in Figure 6.14 show the position error changes when precise orbits are used. The results are little changed from the initial results in Figure 6.13. The precise orbits have very little effect in this case. As mentioned in Section 5.1.1, the orbital error changes are smaller on this day than for the land data, in large part because the worst two satellites for the land data are not in the solution. This may be part of the reason why using the precise orbits has so small an effect.
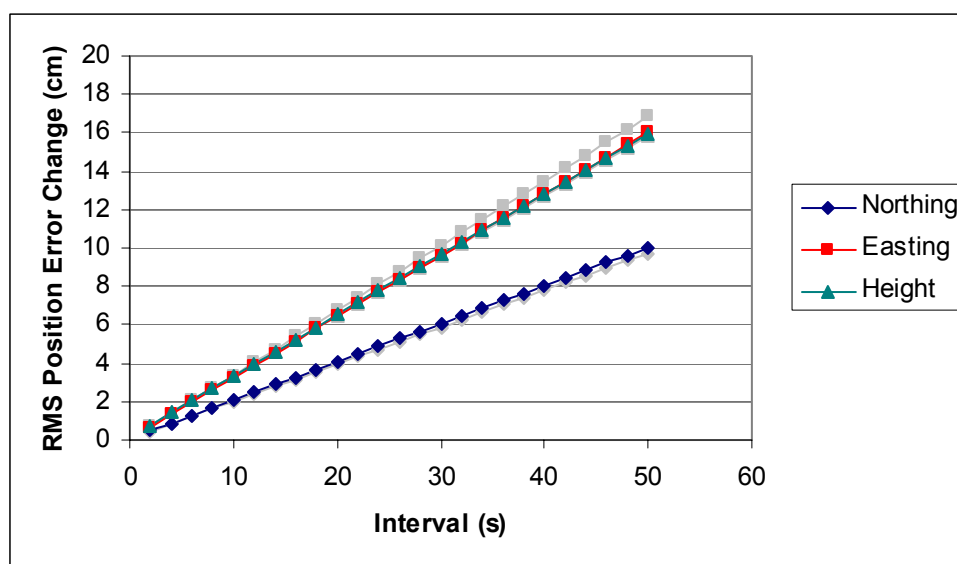


Figure 6.14: RMS position error change over time after removing orbital error for marine data

Figure 6.15 shows the results when precise clocks and broadcast orbits are used. The results are better in the horizontal components, but not in the height. These improvements are the opposite of the land data case. In both the land and marine cases, the effect on the position errors was not large when the precise clocks were used alone, without the precise orbits.
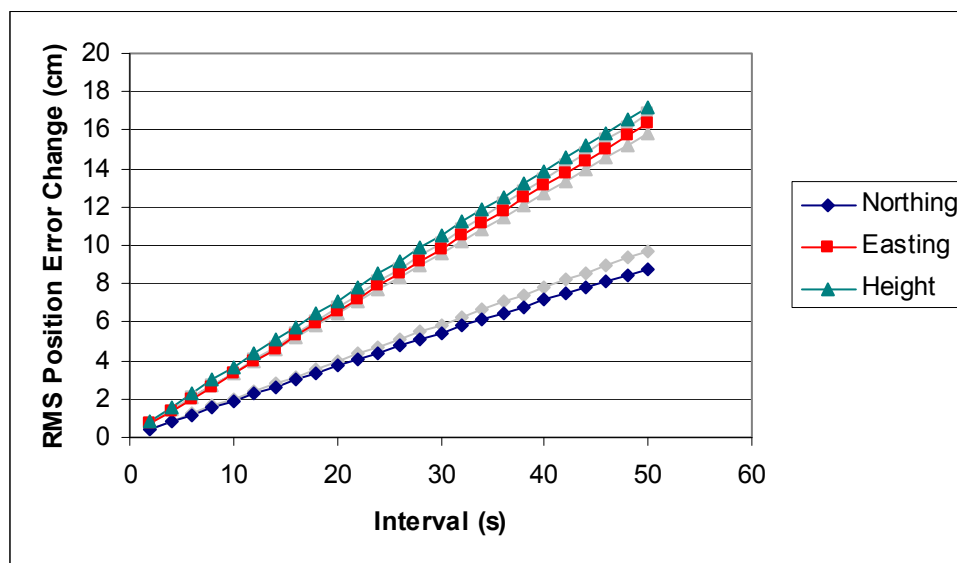
Figure 6.15: RMS position error change over time after removing satellite clock error for marine data

Both precise orbits and clocks were used to generate the results given in Figure 6.16. As in the case where precise clocks alone are used the results are better horizontally and worse vertically, compared with the initial results. This suggests that problems other than the orbits and clocks are main drivers of the changes in the height errors for the ship data. The geometry is much poorer for the marine case than the land case, which leads to positions with less accuracy.

The RMS change in the position errors when dual frequency data is used is given in Figure 6.17. There is a substantial improvement in all three directions. The ionospheric error clearly had a very large effect on the position errors. Over a time interval of 50 seconds the results improve by 36-52%. The results are somewhat worse for time intervals of less than 6 seconds, but after that there is a significant reduction in the change of the position errors. As with the land data case, removing the change in the ionospheric error leads to a large improvement in the computed position stability.
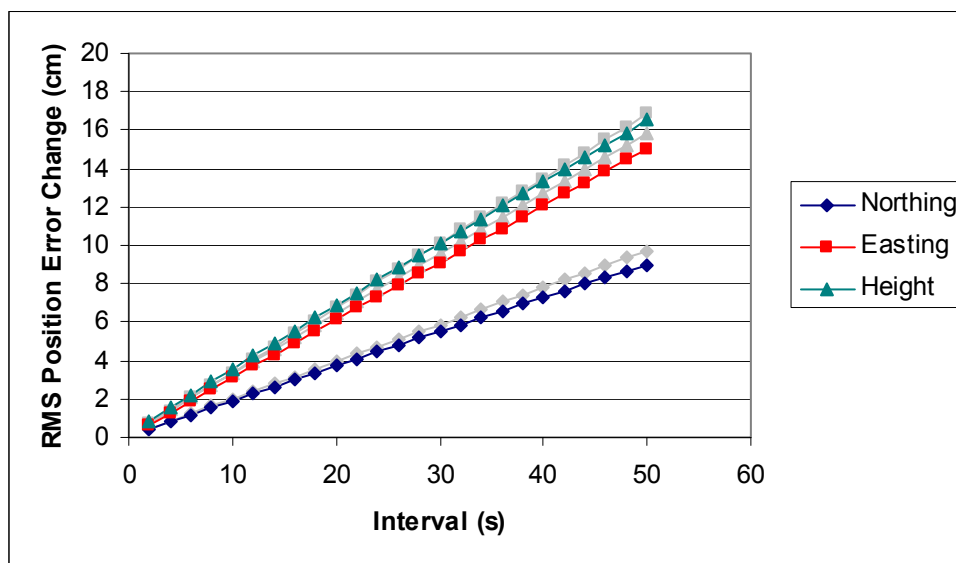
Figure 6.16: RMS position error change over time after removing satellite clock and orbital errors for marine data
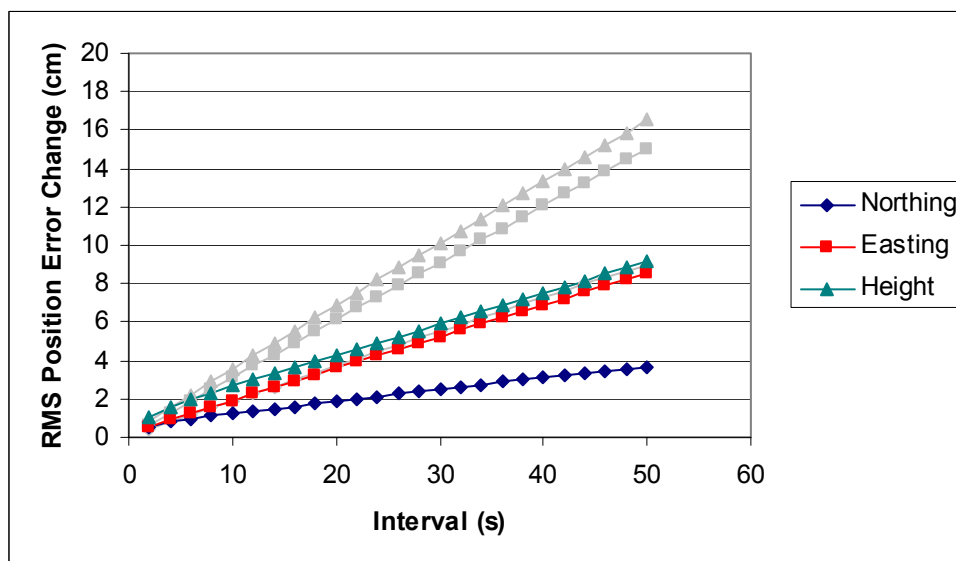


Figure 6.17: RMS position error change over time after removing ionospheric error change for marine data

The results when all four errors are considered are shown in Figure 6.18. These results are much better than the initial results with only a tropospheric correction applied. The

improvement in all three directions varies from 43-63%, which is similar to the land data case. Removing all errors yields much better results than with broadcast orbits and clocks with L1 only data. The remaining error is still larger than in the land case, likely due to the geometry of the satellite constellation and inaccuracy of the computed truth position.
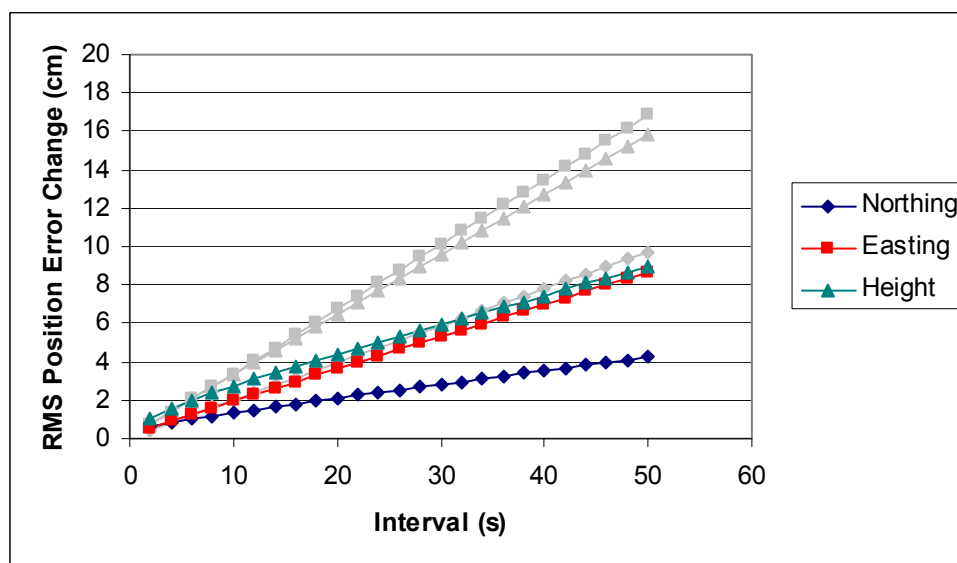


Figure 6.18: RMS position error change over time after removing ionospheric, satellite clock, and orbital error for marine data

A comparison of the marine results is given in Table 6.3. The ionosphere had a much larger effect in the marine case than for the land data. This is because the marine data was collected only in the afternoon, while the static data was collected for 24 hours a day. Over a 10 second interval, applying an ionospheric correction has a large positive effect on the marine data results, while the effect was much smaller for the static data.

Table 6.3: Comparison of RMS position error changes for marine data

| | Interval | Northing | | Easting | | Height | |
|---|---|---|---|---|---|---|---|
| | | RMS | % | RMS | % | RMS | % |
| None | 2 | 0.5 | | 0.7 | | 0.8 | |
| Orbit | | 0.5 | **-3** | 0.7 | **4** | 0.8 | **0** |
| Clock | | 0.5 | **0** | 0.7 | **1** | 0.9 | **-14** |
| Orbit/Clock | | 0.5 | **1** | 0.6 | **7** | 0.8 | **-7** |
| Ionosphere | | 0.5 | **-16** | 0.5 | **21** | 1.0 | **-31** |
| All | | 0.6 | **-20** | 0.5 | **20** | 1.1 | **-38** |
| None | 10 | 2.0 | | 3.4 | | 3.3 | |
| Orbit | | 2.1 | **-5** | 3.2 | **6** | 3.3 | **0** |
| Clock | | 1.9 | **5** | 3.3 | **3** | 3.7 | **-12** |
| Orbit/Clock | | 1.9 | **5** | 3.0 | **12** | 3.6 | **-9** |
| Ionosphere | | 1.3 | **35** | 2.0 | **41** | 2.7 | **18** |
| All | | 1.2 | **40** | 1.9 | **44** | 2.7 | **18** |
| None | 20 | 3.9 | | 6.7 | | 6.5 | |
| Orbit | | 4.1 | **-5** | 6.4 | **4** | 6.5 | **0** |
| Clock | | 3.7 | **5** | 6.6 | **1** | 7.1 | **9** |
| Orbit/Clock | | 3.7 | **5** | 6.1 | **9** | 6.9 | **-6** |
| Ionosphere | | 2.2 | **44** | 3.9 | **42** | 4.6 | **29** |
| All | | 1.9 | **51** | 3.6 | **46** | 4.3 | **34** |
| None | 50 | 9.7 | | 16.9 | | 15.9 | |
| Orbit | | 10.0 | **-3** | 16.0 | **5** | 16.0 | **-1** |
| Clock | | 8.8 | **9** | 16.3 | **4** | 17.2 | **-8** |
| Orbit/Clock | | 8.9 | **8** | 15.0 | **11** | 16.5 | **-4** |
| Ionosphere | | 4.7 | **52** | 9.4 | **44** | 10.2 | **36** |
| All | | 3.6 | **63** | 8.6 | **49** | 9.1 | **43** |

**6.3 Airborne Data Results**

The airborne data results when using precise orbits, clocks, dual frequency observations, and a tropospheric correction are given in Figure 6.19. The results when only the tropospheric correction was applied are given in gray lines on the figure. The results have similar magnitudes than those computed with the boat data. It should be noted that these results are probably higher than the true values, since the errors were computed relative to the multi-reference station differential GPS solution. A comparison of the airborne results in the position domain over a 50 second interval is given in Table 6.4. The results improve with each correction, although in some cases the improvement is small. The ionosphere has the largest effect, with the RMS of the position error changes decreasing 24-39% when dual frequency data is used.
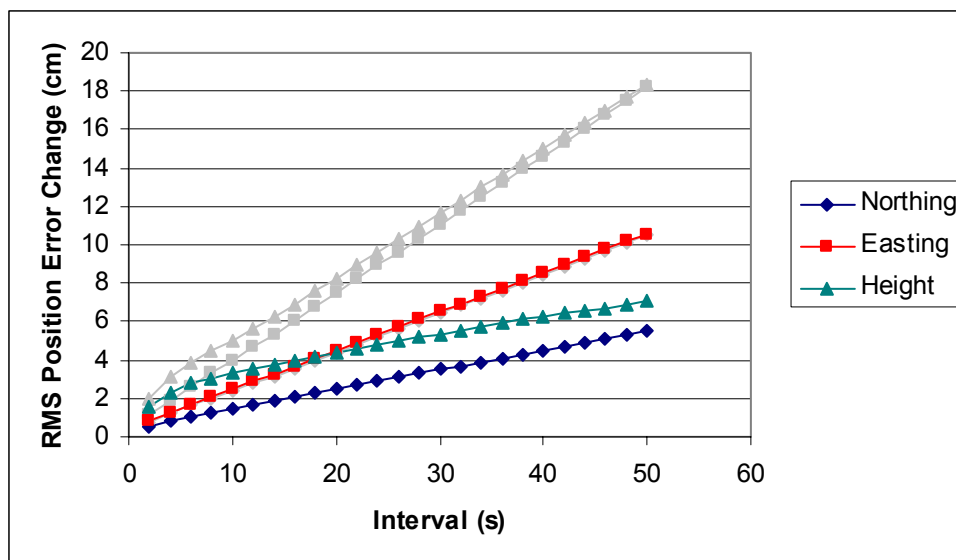


Figure 6.19: RMS position error change over time after removing ionospheric, satellite clock, and orbital error for airborne data

Table 6.4: Comparison of RMS position error changes over a 50 second interval for airborne data

|  | Northing | | Easting | | Height | |
|---|---|---|---|---|---|---|
|  | RMS | % | RMS | % | RMS | % |
| None | 10.5 |  | 18.2 |  | 18.3 |  |
| Orbit | 8.8 | **16** | 17.8 | **2** | 14.9 | **19** |
| Clock | 10.3 | **2** | 17.9 | **2** | 16.3 | **11** |
| Orbit/Clock | 8.4 | **20** | 15.2 | **16** | 11.7 | **36** |
| Ionosphere | 6.4 | **39** | 13.9 | **24** | 13.0 | **29** |
| All | 5.4 | **49** | 10.3 | **43** | 7.1 | **61** |

# CHAPTER 7

# CONCLUSIONS AND RECOMMENDATIONS

For an airborne magnetometry application relative (over time) positions must be accurate to the level of a few centimetres over intervals of 2-50 seconds. Several GPS error sources change temporally, which leads to a change in the errors in the computed position. For this reason, the temporal characteristics of many different GPS error sources have been investigated. These errors include the orbital, satellite clock, and ionospheric errors. The temporal characteristics of these errors have been analyzed independently. Other GPS error sources include errors due to the troposphere, multipath, and noise. Satellite clock and orbit errors were analyzed by comparing broadcast and precise satellite clock corrections and orbits. Dual frequency carrier phase data was used to assess the change in the ionospheric error. The remaining errors, which include the tropospheric error, multipath, and noise were investigated together. Several tests were conducted to assess the change of these GPS errors using time and frequency analyses. Once these errors were investigated, the effect of each error in the position domain was investigated. A new carrier smoothing method was developed, as well as an algorithm to remove position jumps due to a change in satellites. Finally, the results in the position domain were given after removing all errors, and a comparison to the initial results was shown.

## 7.1 Measurement Domain Conclusions

The RMS of the changes in orbital errors over time increased in a linear manner as a function of time, with trends of many hours being evident in the errors. The radial component had the smallest changes as a function of time, and decorrelated the slowest. The magnitude of the changes in the errors was very similar from day to day. In the frequency domain each of the across-track, along-track, and radial errors had similar

characteristics. The power of the orbital errors is primarily at low frequencies. Over a 50 second interval, the average RMS of the change in the three-dimensional error was 2.8 cm, while the radial component of the error changed 0.9 cm. Over 30 minutes the changes increased to 70 cm for the three-dimensional error, and 30 cm for the radial component.

Satellite clock errors also increased as a function of time, but not linearly. There are also significant differences in the performances of the clocks depending on which satellite Block it is. The satellites have different types of oscillators depending on the satellite Block. Block II satellites were launched in 1989-1990, Block II A in 1990-1997, and Block II R in 1997-2001. The Block II R satellites performed the best, followed by Block II A, with Block II satellites having the poorest performance over intervals of less than 28 minutes. The average RMS change of the satellite clock error over 50 seconds was 2.7 cm for Block II R satellites, 3.5 cm for Block II A, and 4.2 cm for Block II. Over 30 minutes, the average RMS changes are 7 cm for Block II R, 30 cm for Block II A, and 29 cm for Block II. Block II R satellite clock errors have much more power at high frequencies than either Block II or II A satellites. Also, Block II R satellite clock errors decorrelated much faster than those of the other two Blocks. As with the orbital errors, the changes in errors were very similar from day to day. As new Block II R satellites are launched, the changes in the average RMS changes over time is expected to decrease, due to the superior performance of the rubidium oscillators in these satellites.

Changes in the ionospheric errors are not similar from day-to-day. The results are dependent upon the conditions in the ionosphere, the elevation angle of the satellite, and the time of day. Low elevation satellites had the largest ionospheric error changes over time. The RMS results were the worst during the ionospheric storm on November 6, and also the least correlated. On November 6 the average RMS change over 50 seconds was 25 cm, as compared to 4-7 cm on the moderate days. The changes in the ionospheric errors increased significantly as the elevation angle decreased.

Changes in the remaining errors are due to the troposphere, multipath, noise, and higher-order ionospheric effects. These errors are much different depending on whether or not a tropospheric correction has been applied. The tropospheric error has a trend of several hours that is heavily influenced by the elevation of the satellite. The multipath and noise are affected, although much less than the troposphere, by the elevation angle. The tropospheric correction is not perfect, especially when modeling the wet delay. Due to this problem, after the tropospheric correction is applied to the remaining errors, there is still a trend of many minutes. The errors decorrelate much faster before a tropospheric correction is used, but the frequency of the errors is similar. When a tropospheric correction is applied the average RMS of the change in the remaining errors is 1.6-1.8 cm over 50 seconds, and about 1.1 cm above 30° elevation.

The changes have the highest magnitude for the ionospheric error. Changes in this error also had a large effect on relative (over time) GPS positions. The variability in the ionospheric error from day-to-day means that the atmospheric conditions should be considered whenever GPS data is collected. The effects of the other errors such as the satellite clock and orbital errors are also significant, and should be minimized for the most accurate single point GPS positions.

## 7.2 Position Domain Conclusions

When the orbital errors were removed and the positions were computed, the changes in the errors decreased in every component in the land data case. The largest change was 15% in the height component, from 10.2 to 8.7 cm over a 50 second interval. The airborne data showed similar results, with the changes in the height component decreasing from 18.3 to 14.9 cm over 50 seconds. In the marine case removing only the orbital errors had little effect on the position results. The northing and height degraded by 1-3%, while the easting component improved 5%. In most cases, the results improve with the precise orbits, so they should be used if available.

When only the satellite clocks errors were removed the effect on the land results was not large, with only the height component having a noticeable improvement. However, when both precise clocks and orbits were used, there was a significant advantage, with the height improving up to 32%. The RMS change in the height component over 50 seconds was reduced from 10.2 to 6.9 cm. The marine data results got worse when precise clocks were used, as well as when precise clocks and orbits were used. This suggests other errors and the geometry had a larger effect on the marine data than the land data. For the airborne data, only the height component showed a significant change with precise clocks. The height improved 11% from 18.3 to 16.9 cm, while the other two components only changed 2%. Using both precise orbits and clocks leads to much better performance, with the RMS changes in the height falling to 11.7 cm over a 50 second interval. Based on these results, it is of little value for this application to use precise clocks without using precise orbits. However, if both precise orbits and clocks are available they should be used.

Using L1 and L2 phase data to remove the changes in the ionospheric error on a typical day resulted in gains of better than 20% in all three components for the land data, and better than 35% for the marine data. The RMS change in height over 50 seconds was reduced from 10.2 to 8.6 cm for the static data, 15.9 to 10.2 cm on the boat, and 18.3 to 13.4 cm on the airplane. However, over very short time intervals the accuracy was degraded due to the increased noise. On a day with higher variability in the ionosphere, applying the correction to the land data led to improvements over a 50 second interval of about 50% in all components, with a reduction from 17.0 to 8.8 cm in height. In general removing long-term errors has a larger effect than short-term errors on the stability of the position solution. Dual frequency data is very beneficial for this application, and in should certainly be used in real-time processing, unless the time interval of interest is less than 10 seconds.

When all four errors were removed, the improvement was 46-54% in all three directions for the land data. Over 50 seconds, the RMS of the positions changes decreased from 5.6

to 2.6 cm in northing, 3.9 to 2.1 cm in easting, and 10.2 to 4.7 cm in height. For the marine data the improvement was 43-63% in all three directions. The RMS of the position error changes over 50 seconds decreased from 9.7 to 3.6 cm in northing, 16.9 to 8.6 cm in easting, and 15.9 to 9.1 cm in height. The aircraft data also showed a significant improvement, with the changes in the position errors decreasing 43-61%. The RMS of the changes in the position errors for the airborne data decreased from 10.5 to 5.4 cm in northing, 18.2 to 10.5 cm in easting, and 18.3 to 7.1 cm in height over a 50 second interval. Using each of precise orbits, precise clocks, dual frequency data, and a tropospheric correction leads to the best possible relative (over time) positioning results over a 10-50 second time interval.

## 7.3 Recommendations

The research presented in this thesis has shown that using precise orbits and clocks, in addition to dual-frequency data, is beneficial to obtaining the best possible relative (over time) positioning results. Based on this research, the following recommendations can be made:

1) Investigate using a high quality inertial navigation unit to assist in computing stable positions over time, and ensure data continuity. Inertial systems use three accelerometers and three gyroscopes to determine the accelerations in the earth's reference frame. The accelerations can be integrated twice to obtain positions, but are very unstable over long time periods (Nayak, 2000). It is possible that using an inertial system would give better results over very short time periods, although over long intervals the results would probably degrade.

2) Monitor the significance of ionospheric error changes as time moves further away from the solar maximum. As mentioned earlier, the solar maximum has led to increased storm activity, which should peak in 2001-2003 (Skone et al., 2001). Once this time has past, it is expected that the changes in the ionospheric errors

will decrease, which should increase the interval at which the single frequency solution has lower changes in the position errors over time. In this thesis, that interval was 10 seconds on a typical day, and 6 seconds on the severe day for the land data.

3)      Evaluate the effect of a new carrier frequency on the estimated positions. This will not be available for a few years, but once it is the new phase measurement will allow more accurate computation of the ionospheric effect. Since the new frequency will not be encrypted the resulting phase measurement should be less noisy than the current L2 measurement. As with the second recommendation, this will change the interval at which the single frequency results are better than dual frequency. However, in this case it is expected the interval will decrease.

4)      Evaluate the effect of using an external oscillator as the receiver clock on the position errors, and remaining measurement errors studied in Section 5.4.

5)      Continue to examine the clock stability of new satellites that get launched. It is expected that newer clocks will have a less significant low-frequency errors than the current clocks. This probably will decrease the impact of using precise clocks in calculating the position.

6)      Continue to study the orbital error changes as new satellites get launched and the control segment continues to improve.

# REFERENCES

Auld, J. (2000). GPS Performance Evaluation During the SA Turn Down May 2, 2000. Viewgraphs of presentation at Institute of Navigation – Alberta Chapter Meeting, Calgary, Alberta, June 2.

Beutler, G., R. Weber, U. Hugentobler, M. Rothacher, and A. Verdun. (1998). GPS for Geodesy, Chapter 2: GPS Satellite Orbits, Springer-Verlag, pp. 43-109.

Braasch, M. and F. van Graas. (1991). Guidance Accuracy Considerations for Real time GPS Interferometry. Proceedings of ION GPS-91, Albuquerque, New Mexico, September 9-13, pp. 373-386.

Brozena, J. and V. Childers. (2000). The NRL Airborne Geophysics Program. International Association of Geodesy Symposia, Volume 121, Geodesy Beyond 2000 - The Challenges of the First Decade, pp. 125-129.

Bruton, A. (2000). Improving the Accuracy and Resolution of SINS/DGPS Airborne Gravimetry. PhD thesis, Department of Geomatics Engineering, University of Calgary, December.

Cannon, M. E., G. Lachapelle, M. Olynik, M. G. Petevello, B. Gelatka, and J. Davis. (2001). P3 Aircraft Buffeting Using Precise Carrier Phase Techniques. Proceedings of ION GPS-2001, Salt Lake City, Utah, September 11-14, pp. 1009-1016.

Cannon, M. E., W. Zhang, and L. Fortes. (2002). Airborne Data Processing Using Multi-Ref in Post-Mission, Report to Applanix Corporation, University of Calgary.

Challstrom, C. (1999). The Benefits of GPS Modernization. Quarterly Newsletter of the Institute of Navigation, Volume 9, Number 2, Summer.

Cheney, W., and D. Kincaid. (1994). Numerical Methods in Computing. Brooks/Cole Publishing Company, p. 134.

Doherty, P., P. Gendron, R. Loh, and D. Anderson. (1997). The Spatial and Temporal Variations in Ionospheric Range Delay. Proceedings of ION GPS-97, Kansas City, Missouri, September 16-19, pp. 231-240.

European Union (EU). (2002). Galileo: Yes at Last! Press Release, March 26.

Fortes, L. (2002). Optimizing the Use of GPS Multi-Reference Stations for Kinematic Positioning. PhD thesis, Department of Geomatics Engineering, University of Calgary, April.

Goad, C. and L. Goodman. (1974). A Modified Hopfield Tropospheric Refraction Correction Model. Presented at the Fall Annual Meeting American Geophysical Union, San Francisco, California, December.

Hatch, R. (1986). Dynamic Differential GPS at the Centimeter Level. Proceedings of the Fourth International Geodetic Symposium on Satellite Positioning, Austin, TX.

Himmelblau, D. (1974). Basic Principles and Calculations in Chemical Engineering. Prentice-Hall, Inc., p. 591.

Hopfield, H. (1969). Two-quartic Tropospheric Refractivity Profile for Correction Satellite Data. Journal of Geophysical Research, Volume 74, Number 18, pp. 4487-4499.

Howind, J., Kutterer, H., and Heck, B. (1999): Impact of temporal correlations on GPS-derived relative point positions. Journal of Geodesy, Volume 73, pp. 246-258.

Hugentobler, U., S. Schaer, and P. Fridez. (2001). Bernese GPS Software, Version 4.2. Astronomical Institute, University of Bern, 2001.

International GPS Service (IGS). (2001). International GPS Service Annual Report 2000, IGS Central Bureau, Jet Propulsion Laboratory. Pasadena, California, p. 14-16.

Jefferson, D. and Y. Bar-Sever. (2000). Accuracy and Consistency of Broadcast GPS Ephemeris Data. Proceedings of ION GPS-2000, Salt Lake City, Utah, September 19-22, pp. 438-446.

Kaplan, E. (1996). Understanding GPS Principles and Applications. Artech House Publishers, p. 231-261.

Klobuchar, J., P. Doherty, and B. El-Arini. (1995). Potential Ionospheric Limitations to GPS Wide-Area Augmentation System, Navigation: Journal of the Institute of Navigation, Volume 42, Number 1, Spring, pp. 353.

Klobuchar, J. (1996). Global Positioning System: Theory and Applications, Chapter 12: Ionospheric Effects on GPS. Volume 163, Progress in Astronautics and Aeronautics, p. 485-515.

Knight, M. and A. Finn. (1998). The Effects of Ionospheric Scintillations on GPS. Proceedings of ION GPS-98, Nashville, Tennessee, September 15-18, pp. 673-685.

Kouba, J. and P. Héroux. (2001). GPS Precise Point Positioning Using IGS Orbit Products. GPS Solutions Quarterly Technical Journal, Volume 5, Number 2, Fall, pp. 12-28.

Kunches, J. (1997). Now it Gets Interesting: GPS and the Onset of Solar Cycle 23. Proceedings of ION GPS-97, Kansas City, Missouri, September 16-19, pp. 225-230.

Lachapelle, G., J. Hagglund, W. Falkenberg, P. Bellemare, M. Casey, and M. Eaton. (1986). GPS Land Kinematic Experiments. Proceedings of the Fourth International Geodetic Symposium on Satellite Positioning, Austin, TX, pp.1327-1344.

Lachapelle, G., W. Falkenberg, D. Neufeldt, and P. Keilland. (1989). Marine DGPS Using Code and Carrier in a Multipath Environment. Proceedings of ION GPS-89, Colorado Springs, Colorado, September 27-29, pp. 343-347.

Lachapelle, G., H. Sun, M. E. Cannon, and G. Lu. (1994). Precise Aircraft-to-Aircraft Positioning Using a Multiple Receiver Configuration. Canadian Aeronautics and Space Journal, Volume 40, Number 2, pp. 74-78.

Lachapelle, G., A. Bruton, J. Henriksen, M. E. Cannon, and C. McMillan. (1996a). Evaluation of High Performance Multipath Reduction Technologies for Precise DGPS Shipborne Positioning. The Hydrographic Journal, Number 82, October, pp. 11-17.

Lachapelle, G., M. E. Cannon, W. Qiu, and C. Varner. (1996b). Precise Aircraft Single-Point Positioning Using GPS Post-Mission Orbits and Satellite Clock Corrections. Journal of Geodesy.

Lachapelle, G., S. Ryan, M. Petovello, and J. Stephen. (1997). Augmentation of GPS/GLONASS for Vehicular Navigation Under Signal Masking. Proceedings of ION GPS-97, Kansas City, Missouri, September 16-19, pp. 1511-1519.

Langley, R. (1996). GPS for Geodesy, Chapter 5: GPS Receivers and Observables. 2$^{nd}$ Edition, Springer-Verlag, pp. 151-185.

Langley, R., H. Jannasch, B. Peeters, and S. Bisnath. (2000). The GPS Broadcast Orbits: An Accuracy Analysis. Viewgraphs of paper presented in Session B2.1-PSD1, 33rd COSPAR Scientific Assembly, Warsaw, Poland, July 16-23.

Mayaud, P. (1980). Derivation, Meaning and Use of Geomagnetic Indices. Geophysical Monograph 22, American Geophysical Union, Washington, DC.

National Academy of Public Administration/National Research Council (NAPA/NRC). (1995). The Global Positioning System – Charting the Future, Washington, DC.

National Oceanic and Atmospheric Administration Space Environment Center (NOAA). (2001). Official Space Weather Advisory, November 4.

Nayak, R. (2000). Reliable and Continuous Urban Navigation Using Multiple GPS Antennas and a Low Cost IMU. MSc thesis, Department of Geomatics Engineering, University of Calgary, October, p. 20.

Neilan, R., A. Moore, T. Springer, J. Kouba, J. Ray, and C. Reigber. (2000). International GPS Service 2000: Life Without SA. Proceedings of ION GPS-2000, Salt Lake City, Utah, September 19-22, pp. 438-446.

NovAtel. (2000). Look Into NovAtel's GPS-600 Antenna. Product Specification Sheet.

O'Keefe, K. (2001). Availability and Reliability Advantages of GPS/Galileo Integration. Proceedings of ION GPS-2001, Salt Lake City, Utah, September 11-14, pp. 2096-2104.

Parkinson, B., T. Stansell, R. Beard, K. Gromov. (1995). A History of Satellite Navigation. Navigation: Journal of the Institute of Navigation, Volume 42, Number 1, Spring, pp. 109-164.

Peck, S., C. Griffith, V. Reinhart, J. Tekawy, W. Bertiger, B. Haines, and G. Winkler. (1997). WAAS Network Time Performance and Validation Results. Proceedings of ION GPS-97, Kansas City, Missouri, September 16-19, pp. 1123-1131.

Petovello, M., M. E. Cannon, and G. Lachapelle. (2000) $C^3NAVG^2$ Operating Manual. Department of Geomatics Engineering, University of Calgary, May.

Press, W., S. Teukolsky, W. Vetterling, and B. Flannery. (1988). Numerical Recipes in C, Cambridge University Press.

Qiu, W. (1993). An Analysis of Some Critical Error Sources in Static GPS Surveying, UCGE Reports No. 20054, Department of Geomatics Engineering, University of Calgary.

Radovanovic, R. (2001). Variance-Covariance Modeling of Carrier Phase Errors for Rigorous Adjustment of Local Area Networks. IAG 2001 Scientific Assembly, Budapest, Hungary, September 2-7, 2001, Section C3 Paper 6.

Raquet, J. (1998). Development of a Method for Kinematic GPS Carrier-Phase Ambiguity Resolution Using Multiple Reference Receivers. PhD thesis, Department of Geomatics Engineering, University of Calgary, May.

Ray, J. (2000). Mitigation of GPS Code and Carrier Phase Multipath Effects Using a Multi-Antenna System. PhD thesis, Department of Geomatics Engineering, University of Calgary, March.

Saastamoinen, I. (1973). Contribution to the Theory of Atmospheric Refraction, Bulletin Geodesique, 107, pp. 13-34.

Seeber, G. (1993). Satellite Geodesy Foundations, Methods, and Applications. Published by Walter de Gruyter, pp. 291-295.

Shi, J. and M.E. Cannon. (1995). Critical Error Effects and Analysis in Carrier Phase-Based Airborne GPS Positioning Over Larger Areas. Bulletin Geodesique, Number 69, pp. 261-273.

Skone, S. (1998). Wide Area Ionospheric Grid Modelling in the Auroral Region. PhD thesis, Department of Geomatics Engineering, University of Calgary, December.

Skone, S. (2001). The Impact of Magnetic Storms on GPS Receiver Performance. Journal of Geodesy, Volume 75, pp. 457-468.

Skone, S., M. El-Gizawy, and S. Shrestha. (2001). Limitations in GPS Positioning Accuracies and Receiver Tracking Performance During Solar Maximum. Proceedings of the International Symposium on Kinematic Systems in Geodesy, Geomatics, and Navigation. Banff, Alberta, June 5-8, pp. 129-143.

Spilker, J. (1996a). Global Positioning System: Theory and Applications, Chapter 4: GPS Navigation Data. Volume 163, Progress in Astronautics and Aeronautics, pp. 121-150.

Spilker, J. (1996b). Global Positioning System: Theory and Applications, Chapter 13: Tropospheric Effects on GPS. Volume 163, Progress in Astronautics and Aeronautics, pp. 517-546.

Townsend, B. and P. Fenton. (1994). A Practical Approach to the Reduction of Pseudorange Multipath Errors in a L1 GPS Receiver. Proceedings of ION-GPS 94, Salt Lake City, Utah, September, pp. 143-148.

Townsend, B., P. Fenton, K. Van Dierendonck, and R. van Nee. (1995). Performance Evaluation of the Multipath Eliminating Delay Lock Loop. Navigation, Journal of the Institute of Navigation, Volume 42, Number 3, Fall, pp. 503-514.

Trimble Navigation Limited. (1999). Software User Guide Volume 1 and 2, Trimble Geomatics Office, Version 1.00.

Van Dierendonck, A. J., P. Fenton, and T. Ford. (1992). Theory and Performance of a Narrow Correlator Spacing in a GPS Receiver. Navigation, Journal of the Institute of Navigation, Volume 39, Number 3, Fall, pp. 265-283.

Wells, D., N. Beck, D. Delikaraoglou, A. Kleusberg, E. Krakiwsky, G. Lachapelle, R. Langley, M. Nakiboglu, K. P. Schwarz, J. Tranquilla, P. Vanicek. (1987). Guide to GPS Positioning, 2nd printing with corrections, Canadian GPS Associates.

White House. (2000). Statement by the President Regarding the United State's Decision To Stop Degrading Global Positioning System Accuracy. White House Press Announcement, May 1.

Woo, K. (1999). Optimum Semi-Codeless Carrier Phase Tracking of L2. Proceedings of ION GPS-99, Nashville, Tennessee, September 14-17, pp. 289-305.

Zhodzishsky, M, P. Zagnetov, A. Zinoviev, J. Ashjaee. (1999). On Reducing the Impact of GDOP Discontinuties on Receiver Positioning Accuracy. Proceedings of ION GPS-99, Nashville, Tennessee, September 14-17, pp. 1629-1634.

Zumberge, J. and W. Bertiger. (1996). Global Positioning System: Theory and Applications, Chapter 16: Ephemeris and Clock Navigation Accuracy. Volume 163, Progress in Astronautics and Aeronautics, pp. 585-599.

# APPENDIX A

## SATELLITE ANTENNA OFFSETS

Table A.1: GPS satellite antenna phase offsets, with respect to the centre of mass in the SCSF system (Hugentobler et al., 2001).

| SV | Block | Across-track offset (m) | Along-track offset (m) | Radial offset (m) |
|----|-------|-------------------------|------------------------|-------------------|
| 1  | II A  | 0.2794 | 0 | 1.0230 |
| 2  | II    | 0      | 0 | 0      |
| 3  | II A  | 0.2794 | 0 | 1.0230 |
| 4  | II A  | 0.2794 | 0 | 1.0230 |
| 5  | II A  | 0.2794 | 0 | 1.0230 |
| 6  | II A  | 0.2794 | 0 | 1.0230 |
| 7  | II A  | 0.2794 | 0 | 1.0230 |
| 8  | II A  | 0.2794 | 0 | 1.0230 |
| 9  | II A  | 0.2794 | 0 | 1.0230 |
| 10 | II A  | 0.2794 | 0 | 1.0230 |
| 11 | II R  | 0      | 0 | 0      |
| 12 | I     | 0.2100 | 0 | 0.8540 |
| 13 | II R  | 0      | 0 | 0      |
| 14 | II R  | 0      | 0 | 0      |
| 15 | II    | 0.2794 | 0 | 1.0230 |
| 16 | II    | 0.2794 | 0 | 1.0230 |
| 17 | II    | 0.2794 | 0 | 1.0230 |
| 18 | II R  | 0      | 0 | 0      |
| 19 | II    | 0.2794 | 0 | 1.0230 |
| 20 | II R  | 0      | 0 | 0      |

| SV | Block | Across-track offset (m) | Along-track offset (m) | Radial offset (m) |
|----|-------|------------------------|------------------------|-------------------|
| 21 | II    | 0.2794 | 0 | 1.0230 |
| 22 | II A  | 0.2794 | 0 | 1.0230 |
| 23 | II A  | 0.2794 | 0 | 1.0230 |
| 24 | II A  | 0.2794 | 0 | 1.0230 |
| 25 | II A  | 0.2794 | 0 | 1.0230 |
| 26 | II A  | 0.2794 | 0 | 1.0230 |
| 27 | II A  | 0.2794 | 0 | 1.0230 |
| 28 | II R  | 0 | 0 | 0 |
| 29 | II A  | 0.2794 | 0 | 1.0230 |
| 30 | II A  | 0.2794 | 0 | 1.0230 |
| 31 | II A  | 0.2794 | 0 | 1.0230 |

Notes:

1. Satellite block and antenna offsets are as of November 14, 2001. They are valid for the land data collected on November 2-10, 2001.
2. Satellites 12, 16, and 19 were not available when the land data was collected.
3. Satellite 12 was decommissioned in 1995.
4. Satellite 16 was decommissioned in 2000.
5. Satellite 19 has reported bad health since 2001.